Models of stellar winds from X-ray bursts

Author:

Yago Herrera

Thesis submitted for the degree of
Doctor in Philosophy.

Advisor:
Dr. Glòria Sala

Co-advisor:
Dr. Jordi José

Barcelona, October 2021.

Acknowledgements

"On a stormy sea of moving emotion,
tossed about, I'm like a ship on the ocean.
I set a course for winds of fortune,
but I hear the voices say...

Carry on, my wayward son.
There'll be peace when you are done.
Lay your weary head to rest.
Don't you cry no more..."

"Carry on, wayward son", song by Kansas.

This doctoral thesis research was funded by a grant from the *Fondo de Proyectos de Investigación* (FPI), awarded by *Ministerio de Economía y Competitividad* (MINECO) of the Spanish government. It was also made possible by such an excellent house of knowledge as Universitat Politècnica de Catalunya.

I want to thank my advisors, Dr. Glòria Sala and Dr. Jordi José. Glòria's supportive and enthusiastic guidance never hindered my curiosity to explore, but she was also there to steer my efforts back on track whenever I wandered too far off. Jordi's thorough attention to details was as helpful as his vast experience and focus on the important issues. My immense gratitude to both of them for giving me the chance to dive into such an interesting topic, full of challenge and learning opportunities, for their patience and effort, and, above all, for being both great human beings.

My dear friend, Dr. Guadalupe Ruiz, is one of the main characters in this adventure too. Without her recommendation and huge help in starting this quest, none of it would have happened. For this, and for being always present as one of my best friends for more than a decade, I owe her my eternal gratitude. This journey was more enjoyable by the company of my fellow PhD and master students, who became my dearest friends: Sofia, Araceli, Jonny, Eda, Arman and Joana; but also by the fun and interesting times with my friends outside academy: Gabor, Ayla, Liam, Fanni, Pavel, and Lucas, who became my surrogate family.

Family is where everything begins, my parents and my brothers made me who I am. They gave me the passion and thirst for knowledge, the wit and wisdom to try to be a better person, and the heart and will to face adversity. Words cannot begin to describe how much I owe to them, and how much I love them. Finally, to Mila, for all her love and support, and for being the greatest life partner, friend, and companion I ever had the illusion of finding. All the things we share, and all the nice and memorable moments, are engraved in my heart and made me a new person. To them I especially dedicate this work, full-heartedly.

Contents

List of Tables

List of Figures

Chapter 1

Introduction

1.1 X-ray bursts

X-ray bursts (XRBs) were discovered in the mid 1970s independently by Babushkina *et al.* (1975); Belian *et al.* (1976); Grindlay *et al.* (1976). Most of them are characterized by bright and sudden spikes in the X-ray band of the electromagnetic spectrum, starting with a quick and sharp luminosity rise, in about 1 – 10 `s`, followed by a much slower decay tail ranging from $\sim$ 10 to 100 `s`, and recurrence periods from hours to days. The luminosity can sometimes rise up to a thousandfold the *persistent* (normal) luminosity of the source, although the typical increase is in the hundreds, reaching values of the order of 10^{38} `erg/s`, with a total energy output of about 10^{39} `erg`. An odd exception was soon found with the discovery of the *Rapid Burster* MXB 1738-335 (see Lewin *et al.* 1976), which exhibited much quicker sequences of short lived bursts with no tail, recurring every $\sim$ 10 `s`, as well as some of the other *normal* bursts. XRBs were then classified into type I,[1] for the most commonly observed ones, and type II for quicker ones in the *Rapid Burster*.[2]

The spatial distribution of most of the XRB sources observed matches that of low-mass X-ray binaries (LMXB)[3] around the galactic center. Globular clusters contain a significant portion of these bursting sources, suggesting a connection with old population stars (see Lewin *et al.* 1993). More recently, extragalactic XRB sources have been discovered in globular clusters around the Andromeda galaxy (see Pietsch & Haberl 2005). As of today, more than a hundred type I XRB sources have been identified,[4] constituting the most frequent type of explosive event in the galaxy, and ranking third in terms of total energy output after supernova and classical novae.

Several mechanisms have been proposed to explain the origin of XRBs. Following pioneering work by Hansen & van Horn (1975), two independent works suggested that either

[1] See Page 2 for a modern classification of type I XRBs based on their duration and recurrence times.

[2] Only one other source was found to date exhibiting type II XRBs: the bursting pulsar GRO J1744-28 (see Finger *et al.* 1996; Kouveliotou *et al.* 1996).

[3] LMXBs are bright X-ray emitting binary systems composed of a massive compact object (neutron star or black hole), and a less massive main sequence star, red giant, or sometimes a white dwarf. The X-rays originate in the hot plasma at the inner parts of the accretion disk that forms around the compact object, made of material stolen from the companion star (see further ahead).

[4] See `http://www.sron.nl/~jeanz/bursterlist.html` for an updated list of known galactic type I XRB systems.

the hydrogen-rich material (Woosley & Taam 1976) or helium-rich material (Maraschi & Cavaliere 1977), accreted onto a compact object like a neutron star and undergoing thermal instabilities under high electron degeneracy, could erupt in thermonuclear flashes powering the burst episodes. A first evidence supporting the thermonuclear origin of XRBs is the ratio between time-integrated persistent and burst energy fluxes, α, observed to lie typically in the range ~ 40 – 100. This is in close correspondence with the ratio between the gravitational potential energy released by matter falling onto the neutron star (NS) during the accretion stage ($GM_{\rm NS}/R_{\rm NS} \sim 200$ `MeV` per nucleon) and the nuclear energy generated in the burst (about 5 `MeV` per nucleon, for a solar mixture burned all the way up to the Fe-group nuclei). However, the features of type II XRBs were better associated with accretion instabilities (see Hoffman *et al.* 1978), as follows. A magnetized NS could temporarily hold off the material spiraling in from the accretion disk, which then accumulates on the magnetosphere. Eventually, a fraction of this material pushes through, generating a spike of X-rays from the conversion of its gravitational energy, with no tail, as expected for type II XRBs. In turn, this mechanism also suggests that sources exclusively exhibiting type I XRBs lack a strong enough magnetic field ($< 10^{11}$ `G`) to generate these accretion instabilities.[5]

Early semi-analytical models portraying a NS as the host for type I XRBs were developed by Joss (1977), and Lamb & Lamb (1978). Later, Joss (1978) performed the first numerical simulations, showing that unstable helium burning can explain their main observational features like light curves, total energy, recurrence times and spectral features. Several studies followed during the 1980s, improving in different aspects and studying the influence of several parameters such as NS masses and radii, central temperatures, magnetic fields, accretion rates and metallicity of the accreted material (see, e.g., Joss & Li 1980; Ayasli & Joss 1982; Paczyński 1983). One key limiting aspect in the progression of numerical models was the available computational power, which restricted their complexity in terms of input physics and level of detail attained. For instance, during the 1980s, models were restricted to reduced nuclear reaction networks, or to a single burst.

Modern numerical models couple 1-dimensional hydrodynamic simulations to larger nuclear reaction networks, containing hundreds of isotopes linked by thousands of possible reactions (see Woosley *et al.* 2004; Tan *et al.* 2007; Fisker *et al.* 2008; José *et al.* 2010). They are also capable of simulating several consecutive bursts, which provides information about the long-term evolution of these systems, a relevant issue since the properties of every subsequent burst may be affected by the initial conditions set by previous ones. Particularly, the thermal and compositional inertia determines the energy and fuel availability for following bursts, which in turn affects features like their nuclear burning regimes (stable/unstable H/He burning, C burning), ignition depth, or cooling timescales. In close relation to this, observations have also revealed some bursts characterized by longer duration and recurrence time, and larger energy output. These have opened a subtype classification of type I XRBs into *Normal bursts* (for the most common ones described before), *Intermediate bursts* (with durations in $15 - 40$ `min`, recurrences times of tens of days, and energy outputs in 10^{40-41} `erg`), and *Superbursts* (lasting ~ 1 `day`, recurring every $1 - 2$ `yr`, and as energetic as 10^{42} `erg`). Their mechanisms are similar in essence, and their difference is thought to derive mainly from higher ignition depths, which delays cooling timescales, and different nuclear burning regimes: He-accretion in ultra compact X-ray binaries or ashes accumulated from previous hydrogen bursts for *Intermediate* bursts, and carbon burning for *Superbursts* (see,

[5] See, however, Bult *et al.* (2019) for a recent detection of type I XRBs in a pulsar, and Goodwin *et al.* (2021) for a model of type I XRB including the effect of accretion hot-spots caused by NS magnetic fields.

e.g., Keek & in't Zand 2008, and references therein).

Today, the general picture for the scenario and basic mechanism behind the most common XRBs is well accepted in the scientific community. Type I XRBs are highly energetic and recurrent thermonuclear events occurring on the envelope of accreting neutron stars in binary systems where the secondary star is usually a main sequence star or red giant. Most observed XRBs have short orbital periods, in the range 0.2–15 hr.[6] As a result, the secondary star overfills its Roche lobe and mass-transfer ensues through the inner Lagrangian point (L1) of the system. The material stripped from the secondary has angular momentum, such that it forms an accretion disk around the NS. Viscous forces then progressively remove angular momentum from the disk forcing the material to spiral in and pile up on top of the NS. The accreted material accumulates under mildly degenerate conditions, driving a temperature increase and the onset of nuclear reactions. As a result, a thermonuclear runaway occurs, generating a massive luminosity increase as well as nucleosynthesis of heavier elements, mostly around $A = 64$ (see, e.g., José *et al.* 2010; Fisker *et al.* 2008; Woosley *et al.* 2004). The presence of heavy elements can, in principle, be detected (see Weinberg *et al.* 2006; Chang *et al.* 2005, 2006; Bildsten *et al.* 2003) in the form of absorption features in the spectrum, which mostly lies in the X-ray range. For further information on XRBs see Strohmayer & Bildsten (2006); Keek & in't Zand (2008); Galloway *et al.* (2008); José (2016).

The mechanism powering XRBs bears a clear resemblance with that for classical novae (hosted by white dwarfs instead), but unlike them, the high surface gravity of the NS prevents, in principle, the explosive ejection of material. A typical NS ($M_{\rm NS} \sim 1.4$ $\rm M_\odot$, $R_{\rm NS} \sim 10$ km) has an escape velocity of $v_{\rm esc} \sim 2c/3$, allowing only a limited envelope expansion before the nuclear fuel is consumed. However, for some values of accretion rate, a considerable photospheric radius expansion (PRE) takes place. In these cases, the luminosity can approach or even exceed the Eddington limit in some of the outer layers of the expanded envelope, which may lead to the ejection of some material through a radiation-driven wind.

1.2 Stellar winds

Stellar winds have been studied in different scenarios throughout most part of 20th century, and in a variety of forms (see Parker 1965; Żytkow 1972; Castor *et al.* 1975). The simplest models assume spherical symmetry and stationary wind and can be broadly classified according to the main driving mechanism into gas pressure-driven or radiation-driven, although magnetic fields can also play an important role. For a wind to be radiatively driven, high luminosity and high opacity must be present.

In the framework of neutron stars, several studies of radiation-driven winds have been performed since the early 1980s, with varying hypotheses, approximations and calculation techniques. Ebisuzaki *et al.* (1983), Kato (1983), Quinn & Paczyński (1985) and Joss & Melia (1987) all used non-relativistic models with an approximated formula for opacity as a function of temperature. The models adopted different boundary conditions both at the photosphere and at the base of the wind envelope, as well as different treatments of the sonic point singularity (see Chapter 2). Studies based on general relativistic models were performed by Turolla *et al.* (1986), and Paczyński & Prószyński (1986). In a more recent work Yu & Weinberg (2018) used MESA code (see Paxton *et al.* 2011) to perform a time-dependent hydrodynamic simulation of the wind envelope following a hydrostatic burst rise.

[6] Exceptions include GX 13+1 (592.8 hr), Cir X-1 (398.4 hr), and Cyg X-2 (236.2 hr).

As this thesis was being written, Guichandut *et al.* (2021) published a study including an analysis of the transition from static expanded envelopes to radiatively-driven stellar wind and discuss the applicability of steady-state models during it.

1.3 Motivation and objectives

Advances in computational power and numerical techniques have allowed several studies since the 2000s to perform hydrodynamic simulations of XRBs with extended nuclear reaction networks (see Fisker *et al.* 2008; Woosley *et al.* 2004; José *et al.* 2010). These studies have shown that XRBs synthesize a large variety of proton-rich nuclei. The potential impact of XRBs on galactic abundances is still a matter of debate and relies on the high overproduction of some particular isotopes, but also on the ejection of material during the burst. It has been suggested that if a tiny fraction of the accreted envelope is ejected through radiation-driven winds, XRBs may potentially be the source of some light p-nuclei, such as ^{92,94}Mo and ^{96,98}Ru (see Schatz *et al.* 1998, 2001), which are systematically under-produced in all canonical scenarios proposed to date for the synthesis of such species. However, it is still not clear whether XRBs contribute to the galactic abundances, since the strong gravitational pull of the NS prevents the direct ejection of matter, only potentially viable through a radiation-driven wind.

Additionally, the study of XRBs wind can lead to a more accurate determination of neutron stars radii, and help constrain the equation of state (EoS) of neutron star matter (see Özel *et al.* 2010; Steiner *et al.* 2010). Several theoretical models for the state of matter inside neutron stars have been proposed, resulting in a variety of possible EoS (see Lattimer & Prakash 2006). When modeling a NS interior structure, a given choice of EoS determines a specific mass-radius relation. Thus, accurate measurements of NS masses and radii, taken independently, are needed to test the validity of these theoretical models. Neutron star masses, for instance, can be determined from bolometric luminosities during XRBs with significant envelope expansion (assuming the maximum corresponds to the Eddington limit). The radius is more difficult to measure, and methods proposed carry a varied sensitivity to systematic errors (see Damen *et al.* 1990; Steiner *et al.* 2010; Güver *et al.* 2012; Sala *et al.* 2012). A detailed study of the NS envelope evolution during XRBs, that includes stellar wind features, can bring more light into this matter.

Motivated by the aforementioned unanswered questions and by the new possibilities brought by the recent technical advancements, the interest of the scientific community in stellar winds in the context of XRBs has been renewed. For this reason, we proceeded to reanalyze these wind mechanisms, trying to improve on some aspects of input physics (like updated opacity), numerical techniques (critical point treatment), and deepening the analysis of solutions, the exploration of parameter space and characterization of observable magnitudes in the context of neutron stars. Once this is achieved, the final objective is to apply the stellar wind model, with the aforementioned improvements (and implemented through a simulation code entirely developed in this work), to the physical conditions of type I XRBs. We proceed towards this goal by matching numerical solutions of the stellar wind model, to a set of XRB hydrodynamic models developed by other members in our research group. This way, we could obtain physical predictions about the evolution of the entire neutron star atmosphere, including both the nuclear burning shells and the expanded wind envelope. On one hand, this allows us to study the evolution of observable magnitudes in more realistic conditions, and their relation to parameters such as NS mass and radius,

potentially leading to the development of better measuring techniques. And on the other hand, we can obtain the composition of the envelope layers blown by the wind, given by the isotopes synthesized in the nuclear reactions simulated in the XRB models. This allows us to study the possible contribution of XRBs to galactic abundances, with special interest in the aforementioned light proton-rich species.

This thesis is organized as follows. The basic stellar wind model, input physics and simulations setup are described in Chapter 2, with some mathematical aspects and details of the computation methods explained in Appendix A, and further details on input physics in Appendix B. Results from our simulations of radiative winds applied to a generic NS scenario, are presented in Section 2.4. There, the focus is set on the exploration of parameter space, the characterization of different types of solution and their self-consistency with model hypotheses, and analysis of possible predictions related to observable variables, paving the road to the application of the wind models to a more complex XRB scenario. This work has been published in *Astronomy & Astrophysics* (Herrera *et al.* 2020). Chapter 3 is dedicated to the application of our stellar wind simulations to the XRB scenario described by the hydrodynamic simulations performed by José *et al.* (2010), which includes a thermonuclear reaction network with over 300 isotopes and more than a thousand possible reactions. There, a summarized description of their XRB hydrodynamic models is followed by an account of the methods employed to match both the stellar wind and XRB hydrodynamic simulations, and an analysis of the results obtained, including the wind-related mass-loss and its contribution of key isotope species to galactic abundances, as well as the impact on observable features. Several bursts were analyzed; results from the best matching model are presented in Chapter 3, and additional models are described in Appendix C. Finally, the significance of our results and our main conclusions are summarized in Chapter 4.

Chapter 2

Stellar wind model

Stellar winds are a common feature found in luminous stars. They affect the physics of stellar atmospheres, regarding density stratification and energy transfer, through the appearance of transonic velocity fields in macroscopic scale. They also influence the evolution of their host stars through mass-loss and the consequent modification of their surface abundances and chemical profiles. This in turn affects the galactic dynamic, depositing energy and momentum, but also heavy elements byproduct of nuleosynthesis, into the interstellar medium.

The first theoretical model of stellar winds was published by Parker (1965). It was used to describe the solar wind, with a constant temperature profile, driven purely by a gas pressure gradient. This simple model has analytical solutions. Since then, numerous developments followed, rising in complexity and including different driving mechanisms resulting from microscopic interactions between photons and atoms, molecules or dust present in the atmosphere.

Without any prior assumption on the temperature profile throughout the envelope, the spherically symmetric stationary wind equations constitute a set of nonlinear coupled differential equations. The boundary conditions are often given at more than one point and with implicit expressions. Another common feature is the appearance of a singular point where the wind becomes supersonic (see Section 2.2.2). Different approaches have been implemented to deal with the numerical difficulties involved in solving the equations close to this singular point (see, e.g., Żytkow 1972; Joss & Melia 1987; Paczyński & Prószyński 1986).

In this chapter we present a new implementation of a radiatively-driven stellar wind model, commonly employed in compact star scenarios. We describe its main features and equations in Section 2.1. The choice of boundary conditions from different prescriptions available in literature is discussed in Section 2.2. An outline of the calculation method is explained in Section 2.3, with additional details in Appendix A. This model was successfully implemented in a generic NS scenario and the results are shown in Section 2.4, with further analysis and discussion in Section 2.5.

2.1 Radiative stellar wind equations

The simulations reported in this work rely on a stationary, nonrelativistic wind model with spherical symmetry. Neutron stars have a typical radius of a few times their Schwarz-

schild radius, and so while general relativity corrections on gravity could be of importance close to its surface, they diminish rapidly in a wind envelope that extends hundreds of kilometers. Paczyński & Prószyński (1986) showed that the main effects of general relativity on the wind structure can be relevant for solutions with lower mass outflows ($< 5\times10^{17}$ g/s), resulting in a more extended (up to a factor of 4) and cooler envelope. However, they rapidly become less significant for higher mass outflows, giving corrections of only a few percent. We therefore leave the effects of general relativity for a follow-up work and study the Newtonian approach here as a stepping stone. The radiation-driven wind, treated as a fully ionized perfect gas, is assumed to be optically thick and in local thermal equilibrium (LTE) with radiation. For a more detailed treatment of the optically thin regions and their impact on observables, see for example Joss & Melia (1987) (non-relativistic model) or, more recently Guichandut *et al.* (2021) (relativistic model).

In this framework, the basic hydrodynamic equations for mass (2.1), energy (2.2), momentum conservation (2.3), and radiative energy transport (2.4) become:[1]

$$\dot{M} = 4\pi r^2 \rho v \tag{2.1}$$

$$\dot{E} = \dot{M}\left(\frac{v^2}{2} - \frac{GM}{r} + h\right) + L_R \tag{2.2}$$

$$0 = v\frac{\mathrm{d}v}{\mathrm{d}r} + \frac{GM}{r^2} + \frac{1}{\rho}\frac{\mathrm{d}P}{\mathrm{d}r} \tag{2.3}$$

$$\frac{\mathrm{d}T}{\mathrm{d}r} = -\frac{3\,\kappa\rho L_R}{16\pi c a r^2 T^3}, \tag{2.4}$$

where the variables $r, T, v, \rho, L_{\mathtt{R}}$ stand for the radial coordinate, temperature, wind velocity, gas density, and radiative luminosity, respectively. The total pressure P, and specific enthalpy h, include the contributions of gas and radiation, in the form:

$$P(\rho,T) = \frac{\rho k T}{\mu m_A} + \frac{aT^4}{3} \qquad \text{and} \qquad h(\rho,T) = \frac{5}{2}\frac{kT}{\mu m_A} + \frac{4}{3}\frac{aT^4}{\rho}. \tag{2.5}$$

The opacity $\kappa(T,\rho)$ must be provided externally either from a radiation transport theoretical model, phenomenological relations, or experimental values. Opacity can have different sources depending on the microscopic processes involved; in general, these depend on photon frequency. The tables calculated by *OPAL* (Iglesias & Rogers 1996) take these aspects into account to give a Rosseland mean opacity as a function of temperature, density, and composition of the gas only. These tables have become the standard source for stellar opacity in recent decades and were used in the present work to obtain the first preliminary results for Section 2.4. Later, they had to be replaced by similar tables from *The Opacity Project* (Seaton *et al.* 1994), that allow changes in gas composition more conveniently, which was necessary for Chapter 3. More details about the opacity tables, and how they are employed, can be found in Appendix Section B.2.

The total mass and energy outflows $(\dot{M}, \dot{E})$ arise as integration constants from the mass and energy conservation laws and can be determined by imposing extra conditions at the base of the wind. Therefore, $\dot{M}$ and $\dot{E}$ can be considered free model parameters. During an XRB these will vary in time but, in a quasi-stationary approach, are assumed to be

[1] See, for instance, Shore (1992) for a derivation from fundamental fluid equations, and other simpler models with analytical solutions.

approximately constant across the wind for a fixed time. The mass of the neutron star core, M, is another model parameter, considered fixed in this work, and constitutes the only relevant source of gravity (the contribution of the envelope mass can be neglected). Lastly the mean molecular mass μ is a function of the mass fractions X_i of the different species present in the envelope (see Appendix Section B.1). The rest of the symbols have their usual meaning: G for gravitational constant, c for speed of light, k for Boltzmann constant, $a = \frac{4\sigma}{c}$ for radiation energy density constant (σ is the Stefan-Boltzmann constant) and m_A for atomic mass unit.

By differentiating the mass conservation equation 2.1, for a constant $\dot{M}$, one can obtain:

$$0 = 2\frac{\mathrm{d}r}{r} + \frac{\mathrm{d}\rho}{\rho} + \frac{\mathrm{d}v}{v}. \tag{2.6}$$

One can also calculate, from equation 2.5, the pressure differential appearing as the last term in the momentum equation 2.3:

$$\frac{\mathrm{d}P}{\rho} = \frac{kT}{\mu m_A}\left(\frac{\mathrm{d}T}{T} + \frac{\mathrm{d}\rho}{\rho}\right) + \frac{4}{3}\frac{aT^4}{\rho}\frac{\mathrm{d}T}{T}, \tag{2.7}$$

and by using equation 2.6 to replace the density differential:

$$\frac{\mathrm{d}P}{\rho} = -\frac{kT}{\mu m_A}\left(\frac{2\mathrm{d}r}{r} + \frac{\mathrm{d}v}{v}\right) + \left(\frac{kT}{\mu m_A} + \frac{4}{3}\frac{aT^4}{\rho}\right)\frac{\mathrm{d}T}{T}. \tag{2.8}$$

After some regrouping, both differential equations 2.3 and 2.4 can be put in the form:

$$\left(v^2 - \frac{kT}{\mu m_A}\right)\frac{\mathrm{d}v}{v} + \left(\frac{kT}{\mu m_A} + \frac{4}{3}\frac{aT^4}{\rho}\right)\frac{\mathrm{d}T}{T} + \left(\frac{GM}{r} - 2\frac{kT}{\mu m_A}\right)\frac{\mathrm{d}r}{r} = 0 \tag{2.9}$$

$$\left(\frac{4}{3}\frac{aT^4}{\rho}\right)\frac{\mathrm{d}T}{T} + \left(\frac{GM}{r}\Gamma\right)\frac{\mathrm{d}r}{r} = 0, \tag{2.10}$$

where we introduced the luminosity ratio $\Gamma = L_{\mathtt{R}}/L_{\mathtt{Edd}} = \frac{\kappa L_R}{4\pi cGM}$ ($L_{\mathtt{Edd}}$ is the local Eddington luminosity). The density and radiative luminosity can be obtained using the mass and energy conservation equations 2.1 and 2.2:

$$\rho = \frac{\dot{M}}{4\pi r^2 v} \tag{2.11}$$

$$L_R = \dot{E} - \dot{M}\left(\frac{v^2}{2} - \frac{GM}{r} + \frac{5}{2}\frac{kT}{\mu m_A} + \frac{4}{3}\frac{aT^4}{\rho}\right). \tag{2.12}$$

These constitute a system of four equations, two algebraic (2.11 and 2.12) and two first-order ordinary differential equations (2.9 and 2.10) that can be solved for v, T, ρ, L_R as functions of the independent variable r.

2.2 Boundary conditions

Two boundary conditions are required to solve the system of two first-order differential equations 2.9 and 2.10. These are normally given at the photosphere (usual for any stellar envelope, but with a slight difference for winds), and a critical point (for stellar wind solutions with non zero velocity at large radii). Additionally, an extra set of conditions can be set to fix the value of the free model parameters $\dot{M}$ and $\dot{E}$ which, in reality, are the integration constants of the original differential equations of mass and energy conservation.

2.2.1 Photosphere

The first condition is given by the definition of the photosphere, where the gas temperature is equal to the effective temperature $T_{\texttt{eff}}$, and can be written as:

$$T_{\rm ph} = T_{\rm eff} = \left(\frac{L_{\rm R,ph}}{\pi a c r_{\rm ph}^2} \right)^{\frac{1}{4}}, \tag{2.13}$$

which shall be referred to as "temperature condition". Hereafter, sub-index "ph" denotes evaluation at the photosphere.

The location of the photosphere in radius is not known a priori so this adds an extra unknown parameter. This is usually given by the point at which the optical depth is about unity,[2] which would require the integration of the atmosphere above the photospheric surface. In the case of an extended atmosphere it is usual to take a locally defined effective optical depth $\tau^* = \kappa\rho r$ that takes a minimum at the photosphere with an approximate value of $\tau^*_{\rm ph} \simeq 3$ (see Kovetz 1998). Kato & Hachisu (1994) showed, in a semi-analytical approximation, that this minimum usually corresponds to the point where this effective optical depth takes a value closer to $\tau^*_{\rm ph} \gtrsim 8/3$. Accordingly, we adopt the following "optical condition":

$$\tau^*_{\rm ph} = \frac{8}{3} \simeq 2.67, \tag{2.14}$$

which constitutes a reasonable approximation that allows us to avoid the integration of the optically-thin upper atmosphere.[3] These conditions, 2.13 and 2.14, when replaced in the radiation diffusion equation 2.4 give rise to a condition for the temperature gradient at the photosphere:

$$\left.\frac{\mathrm{d}\log T}{\mathrm{d}\log r}\right|_{\rm ph} = -\left.\frac{3\kappa\rho r}{16}\frac{L_R}{\pi a c r^2 T^4}\right|_{\rm ph} \simeq -\frac{1}{2}, \tag{2.15}$$

which can be used alternatively instead of either the optical or temperature conditions.

2.2.2 Critical point

The second boundary condition arises from the analysis of the topology of solutions to the momentum equation. From equation 2.9, the wind velocity gradient can be expressed as:

$$\frac{r}{v}\frac{\mathrm{d}v}{\mathrm{d}r} = -\frac{\left(\frac{kT}{\mu m_A} + \frac{4}{3}\frac{aT^4}{\rho}\right)\frac{r}{T}\frac{\mathrm{d}T}{\mathrm{d}r} + \left(\frac{GM}{r} - 2\frac{kT}{\mu m_A}\right)}{\left(v^2 - \frac{kT}{\mu m_A}\right)}, \tag{2.16}$$

[2] This is true in the plane-parallel atmosphere approximation, which is only reasonable for a thin envelope (small extension compared to star radius), but is no longer valid in extended atmospheres, like the ones expected here.

[3] A variety of choices for this τ^* value and other approaches have been adopted for this condition by different authors. The advantages of each choice, or the significance of their impact on results, do not appear to be a settled matter, or a very relevant one (see Guichandut *et al.* 2021).

from where it is clear that the momentum equation presents a singularity when:

$$v^2 = \frac{kT}{\mu m_A}, \tag{2.17}$$

that is, when the wind velocity is equal to the local isothermal sound speed (hereafter, singularity condition). If the conditions were such that this singular value was encountered, in order to have a nonsingular physical value for the velocity gradient we must simultaneously require the following "regularity condition":

$$\left(\frac{kT}{\mu m_A} + \frac{4}{3}\frac{aT^4}{\rho}\right)\frac{r}{T}\frac{\mathrm{d}T}{\mathrm{d}r} + \left(\frac{GM}{r} - 2\frac{kT}{\mu m_A}\right) = 0, \tag{2.18}$$

so that the quotient is finite. A solution may or may not pass through this "critical point" a priori, but the only physically acceptable solution with a wind velocity that approaches zero towards the bottom of the envelope and always increases outwards is the one that indeed does pass through this point. Furthermore, the wind becomes supersonic above this critical point (also known as the sonic point). It is not known a priori where this critical point will lie, but together Equations 2.17 and 2.18 provide both the extra condition needed to locate it and the second boundary condition for the integration constant. We will use the subscript "cr" to refer to variables evaluated at the critical sonic point.

We therefore have four unknown parameters $v_{\rm cr}, r_{\rm cr}, T_{\rm ph}, r_{\rm ph}$ with four conditions to solve them: two at the photosphere (temperature and optical conditions) and two at the critical point (singularity and regularity conditions). The system constitutes a two-point boundary-value problem with nonlinear first-order differential equations. Standard numerical methods for dealing with them are the relaxation method and the shooting method (see Appendix Section A.3).

2.2.3 Wind base

If the model parameters $\dot{M}$ and $\dot{E}$ are free, the resulting solutions may not always reach physical values compatible with those of a neutron star at the wind base. For instance, a high temperature may be found at radii much larger than those of typical neutron stars; on the other hand, velocity may not be realistically low enough (or temperature/density high enough) when reaching a typical neutron star radius. Previous works relied on simplified assumptions for the wind base conditions, such as for example a fixed value of density or temperature, or an energy generation rate given by integration of simple nuclear models. We find that these choices for a wind base may not always be compatible with some of the recent and more realistic hydrodynamic simulations for X-ray bursts (see José *et al.* 2010).

In order to accurately determine the conditions at the wind base, hydrodynamic simulations of the nuclear burning layers are clearly required. Matching stellar wind solutions to the boundary conditions set by XRB hydrodynamic models is a key task in this thesis and the main topic of Chapter 3, where it will be discussed in detail. For now, and as a stepping stone, we search for a condition for the wind base that is still realistic enough for a neutron star undergoing an X-ray burst, while at the same time leave some margin for the natural variability of the physical conditions. This necessary previous step can provide some insight on the possible solutions we can expect and their features, by exploring possible model parameter configurations, and at the same time help fine-tune the required computational tools developed to obtain them, among other things. The choice of this boundary condition will

be explained here, and a full study of the preliminary solutions obtained with it will follow in Section 2.4.

Setting a typical range of values for all the physical variables seems like a good approach at first, but the choice of several restriction values seems arbitrary and turned out to not always be compatible with self-consistent solutions. For instance, a particular choice of maximum velocity and minimum temperature at the wind base sometimes ended up giving solutions that were not deemed stationary (according to the characteristic time criterion explained in Sect. 2.3). Instead, we chose a criterion that is physically based, gives similar wind structure for all solutions, and reduces the amount of variables to be restricted, thus reducing arbitrariness, while at the same time still being compatible with the expected conditions for X-ray bursts. We set the wind base at the innermost point where the radiation pressure gradient becomes larger than the gas pressure gradient, that is where:

$$\nabla P_{\mathtt{R}} \geq \nabla P_{\mathtt{g}} \qquad \texttt{or} \qquad \frac{dP_{\mathtt{g}}}{dP_{\mathtt{R}}} \leq 1. \tag{2.19}$$

Above this point, radiation pressure becomes more important than gas pressure as the driving mechanism. Furthermore, in all solutions explored, the velocity gradient term $v\frac{dv}{dr}$ in the momentum conservation equation 2.3 is still negligible where the equality in equation 2.19 is met, and so the physical conditions can be considered to approximately match those of a static envelope. It can also be shown that at this point $\Gamma \simeq \frac{1}{2}$.

For the preliminary study in Section 2.4, solutions that meet the wind base condition in Eq. 2.19 at radii compatible with possible neutron stars ($7 - 20$ `km`) are then selected and considered as possible candidates for further study. In sections 2.4.1 and 2.4.2 we discuss the validity of these solutions for describing XRBs.

2.3 Numerical procedure

Solving the system of differential equations for stellar wind with analytical methods is only possible in very few cases, with quite restrictive conditions (isothermal or adiabatic wind, for instance) that are unrealistic for NS scenarios. A numerical approach is necessary, and it was implemented through a variety of computational algorithms explained in detail in Appendix A, and outlined here.

For a fixed set of wind model parameters $(\dot{M}, \dot{E}, M, X_i)$, a solution must satisfy all boundary conditions at the critical point and the photosphere. The integration method used to solve the differential equations is the adaptive-step Runge-Kutta (RK45) (see Appendix Section A.1). In order to deal with the two-point boundary-value problem (photosphere and critical point) we use the shooting method (see Appendix Section A.3) as follows. Integration starts at a critical point with radius $r_{\rm cr}$ and velocity $v_{\rm cr}$ satisfying both singularity and regularity conditions for a temporarily assumed $T_{\rm cr}$. Integration proceeds outwards until the optical photospheric condition is met ($\kappa\rho r \simeq 8/3$). There we parametrize a distance to the photospheric temperature condition with a value ϕ:

$$\phi = \frac{T - T_{\rm eff}}{T + T_{\rm eff}}, \tag{2.20}$$

and then use a suitable root-finding method for ϕ in terms of the chosen starting value for $T_{\rm cr}$ (see Appendix Section A.4). The numerical difficulties of starting the integration from the

critical point were solved through a change of variables that cancels the singular denominator in the velocity gradient (see Appendix Section A.2). The integration from the critical point to the photosphere corresponds to the region where the wind is supersonic. Once a supersonic profile is found, we go back to the critical point and proceed integrating inwards. The integration is stopped either when the temperature exceeds a given limit ($T > 10^{10}$ K) or the Schwarzschild radius is reached. Although these stopping point values are outside the region of validity of some of our model hypothesis (ideal gas and non-relativistic regime, respectively), they are only intended to give some margin of exploration for imposing extra boundary conditions at the wind base, as it will become necessary later in Chapter 3.

The solutions are checked for consistency and classified accordingly, in a similar fashion to that in Quinn & Paczyński (1985), as follows. In order for the wind to be considered thick, most of the acceleration must happen at high optical depth. It is enough to require that the sonic point lies at $\tau >> 1$. Solutions for which the effective optical depth of the critical point is too small ($\tau_c^* < 10$) are deemed as optically "thin". The stationary hypothesis is also checked by comparing the dynamical characteristic times Δt above and below the critical point, where

$$\Delta t = \int_{r_1}^{r_2} \frac{dr}{v}, \tag{2.21}$$

which is an estimate of the travel time of a fluid element between arbitrary radii r_1 and r_2.

For the solutions to be considered stationary, $\Delta t_{\texttt{above}} << \Delta t_{\texttt{below}}$, which by use of mass conservation translates into the $\Delta m_{\texttt{above}} << \Delta m_{\texttt{below}}$ requirement for the envelope mass. Solutions with $\Delta m_{\texttt{above}} > 0.1\ \Delta m_{\texttt{below}}$ were considered to be non-stationary. We note that the value of $\Delta m_{\texttt{below}}$ depends on the choice of the inner boundary for the wind base, and the classification of a particular solution may change with a different cut-off for the integration inwards or when imposing the nuclear burning shell conditions.[4] In every solution found, the photospheric velocity never exceeded a few percent of the speed of light ($v_{\rm ph} \lesssim 0.03\ c$), and so the special relativistic corrections are not needed. The hypothesis consistency criteria mentioned above are fairly common and can be found in several other works (see Joss & Melia 1987; Kato & Hachisu 1994).

The whole process can be repeated for different values of freely chosen model parameters ($\dot{M}, \dot{E}, M, X_i$). However, as it quickly became clear, not every combination of model parameters admits a solution. Some other combinations do admit numerical solutions, but they are not acceptable from a physical point of view and need to be further analyzed. Others may give solutions that comply with the main physical hypotheses but do not always adjust to NS scenarios. In fact, the same wind model equations, with similar boundary conditions but different computation methods and micro-physics input, were employed in the context of white dwarfs (see Kato & Hachisu 1994; Kovetz 1998). Even for a fixed stellar mass, M, and envelope composition, X_i, the remaining pair of mass and energy outflows ($\dot{M}, \dot{E}$) span a parameter space where all of the above cases are still possible. The region with valid solutions, in this 2-dimensional parameter space, also depends on the envelope composition (especially X_H) and the mass of the NS, and therefore is not known a priori. Section 2.4 sheds some light on these issues and helps to test the basic simulation code functionality.

[4] However, in Section 3.3.1, we implemented a different prescription for the calculation of characteristic time, following Guichandut *et al.* (2021).

2.4 Simulations results

Simulations were run for a wide range of values in the wind parameter space $(\dot{M}, \dot{E})$, exploring over 1000 points.[5] In all the simulations reported in this chapter, a neutron star mass of $M = 1.4\,\mathrm{M}_\odot$ has been adopted, together with an envelope of solar composition given by $X = 0$, $Y = 0.9$, $Z = 0.1$. These trial values for composition were the ones with the highest metallicity available in the opacity tables by OPAL that were employed for this preliminary study. We normalized the energy output $\dot{E}$ in terms of a constant Eddington luminosity

$$L_\mathrm{o} = \frac{4\pi c G M}{\kappa_\mathrm{o}(1 + X_\mathtt{H})}, \tag{2.22}$$

where $\kappa_\mathrm{o} = 0.2\ \mathtt{cm}^2\mathtt{g}^{-1}$ is the electron scattering opacity, and $X_\mathtt{H}$ is the hydrogen abundance. For a neutron star with $M = 1.4\ \mathrm{M}_\odot$ and no hydrogen in the wind envelope, $L_\mathrm{o} \simeq 3.51 \times 10^{38}\ \mathtt{erg\ s}^{-1} \simeq 9 \times 10^4\ \mathrm{L}_\odot$.

2.4.1 Wind profiles

A suite of different wind profiles is displayed in Figure 2.1. Each plot presents a selection of solutions that have a wind base compatible with a neutron star radius of $R_\mathrm{NS} = 13\ \mathtt{km}$. The first two plots in Figure 2.1 are solutions for velocity and temperature, respectively. The third plot is a profile of characteristic time Δt, which is the time it takes for a fluid element to reach the photosphere from a given radius. The bottom plot is the luminosity ratio $\Gamma = L_R/L_\mathtt{Edd}$ (where $L_\mathtt{Edd}$ is the local Eddington luminosity).[6]

The general pattern observed is that solutions with smaller energy outflows are characterized by larger radii, but also a higher mass output and longer characteristic timescales. This is due to the fact that a fluid element requires longer distances to accelerate to a sufficiently high velocity when its mass is larger or the available energy is smaller. Profiles with higher mass outflow (lower energy outflow) may not be suitable for describing short XRBs, since the total characteristic time (from wind base to photosphere) would be larger than the typical burst duration.[7]

Another significant behavior is that the radiative luminosity starts very low in comparison with the local Eddington limit at low radii, suggesting that the wind is driven by gas pressure rather than radiation in the inner regions. The luminosity ratio $\Gamma = L_\mathrm{R}/L_\mathrm{Edd}$ then rises sharply, before reaching the critical point and flattens very close to unity after that, remaining flat for the rest of the supersonic profile, except for some minor bumps (about 3% maximum excess) in some models close to the photosphere.

2.4.2 Parameter space exploration

Figures 2.2 to 2.4 show photospheric, critical point and wind base values, respectively, as a function of model parameters $(\dot{M}, \dot{E})$. Temperature and radius are plotted in all three figures.

[5] This large resolution was necessary to resolve a sequence of points in parameter space corresponding to solutions meeting wind base condition (Equation 2.19) at a desired $R_\mathrm{NS} = 13\ \mathtt{km}$ (see Section 2.4.2).

[6] Unlike L_o, defined in Equation 2.22, *Local* Eddington luminosity, $L_{Edd} = \frac{4\pi c G M}{\kappa(\rho, T, X_i)}$, is not constant. In some texts it is referred to as *critical* luminosity.

[7] This classification changes when using the different prescription for characteristic time we later implemented in Section 3.3.1, after Guichandut *et al.* (2021).

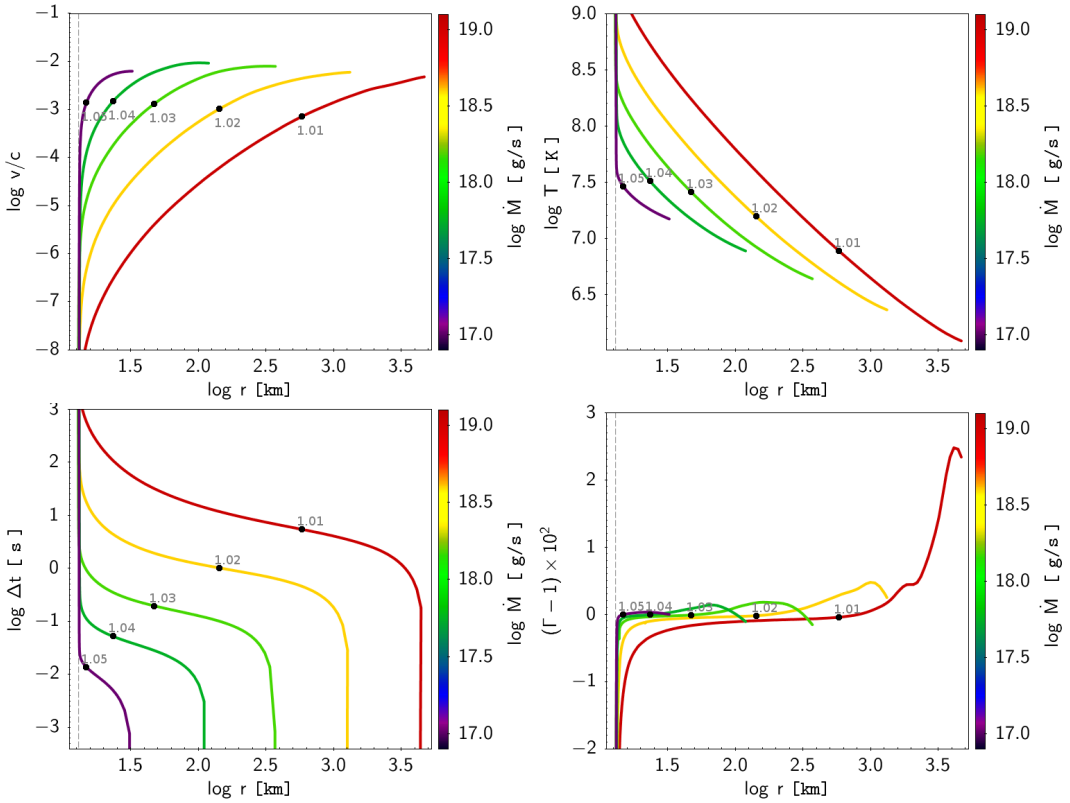

Figure 2.1: Wind profile solutions compatible with a neutron star radius of 13 km (vertical dashed line), with different values of parameters $(\dot{M}, \dot{E})$. Values of mass outflow $\dot{M}$ are indicated by the line color, and values of energy outflow $\dot{E}$, in units of $L_\circ$ (see text), are indicated with labels next to a black circle (•), which marks the location of the critical sonic point in each curve. Top to bottom: Velocity, temperature, characteristic time, and luminosity ratio Γ, all presented as a function of radius. All curves end at the photosphere.

Luminosity ratio Γ is plotted in photosphere and critical point figures ($\Gamma_{\rm wb} \simeq 0.5$ is constant, where "wb" stands for wind base). Wind velocity is only shown for the photosphere, because at the critical point, $v_{\rm cr}^2 \sim T_{\rm cr}$, and wind base values are negligible with values smaller than a few centimeters per second. Other relevant plots presented are effective optical depth τ^* for critical point only, and wind base density and characteristic time. All figures show both the acceptable (self-consistent) solutions and those discarded for being either optically thin or non-stationary solutions, according to the criteria explained in Section 2.3. The subset of acceptable solutions that are compatible with possible neutron stars is also indicated, as well as the solutions plotted in Figure 2.1. We note that the criterion for stationary wind depends on the ratio of envelope mass above and below the critical point, and thus the choice of the wind base affects this classification.

We observe a clear pattern: as energy output $\dot{E}$ increases and mass output $\dot{M}$ decreases, photospheric temperature rises, in the exact opposite fashion to the photospheric radius, which decreases. We study this correlation further below in Section 2.4.3. The photospheric

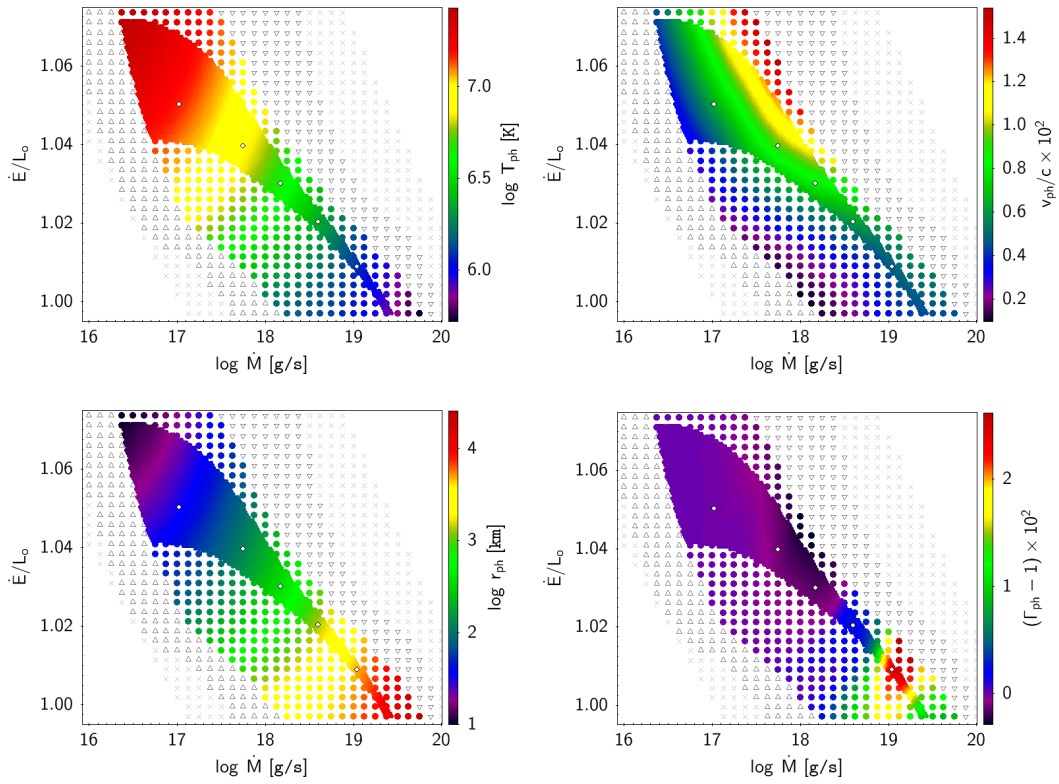

Figure 2.2: Wind parameter space sweep. Color coded values of photospheric magnitudes for different values of parameters $(\dot{M}, \dot{E})$. In reading order: temperature, velocity, radius and luminosity ratio Γ. Points marked with up or down triangles ($\triangle/\triangledown$) correspond to "thin" solutions and to non-stationary solutions, respectively. Points marked with filled circles ($\bullet$) are self-consistent solution candidates, the $\times$ mark denotes no solutions found for the given boundary conditions. Fully colored area marks solutions whose wind base is compatible with possible neutron star radii ($7 - 20$ km), and white diamonds inside of it ($\diamond$) mark selected solutions plotted in Figure 2.1.

wind velocity gradient with respect to parameters seems to be roughly orthogonal to that of temperature or radius, only achieving a few percent of speed of light, and peaking outside the self-consistent solutions zone. The photospheric radiative luminosity is very close to local Eddington luminosity, as shown by the Γ plot, except for low-energy and high-mass outflows, where it peaks at up to a 3% excess. This is due to a small bump in opacity tables that lowers the local Eddington luminosity.

As for the critical point (Figure 2.3), no obvious relationship between temperature and radius appears. The change in critical radius seems to go mostly inversely with $\dot{E}$, while the change in critical temperature seems to have a bigger component in the $\dot{M}$ direction, especially at high $\dot{E}$. By definition of critical point, a critical velocity plot would give the same information as the temperature one, instead we show a plot for effective optical depth. The critical point lies at higher optical depth with bigger mass outflow, hinting at a stretching of the envelope as mentioned above. The radiative luminosity is always close to the local

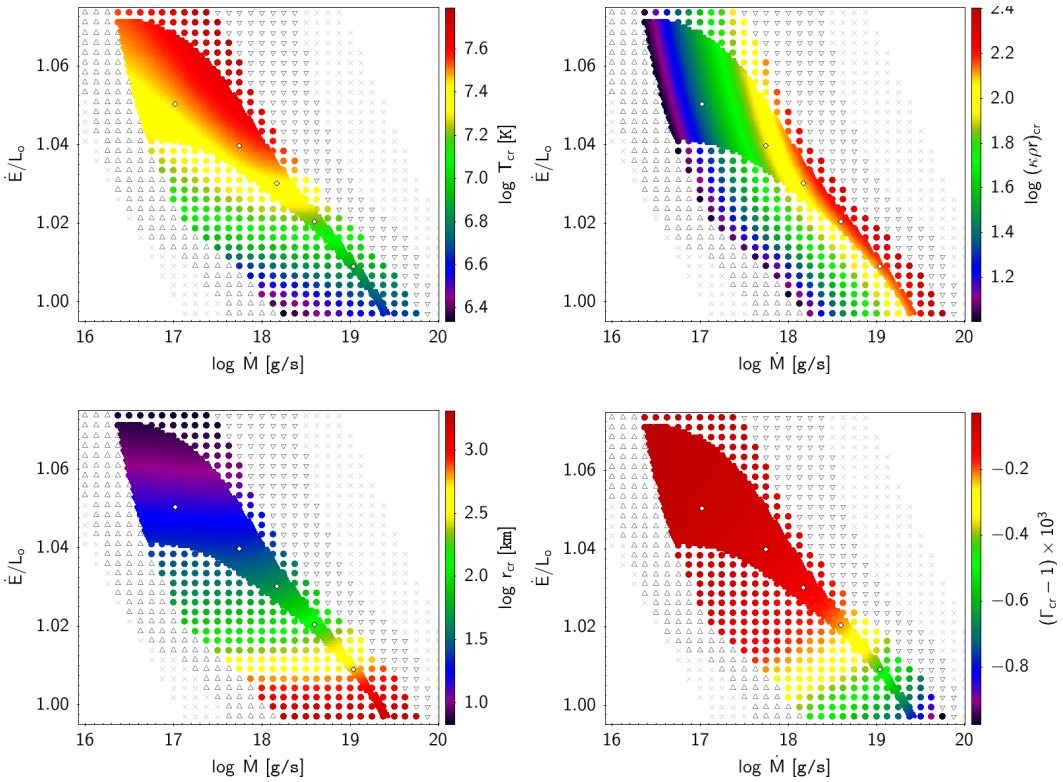

Figure 2.3: Same as Figure 2.2, but for values at the critical (sonic) point, with the exception of the velocity plot that has been replaced by an effective optical depth $\tau^* = \kappa\rho r$ plot.

Eddington limit, but just slightly lower, by no more than $\sim 0.1\%$.

The temperature and density values at the wind base (as defined by equation 2.19) are shown in Figure 2.4. Their values are in a reasonable range for XRBs conditions (see José *et al.* 2010; Fisker *et al.* 2008; Woosley *et al.* 2004) in the area of radial compatibility with neutron stars. However, not all of the models in this area have wind base characteristic times (i.e. the time required for a fluid element to reach the photosphere from the wind base) that are well suited for describing short XRBs, whose duration is of the order of few hundreds of seconds. These models could still represent winds in long-duration XRBs. Nevertheless, it is possible that the high values of Δt found are a result of the choice of the inner boundary condition, as mentioned in Section 2.3. In the profiles shown in Figure 2.1, the velocities quickly go to zero at the wind base, and therefore wind material spends nearly all its outflow time just above the wind base. This is probably an artifact of the time-independent treatment, which may no longer be accurate close to the inner boundary.

2.4.3 Photospheric correlations

A close correlation was found between several photospheric magnitudes across solutions. First, for most profiles, the photospheric luminosity was found to be almost equal to the local Eddington luminosity, as can be seen in Figure 2.5 where the distribution peaks sharply

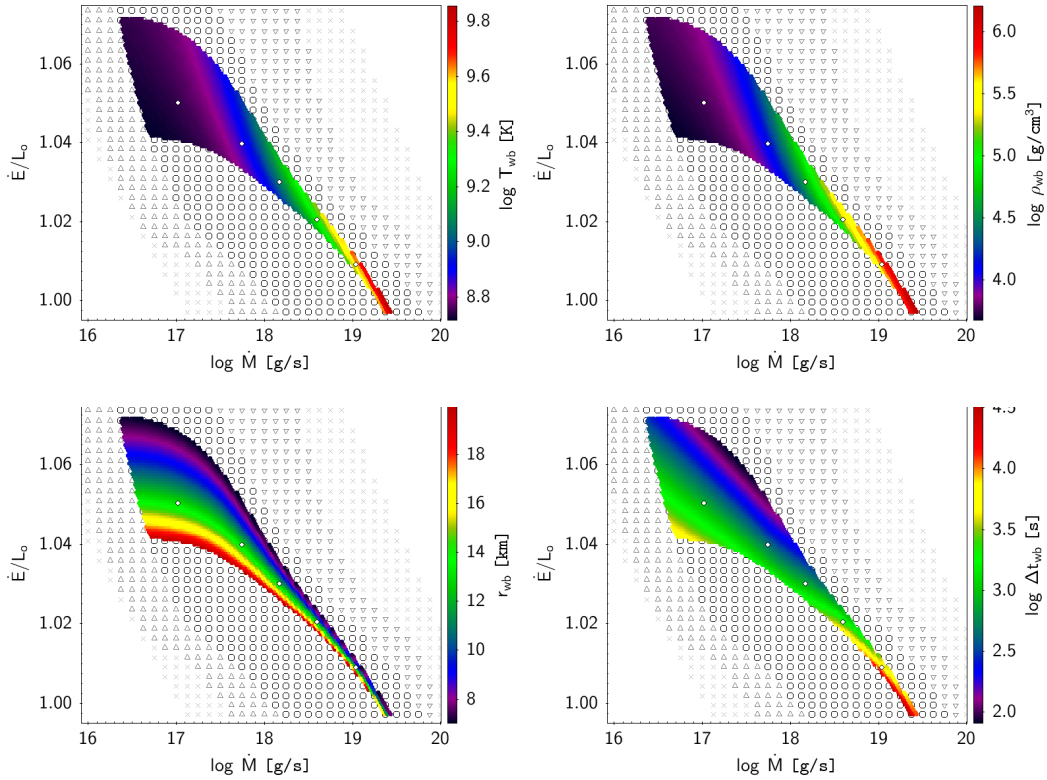

Figure 2.4: Same as Figure 2.2, but for values of temperature, density, radius, and characteristic time Δt at the wind base. Self-consistent solutions outside the area of compatibility with neutron stars are not colored here in order to better resolve values in the area of interest.

around $\Gamma_{\rm ph} = 1$, and the values expressed in terms of mean and standard deviation are: $\Gamma_{\rm ph} = 1.0018 \pm 0.0055$. This can also be seen in the color maps of the wind parameter space in Figure 2.2, where the coloring for photospheric Γ is mostly homogeneous, except for a small rise in the low-energy and high-mass outflows region where a bump in opacity table causes the local Eddington luminosity value to drop a little. The value of radiative luminosity (and therefore also opacity) at the photosphere also shows little variation across models, with the mean and standard deviation being: $L_{\rm R,ph}/L_{\rm o} = 1.025 \pm 0.022$ and $\kappa_{\rm ph}/\kappa_{\rm o} = 0.981 \pm 0.024$.

As both photospheric κ and $L_{\rm R}$ show very little variation, two correlations arise from the photospheric boundary conditions. Assuming a fairly constant $L_{\rm R}$, the effective temperature condition gives:

$$r_{\rm ph}^2 T_{\rm ph}^4 \simeq \texttt{const} \Longrightarrow T_{\rm ph} \sim {r_{\rm ph}}^{-1/2}. \tag{2.23}$$

Similarly, for the optical depth condition and $\kappa_{\rm ph} \simeq \texttt{const}$,

$$r_{\rm ph}\, \rho_{\rm ph} \simeq \texttt{const} \Longrightarrow \rho_{\rm ph} \sim {r_{\rm ph}}^{-1}. \tag{2.24}$$

Furthermore, by using both photospheric conditions, the equations for conservation of mass and energy, and assuming that the radiative luminosity is close to the Eddington limit,

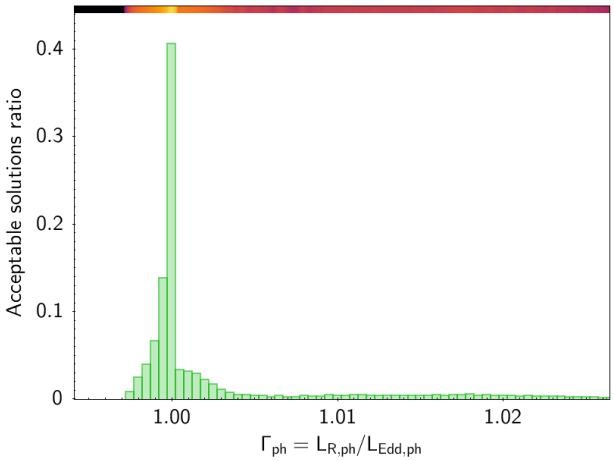

Figure 2.5: Distribution of photospheric luminosity ratio Γ across acceptable solutions with varying values of model parameters.

we can arrive at the following expression, which relates observable photospheric magnitudes with wind model parameters.

$$\frac{8}{3}\frac{v_{\rm ph}}{c} = \frac{GM}{r_{\rm ph}}\frac{\dot{M}}{L_{\rm R,ph}} \simeq \frac{\dot{E}}{L_{\rm R,ph}} - 1. \tag{2.25}$$

Such correlations can be derived considering the following. First, using mass conservation to replace $\dot{M}$, and assuming $L_{\rm R} = L_{\rm Edd} = \frac{4\pi cGM}{\kappa}$, it is easy to see that:

$$\frac{\dot{M}}{L_{\rm R}}\frac{GM}{r} = 4\pi r^2 \rho v \frac{GM}{r}\frac{\kappa}{4\pi cGM} = \kappa\rho r\frac{v}{c}. \tag{2.26}$$

This relationship is valid whenever the luminosity is equal to the local Eddington limit. Further, particularly at the photosphere, using the optical condition, we have:

$$\frac{\dot{M}}{L_{\rm R,ph}}\frac{GM}{r_{\rm ph}} = \frac{8}{3}\frac{v_{\rm ph}}{c}. \tag{2.27}$$

This accounts for the first equality of expression 2.25.

Now let us take the energy conservation equation and rewrite it in the form:

$$\frac{\dot{E}}{L_{\rm R}} - 1 = \frac{\dot{M}}{L_{\rm R}}\frac{GM}{r}\left(\frac{v^2}{u^2} + \frac{5s^2}{u^2} + \frac{8}{3}\frac{aT^4}{\rho u^2} - 1\right), \tag{2.28}$$

where we have introduced the notation $s^2 = \frac{kT}{\mu m_A}$ for local sound speed and $u^2 = \frac{2GM}{r}$ for escape velocity. For the wind to be optically thick, the critical point must lie at much greater optical depth than the photosphere. Since the critical point is the place where the wind becomes supersonic, this often translates into having $v^2 >> s^2$ at the photosphere. Lastly, in almost every solution obtained here, photospheric escape velocity is still around one order of magnitude above wind velocity, which means $s^2 << v^2 << u^2$. The last relation

is relaxed as $\dot{M}$ increases and $\dot{E}$ decreases. So far, neglecting the corresponding terms we have at the photosphere:

$$\frac{\dot{E}}{L_{\rm R}} - 1 = \frac{\dot{M}}{L_{\rm R}} \frac{GM}{r} \left(\frac{8}{3} \frac{aT^4}{\rho u^2} - 1 \right). \tag{2.29}$$

If we now use the photospheric boundary conditions rewritten in a convenient form:

$$ar^2T^4 = \frac{L_{\rm R}}{\pi c} \qquad \text{and} \qquad \frac{8}{3}\frac{1}{\rho r} = \kappa, \tag{2.30}$$

by taking the product of both and dividing by $4GM$, we get:

$$\frac{2}{3}\frac{aT^4 r}{\rho GM} = \frac{\kappa L_R}{4\pi c GM} \qquad \text{or} \qquad \frac{4}{3}\frac{aT^4}{\rho u^2} = \frac{L_{\rm R}}{L_{\rm Edd}}, \tag{2.31}$$

and if again $L_{\rm R} = L_{\rm Edd}$, we get at the photosphere:

$$\frac{8}{3}\frac{aT^4}{\rho u^2} = 2. \tag{2.32}$$

By replacing this value in equation 2.29 we arrive finally at the relation

$$\frac{\dot{E}}{L_{\rm R,ph}} - 1 \simeq \frac{\dot{M}}{L_{\rm R,ph}} \frac{GM}{r_{\rm ph}}, \tag{2.33}$$

which is the second equality in expression 2.25.

For solutions for which the approximation $v^2 << u^2$ weakens, one should add the term corresponding to wind kinetic energy $\frac{\dot{M}v^2}{2L_{\rm R,ph}}$:

$$\frac{\dot{E}}{L_{\rm R,ph}} - 1 \simeq \frac{8}{3}\frac{v_{\rm ph}}{c} + \frac{\dot{M}c^2}{2L_{\rm R,ph}} \left(\frac{v_{\rm ph}}{c}\right)^2, \tag{2.34}$$

where we used relation 2.27 to write the equation in terms of v/c. As $v << c$, and photospheric luminosity varies weakly across solutions ($L_{\rm R,ph} \sim L_{\rm o}$), the correction term will only become relevant for relatively high values of $\dot{M}$, that is, if:

$$\frac{8}{3} \sim \frac{\dot{M} c v_{\rm ph}}{2L_{\rm R,ph}}. \tag{2.35}$$

2.5 Summary and discussion

In the previous section, we present several results, including a set of wind profiles (solutions for the wind model), a high-resolution parameter space exploration characterizing different physical magnitudes at points of interest, and several correlations found for photospheric (observable) values.

The wind profiles found in this work (Sect. 2.4.1 and Fig. 2.1) are qualitatively similar to those found in previous works (see, e.g., Quinn & Paczyński 1985). These previous studies frequently relied on an approximated expression for the opacity, in the form:

$$\kappa_{(T)} = \kappa_{\rm es}(1+X)\left[1 + (\alpha T)^{\xi}\right]^{-1} \tag{2.36}$$

where $\kappa_{\rm es} = 0.2$ $\mathtt{cm}^2\mathtt{g}^{-1}$ is the electron-scattering opacity, X is the hydrogen mass fraction, $\alpha^{-1} = 4.5 \times 10^8$ $\mathtt{K}$, and ξ is a parameter for which different values haven been adopted: $\xi = 1$ (by Kato 1983; Ebisuzaki *et al.* 1983), $\xi = 0.86$ (by Quinn & Paczyński 1985). Figure 2.6 shows a comparison of the opacity profiles obtained for several solutions reported in this work with values obtained through the approximate Eq. 2.36 in some of the aforementioned previous studies. Equation 2.36 neither takes into account the expected density dependence nor metallicity effects.[8] According to more recent studies, a high concentration of heavy elements is expected in the envelope after XRBs (see, for example, José *et al.* 2010; Woosley *et al.* 2004; Fisker *et al.* 2008), and therefore high opacity. The inclusion of updated opacity tables was a necessary improvement in this regard.

At sufficiently high temperatures (close to the wind base), opacity drops considerably in all prescriptions, making the contribution of radiation to wind acceleration less important, while favoring the effect of gas pressure. As temperature and density drop outwards, the gas pressure gradient diminishes, while the opacity increases, lowering the local Eddington limit. As a result, the wind is further accelerated and sustained by radiation. This increase in opacity is higher close to the photosphere with opacity tables than those reported in previous studies, even for the trial $Z = 0.1$ used in this work. The differences may seem relatively small here, namely on the order of a few percent, but they are expected to rise even more for higher metallicity. As we plan to study stellar winds with higher metallicities and different mixtures of heavy elements given by XRBs simulations in Chapter 3, we consider the inclusion of opacity tables to be an important step towards that goal.

With regard to the parameter space exploration presented in this work (Sect. 2.4.2, Figs. 2.2 to 2.4), it served two purposes. The first was to find the regions for which acceptable solutions exist for the wind model used, by testing part of the assumed hypothesis (i.e., optically thick and stationary wind), in a similar way to Quinn & Paczyński (1985). The main improvement in this regard is the number of solutions obtained in the present work with respect to these latter authors. This allows for a higher resolution, which helps, for instance, to better determine these regions. The other purpose of the parameter space exploration was the characterization of physical magnitudes at points of interest, especially at the photosphere (high resolution enabled this too). The dependence of these photospheric values on the wind parameters serves as a link between the physics of the layers close to the base of the envelope and observable magnitudes at the photosphere in the following way: The parameters explored, namely mass and energy outflow $(\dot{M}, \dot{E})$, are fully determined when imposing suitable boundary conditions for all physical variables at the base of the wind envelope. To this end, we would need to rely on hydrodynamic XRB models of the underlying layers, where nuclear reactions take place. This is presented in Chapter 3. In order for the current wind model to be applied safely and consistently, the boundary conditions provided by a given XRB model should result in mass and energy outflows that lie in the acceptable region. Once the parameters are fixed at the base by the XRB model, the corresponding wind solution gives the values of each observable magnitude at the photosphere. However, each value of a single photospheric magnitude taken separately does not uniquely determine the $(\dot{M}, \dot{E})$ pair.

The correlations found in Section 2.4.3 (Equation 2.25) relate the photospheric magnitudes (that can either be directly observed or calculated from observable ones) with model parameters $(\dot{M}, \dot{E})$ in a more direct and unique way. For instance, the radiative luminosity

[8] See, however, Joss & Melia (1987); Paczyński (1983), for other density-dependent prescriptions which still do not include metallicity effects.

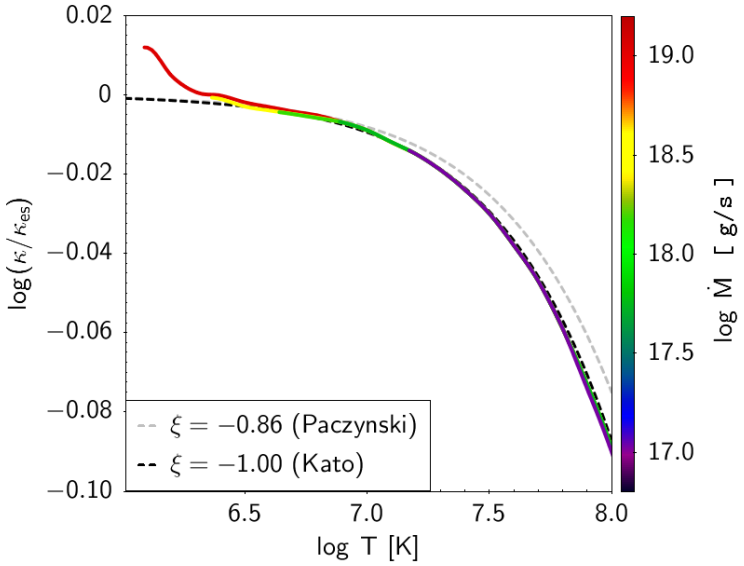

Figure 2.6: Opacity profiles vs. temperature. Wind solutions obtained in this work (continuous lines) with wind base at $R_{\rm NS} = 13$ km and different values of $\log \dot{M}$. Other prescriptions adopted in previous studies (dashed lines) with different values of ξ (see text), are also shown for comparison. Opacity is normalized to $\kappa_{es} = 0.2$ cm^2/g.

L_R can be estimated if the distance to the XRB source is known, while wind velocity v could be estimated from the Doppler shift in spectral absorption lines during the XRB. With both velocity and luminosity, one could calculate the total energy outflow $\dot{E}$ by means of Eq. 2.25. An estimate of photospheric temperature (e.g., by fitting a blackbody frequency distribution for the spectrum), can be used to calculate the photospheric radius by means of the $r \sim T^{-2}$ photospheric correlation or directly through the definition of effective temperature (Eq. 2.13). Once we have r, v, and L_R at the photosphere, calculation of the mass outflow $\dot{M}$ is possible through Eq. 2.27, or from the mass conservation (Eq. 2.1) with the density given by the $\rho \sim r^{-1}$ photospheric correlation. Furthermore, since nuclear reactions in XRBs take place at the interface of the envelope with the neutron star core, these correlations could provide a technique for determining the radius of the neutron star indirectly by observation of the photospheric magnitudes alone.

In summary, here we explore the possible solutions of a nonrelativistic radiative wind model in a typical XRB scenario at high resolution in the parameter space $(\dot{M}, \dot{E})$. The wind profiles suggest a transition from gas pressure (in the inner regions) to radiation pressure (as the wind becomes supersonic) as the main driving mechanism. The inclusion of updated micro-physics data with higher metallicities and higher opacities, is important here because it reinforces the role of radiation in the wind acceleration, facilitating the above-mentioned transition. Radiative luminosity was found to remain very close to the local Eddington limit in this regime, and at the photosphere in particular. A high correlation was found between different observable (photospheric) magnitudes and the model parameters. These correlations can be used to link observational data to the physical conditions of the underlying layers where nuclear reactions take place. However, given some of the simplifying hypothesis

of the model (non-relativistic regime, optically thick wind, LTE, etc.), it remains to be determined whether or not these correlations hold once more complex studies are performed. Hydrodynamic models of XRBs with nuclear reactions are required to impose boundary conditions at the base of the wind envelope and will determine the model parameters. This is the main topic of the next chapter.

Chapter 3

Matching stellar winds with XRB hydrodynamic simulations

The stellar wind models presented so far have free parameters that can be adjusted to different physical situations. In the previous chapter we explored a subset of possible wind solutions that are compatible with a very general boundary condition expected at the base of the envelope (Eq. 2.19), for neutron stars with radius lying within a wide possible range ($7 - 20$ km). We found that, for a particular neutron star radius of 13 km, a sequence of solutions aligned in the parameters space, with correlated energy and mass outflows. Although these values were within the expected ranges for an XRB, no specification was made on whether these solutions corresponded to actual XRB conditions or how do they evolve in time. In this chapter we connect the stellar wind models to a more realistic burst scenario as described through the XRB hydrodynamic models developed in previous studies by other members of this group. These XRB hydrodynamic models simulate the nuclear reactions and more complicated hydrodynamical processes, undergone by the continuously accreted material, that take place at the innermost parts of the envelope, close to the neutron star crust.

The objective is to determine if the physical conditions given by the XRB hydrodynamic models are suitable for a stellar wind to appear at some point during the evolution of the burst. In other words, we want to find if there is a compatible match between the possible wind profiles, obtained as solutions of the model developed in the previous chapters, and the boundary values given as a result from the XRB hydrodynamic models. These extra boundary conditions will constrain the free parameters in the wind model, and could determine a unique wind profile at each time, in case a solution exists. If successful, the ultimate goal is to study the consequent mass-loss and predicted observable magnitudes. Our particular interest is set towards determining whether this potential mass-loss has an impact on the galactic abundances of the light p-nuclei isotopes mentioned in the introduction (Sect. 1.3), namely ^{92,94}Mo and ^{96,98}Ru.

We are going to work under the assumption that the chemical composition of the wind envelope will be determined by the XRB hydrodynamic models at each matching point, and it does not change across the wind profile for a fixed time. Since each matching point candidate has different composition, often reaching high metallicity values, the opacity tables provided by OPAL, with fixed abundances and limited to low metalicity, are no longer useful. Instead,

our stellar wind code had to be modified to use tables provided by The Opacity Project (See App. B.2), which allows us to change the composition rapidly. Another aspect to take into consideration is the fact that the wind and XRB models differ in some key features and basic hypotheses. For instance, the wind model describes a stationary regime, while XRB models are time dependent. However, if the evolution of XRB conditions is slow enough, under some criteria, a matching sequence of steady wind solutions could still be considered as a good quasi-stationary approximation. Convective energy transport, degenerate matter contributions to the equation of state, and energy generation are also only contemplated in the XRB hydrodynamic models, since they were not necessary for wind models. These issues will be taken into consideration when assessing the validity of the match.

This chapter is organized as follows. An overview of the XRB hydrodynamic models is presented in Sect 3.1, summarizing the most relevant features and results in relation to our objective. Section 3.2 contains a description of the method developed to match wind model solutions to XRB hydrodynamic simulations data. An analysis of the match results, their validity and consequences regarding observational features, mass-loss and contribution to the galactic medium of the isotopic abundances of interest follows in Sect. 3.3.

3.1 X-ray bursts hydrodynamic models

The XRB hydrodynamic models analyzed in this work were developed by José *et al.* (2010). They perform a series of simulations of XRB evolution by coupling a nuclear reaction network, that includes 324-isotopes linked by 1392 possible reactions, into a modified version of the *SHIVA* hydrodynamic evolution code (see José & Hernanz 1998; José 2016). The code uses Lagrangian formulation (i.e., the computational grid is attached to the moving fluid), as opposed to the Eulerian formulation used in the stellar wind model, where the coordinate system is fixed relative to the neutron star. The main features and hypotheses of these models are: spherical symmetry, Newtonian gravity, and energy transport by radiative diffusion and convection. Equation of state includes contributions from the electron gas (with different degrees of degeneracy), the ion plasma, and radiation; Coulomb corrections to the electronic pressure are also taken into account. Energy generation rates consider both the input from the aforementioned nuclear reaction network, and losses due to neutrino emissions.

The XRB models present the evolution of physical data in a discrete grid of equal mass shells, and time-steps of varying duration. Variables reported in each (shell,time-step) grid point include (see Fig. 3.1): radial coordinate of the shell's mid-point, temperature, density, total luminosity (including all energy outflow contributions), fluid velocity, and mass fractions for the 324 isotopes. They computed several models, varying parameters such as: neutron star mass $M_{\rm NS}$ (and its corresponding radius, $R_{\rm NS}$, according to most accepted equation of state models), metallicity of the accreted material, Z, and grid resolution. All XRB models features are summarized in Table 3.1.

In the present work we will focus on two different models including a total of five bursts: four consecutive bursts of a 55-shells model (model # 1 in Table 3.1), which we will refer to as XRB-1 to XRB-4, and one burst corresponding to the 200-shells model # 2 (which we will call XRB-A). The rest of parameters are equal in both models, namely: $M_{\rm NS} = 1.4\,{\rm M}_\odot$, $R_{\rm NS} = 13.1$ `km`, accreted material of solar composition with metallicity $Z = 0.02$ and an accretion rate of $1.75 \times 10^{-9}\,{\rm M}_\odot/$`yr` (that is 1.1×10^{17} `g/s`). The models also differ in the resulting time-step resolution, with above 20000 steps for the 200-shells burst, and an average of about 8000 steps per burst for the 55-shells model. This implies an almost ten-fold

increase in grid-points resolution in favor of model XRB-A.

Model input parameters					Resulting burst features				
#	Shells	$M_{\rm NS}$ ($\rm M_\odot$)	$R_{\rm NS}$ (km)	Z	τ_{rec} (hr)	$\tau_{0.01}$ (s)	T_{pk} (10^9K)	L_{pk} ($10^5 \rm L_\odot$)	α
1	55	1.4	13.1	0.02	5.9	75.8	1.06	0.97	60
					6.4	62.3	1.15	1.7	40
					4.9	55.4	1.26	2.1	34
					5.1	75.7	1.12	1.2	36
2	200	1.4	13.1	0.02	5.9	59.2	1.05	0.9	62
					4.6	73.9	1.20	1.5	31
3	55	1.4	13.1	10^{-3}	18.1	423	1.40	1.0	34
					9.4	296	1.39	1.1	24
					8.9	281	1.32	0.98	24
					8.9	252	1.30	1.0	27
					8.8	250	1.26	1.0	30
4	55	1.8	17.0	0.02	9.3	62.3	1.03	1.7	77
					8.5	46.3	1.08	2.6	46
					8.9	59.5	1.1	2.1	45

Table 3.1: Main features of the XRB hydrodynamic models published by José *et al.* (2010). Model input parameters indicated once per model (left side) are: model original number denomination, shell grid resolution, neutron star mass and radius, and metallicity of the accreted material (all models have an accretion rate of $1.75 \times 10^{-9}\,\rm M_\odot/yr$). Resulting features for each subsequent burst (right side): recurrence time (τ_{rec}), burst duration ($\tau_{0.01}$), peak temperature, peak luminosity, and burst over persistent luminosity ratio (α).

Both models studied here also show similar resulting features: burst recurrence times ranging in about $5 - 6.5$ hr, burst durations of $55 - 75$ s, peak luminosities within $\sim [1-2] \times 10^5 L_\odot$, and peak temperatures in $[1 - 1.25] \times 10^9$ K. They also report qualitatively similar light curves and, with few exceptions, a good agreement in terms of nucleosynthesis. Therefore, they concluded that a resolution of 55 shells was appropriate to describe the XRB evolution, in agreement with other related studies (Fisker *et al.* 2008; Woosley *et al.* 2004). However, a high resolution in the XRB becomes important when trying to match stellar wind solutions, as it will become clear in our analysis throughout the rest of this chapter.

Other model variants they reported include: a five-bursts model (# 3) with low metallicity accreted matter ($Z \sim 10^{-3}$), and another three-bursts model (# 4), back with $Z = 0.02$, but occurring on a more massive and bigger neutron star ($M_{\rm NS} = 1.8\,\rm M_\odot$, $R_{\rm NS} = 17$ km). Both these models were computed with a 55-shells grid resolution. When compared to the first two models, the low metallicity model # 3 was characterized by longer burst durations, within $\sim 250 - 300$ s (except the first burst, which lasted over 400 s), and longer recurrence periods of around 9 hr (18 hr, for the first). Peak temperatures were slightly higher, $1.26 - 1.4 \times 10^9$ K, while peak luminosities varied little around $10^5 L_\odot$. On the other hand, model # 4 with the more massive neutron star also showed burst durations of about 1 min, as in the other models with $Z = 0.02$, but with long recurrence times of ~ 9 hr, as in the lower metallicity one. Its peak temperatures were back to the slightly lower range of $1 - 1.1 \times 10^9$ K, but their peak luminosities were closer to $2 \times 10^5 L_\odot$.

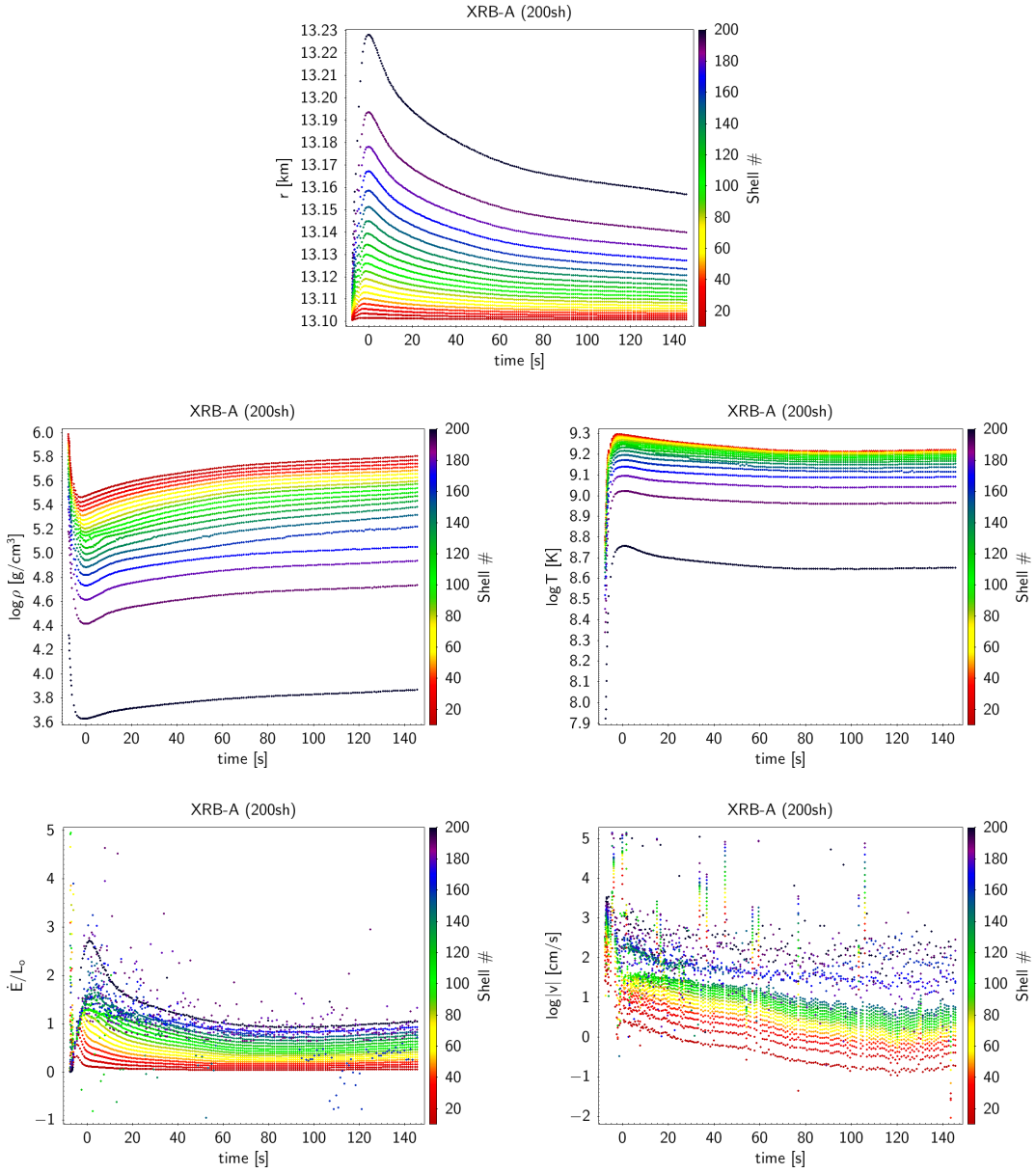

Figure 3.1: Time evolution of the first burst in the 200-shells model # 2 (XRB-A), published by José *et al.* (2010). Shell number is indicated by dot color. Panels in reading order are: radius, temperature, density, total energy outflow, $\dot{E}$, in terms of Eddington luminosity $L_o = 3.52 \times 10^{38}$ `erg/s`, and absolute value of velocity. Time coordinate origin corresponds to peak radial expansion.

Upon comparison with other similar studies, they concluded that the burst properties depend weakly on the neutron star mass. In contrast, the role played by metallicity of the accreted material is significantly stronger, resulting in longer recurrence and decline times, lower peak luminosities, higher peak temperatures, and smaller burst over persistent luminosity ratio, α, when the accreted material has lower metallicity.

Despite the high resolution employed (for the computational power available when these models were developed), some of the variables exhibit significant fluctuation. Sometimes this "noise" can spread considerably apart from the average value evolving in each shell, with several out-laying points even orders of magnitude away. The two main problematic magnitudes in this regard are fluid velocity and total luminosity (see Fig. 3.1 bottom panels).

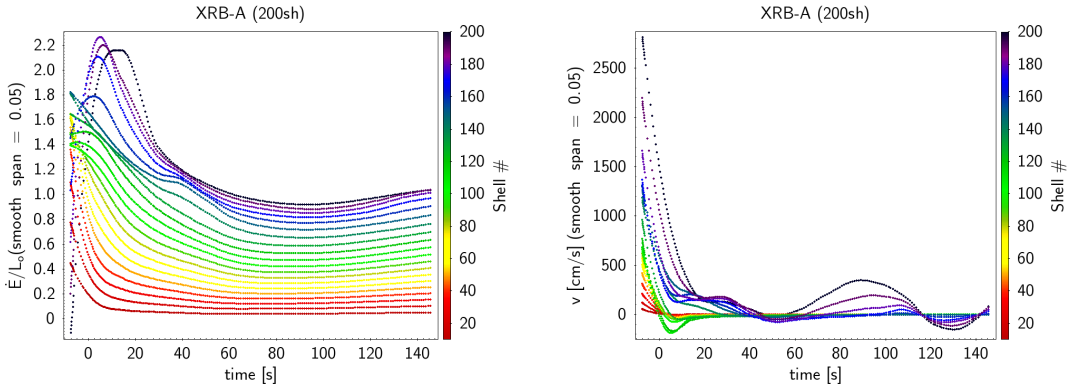

Figure 3.2: Time evolution of smoothed data (model XRB-A). Left: Energy outflow $\dot{E}$ in terms of Eddington luminosity $L_o = 3.52 \times 10^{38}$ `erg/s`; and right: velocity. Shell number is indicated by dot color. Time coordinate origin corresponds to peak radial expansion.

A smoothing process, relying on local regression, was applied for the affected variables and is explained in Appendix A.6. Figure 3.2 shows an example of the smoothed variables. For each smoothed variable, the root mean squared deviation of the original values with respect to their smoothed counterparts was computed. Its ratio to the overall average of the smoothed value was considered as a measure of the original data noise. For total luminosity, $\dot{E}$, this noise ratio was relatively small, giving ~ 0.02 for XRB-A, and between ~ 0.02 and ~ 0.07 for bursts in the lower resolution model. However, for the velocity, this noise ratio was considerably larger: 0.2 for XRB-A, and between ~ 0.45 and ~ 2.33 for the other bursts. This makes the velocity data unreliable and practically useless for our analysis in the search for stellar wind, especially in the lower resolution models. The lower noise ratios of the higher resolution model XRB-A, makes it our favorite candidate for seeking a match with wind profiles. We will focus the search on this burst in particular for the rest of this chapter. The lower resolution bursts, XRB-1 to XRB-4, corresponding to the similar model # 1, will be analyzed in Appendix C. Models # 3 and # 4 will remain for future work.

3.2 Wind-burst matching method

In order to determine whether any of the XRB hydrodynamic models may lead to a stellar wind, we need to find if the physical conditions at any point are compatible with

both the XRB and the wind models. Ideally, at a given matching point, all relevant physical variables should be continuous functions. However, given that both models have different hypotheses corresponding to different physical regimes (and therefore have differing terms in their equations) the ideal match may not always be sensible or possible. For instance, we can not expect a realistic match whenever degenerate gas pressure or convection are relevant terms in the equations of XRB hydrodynamic models, given that they are not present in the wind models. Nevertheless, whenever the conditions are such that these terms can be neglected, we could expect to find a valid match.

Another aspect to take into consideration is whether energy or mass outflows, $\dot{E}$ and $\dot{M}$, resulting from the conditions in the XRB hydrodynamic model, lie in the region of the wind parameter space where solutions can be found and are consistent with the wind model hypotheses. In this regard, the study of the wind parameter space discussed in the previous chapter resulted of great significance. It is worth keeping in mind, though, that the location and shape of this region also depends on the abundances of elements present in the envelope, especially hydrogen, and on the mass of the neutron star. The latter is fixed for the subset of XRB hydrodynamic models considered in this work, but the former changes dynamically within the evolution of each XRB and across its shells.

As it was seen in Section 2.4, the shape of the wind profiles (and therefore the possible values of every variable at the desired matching radius) depends on the wind parameters mentioned before. For some cases, the wind solution may not even reach the desired radius without quickly rising in temperature above physically reasonable values. Conversely, imposing an additional boundary condition at a desired radius (for instance a given value of temperature), restricts the possible solutions in the parameter space.[1] In the aforementioned study we did a similar thing by demanding an approximate value for $\nabla P_g / \nabla P_R \simeq 1$. In order to successfully match a sequence of steady wind profiles to a particular XRB evolution, we would then have to explore any possible free parameter in search for a matching boundary condition at each time step. For fixed element abundances X_i and neutron star mass M, the remaining free parameters are the energy and mass outflows, $\dot{E}$ and $\dot{M}$, which can be uniquely determined by imposing two additional boundary conditions, for instance the temperature and density, at a particular radius.

The energy outflow $\dot{E}$ and the elements abundances X_i are determined by the XRB hydrodynamic models at each point of their shell/time-step grids. So are the temperature and density, which will be used as target boundary conditions. However, given that the velocity data showed high fluctuation (see Section 3.1), it can not be relied on. For this reason, the mass outflow $\dot{M}$, which depends on the velocity through the mass conservation equation 2.1, will be considered as a free parameter. As seen in Section 3.1, the energy outflow $\dot{E}$ varies with radius, so the other free parameter will be the matching radius, since the envelope in the XRB hydrodynamic models extends over a few meters above the neutron star core. In practice, finding the matching radius translates into finding which shell has a better match.

The general idea for the matching procedure employed is as follows. For a given XRB hydrodynamic simulation, we explore the shell/time-step grid, focusing first on every point with an energy outflow $\dot{E}$ that lies within the range of acceptable wind solutions in the parameter space. Since this range depends on the current element abundances and its exact extension is not known a priori, a typically safe and reduced region is chosen in terms of the ratio $\dot{E}/L_X$, for a first of several grid sweeps. In each sweep, every selected grid point is

[1] This is analogous to the energy values becoming discrete in a bound quantum harmonic oscillator.

tested for a possible match by trying different wind profiles with varying mass outflows $\dot{M}$, while the rest of the wind parameters $(\dot{E}, X_i)$ is fixed to those given by the current XRB simulation grid point, until we find the one that matches one of the boundary conditions. For this step (let us call it "first" match) we chose a match in density.[2] That is, we use a suitable root-finding method to find zeros of the following δ_ρ function that parametrizes the match relative error as a function of the mass outflow:

$$\delta_\rho(\dot{M}) = \frac{\rho_W(\dot{M})}{\rho_B} - 1 \tag{3.1}$$

where the subindices W and B stand for "wind" and "burst" (i.e., from the hydrodynamic simulation) values at the matching radius, respectively. Grid points where $\delta_\rho < 0.01$ are considered successful first matches or "hits".

The valid domain for $\dot{M}$ is not known a priori. Root-finding methods like the commonly used Newton-Raphson are not well suited for the task since they not only may wander outside any initial guess of a valid domain, but they also require finding the derivative of the δ_ρ function, which demands calculating additional wind model solutions at each step. A custom root-finding algorithm (dubbed *IRIS*), based on the safer (but often slower) bisection method, was developed for dealing with this problem, and it is described in Appendix A.4.

After the first sweep is completed, the exploration is sequentially extended to previously unexplored grid points that lie adjacent to those for which a "hit" was found, by means of a battleship-like algorithm explained in Appendix A.5. The whole process is repeated until no further hits are found. The aim is to avoid missing out possible hits outside the first guessed safe region, while at the same time preventing the exploration to waste efforts (and computing time) by unnecessarily testing points with parameters outside the wind model acceptable region.

At each point, we also compute a "second" matching error for temperature, δ_T, with an expression analogous to Eq. 3.1, in order to construct the total matching error:

$$\delta = \sqrt{\delta_\rho^2 + \delta_T^2}. \tag{3.2}$$

Grid points where this match error was $\delta < 0.01$, are then considered to be successful XRB-wind matches. Matching points are tested for hypothesis consistency in both XRB hydrodynamic and wind models.

One could argue that a second root-finding algorithm could be employed instead, in order to determine a more precise matching radius in each time-step. First, that would require the interpolation of all physical variables between shells (including the more than 300 isotope abundances). And secondly, it also requires performing one additional root-finding in the first matching variable for each of the intermediate steps of the second root-finding. Furthermore, we could even use a 2-dimensional root-finding method to tackle both matching variables at the same time. The problem is that commonly used N-dimensional root-finding methods also suffer from the same inadequacies as the 1-dimensional Newton-Raphson and similar methods explained before. In order to be successfully applied to this case, a 2-dimensional root-finding method would need similar characteristics as the aforementioned

[2] Several pairs of matching variables could be used here ((ρ, T), (P_R, P_g), etc), and in any order. Which variable is chosen for the first match will affect the precision requirement of the root-finding employed, as well as the overall error obtained for the second match. After trying several combinations, we found that the best results for the method employed, in terms of number of matches, speed and matching errors, is obtained with the ordered pair (ρ, T).

IRIS algorithm. That is, we would need a generalization of a bisection-based method to two dimensions which, as far as we know, does not exist. Nevertheless, we managed to develop a method with such features, called *SiSect*, which is described in Appendix A.4. This was the first method we tried in order to find the matching wind solutions more precisely, before we decided to switch to the method described in the previous paragraphs. After a few trials, we concluded that the resulting improvement in precision was not worth the required extra computing time and effort in tunning the method's parameters. However, with further study and some improvements, we believe that the *SiSect* method can become a powerful tool with numerous applications, and it was worth including in this work.

3.3 Results analysis

The search for XRB-wind model matching points was successful for some of the XRB hydrodynamic simulations studied. This means that, under the considered hypotheses and approximations, these XRB hydrodynamic models give way to a brief stellar wind and the consequent mass-loss. Results for the 200-shells model XRB-A will be analyzed here, while the 55-shells models, XRB-1 to XRB-4, will be described in Appendix C.

3.3.1 Wind-burst matching solutions

The wind-burst matching analysis of the 200-shells hydrodynamic burst model, XRB-A, resulted in the sequence of matching points shown in Fig. 3.3. It shows a very well defined progression from the inner (hotter and denser) layers to the outer (cooler and less dense) ones and allows us to reconstruct a continuous evolution of all physical variables, if needed. The matching error (Eq. 3.2) for these points was significantly low: $\delta < 0.01$. The resulting mass outflow, $\dot{M}$, color-coded in Fig. 3.3, evolves from higher values at the inner matching layers, diminishing as the match moves outwards, until no further match was found. Matching points for deeper layers (and earlier time) than the ones shown can be found in practice, with the same method. However, in that direction, the XRB models enter a region of temperature and density where the effects from electron degeneracy and energy generation from nuclear reactions become significant. Convective energy transport also becomes relevant in deeper layers. Wind model does not contemplate these effects, therefore possible matches towards deeper layers were not explored further.

The distribution of matching solutions in the wind parameter space is shown in Fig. 3.4. At a first glance, the sequence of matching points display a similar distribution in parameter space to the one found in Sect 2.4.2 (see, for instance, Fig. 2.4 bottom-left panel), but the overall energy outflow is slightly higher here. Wind parameters are now normalized in terms of a non-constant Eddington luminosity corresponding to electron-scattering, L_X, which depends on local hydrogen mass fraction, X, as:

$$L_X = \frac{4\pi c G M}{\kappa_o (1+X)} \simeq \frac{3.52 \times 10^{38}}{(1+X)} \ \mathtt{erg\ s^{-1}} \tag{3.3}$$

with $\kappa_o = 0.2\ \mathtt{cm^2 g^{-1}}$, as opposed to Chapter 2 where $X = 0$ and normalization was therefore constant. Otherwise, each of the matching points would deviate slightly from the observed aligned disposition, according to their corresponding hydrogen abundance. We can also follow the time evolution of the parameters now, given by the color scale. Wind total energy

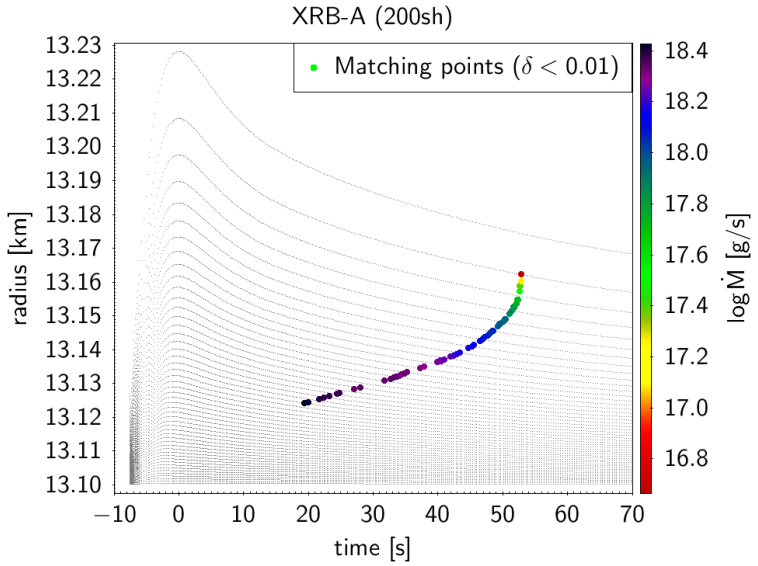

Figure 3.3: Wind matching points during XRB evolution (model XRB-A). Grey dotted lines show the radial expansion of each XRB model shell as a function of time. Points for which matching wind solutions were found ($\delta < 0.01$, see text) are marked with colored circles. Color indicates mass outflow $\dot{M}$ of the matching wind solution.

outflow evolves from lower to higher values, as opposed to mass outflow. The matching point time progression in the parameter space is slower for earlier times and speeds up considerably in the final few seconds.

A selection of radial profiles, for some of the matching wind solutions, is shown in Fig. 3.5. Again, the time progression is indicated with the color scale. The profiles show similar features to the ones reported in Sect. 2.4.1. The main difference is that the overall radial extension of the wind profiles shown here is smaller, which is characteristic of wind solutions with higher energy outflows. The radial extension of the wind envelope shrinks with time, as it is made evident by the position of the critical (sonic) point and photosphere, indicated in each profile. This is expected for the final part of the wind evolution, where the expanded wind envelope should recede and finally meet the original boundaries reported by the XRB hydrodynamic models, as the wind stops.

Values of wind velocity at the photosphere and critical point do not vary much ($v_{\mathtt{ph}} \sim 10^{-2}c$, $v_{\mathtt{cr}} \sim 10^{-3}c$) for most of the duration of the wind, in a similar way to the solutions reported in the previous chapter (See Fig. 2.1). Temperature values at these points are also similar ($\log T_{\mathtt{ph}}(\mathtt{K}) \sim 6.5 - 7$, $\log T_{\mathtt{cr}}(\mathtt{K}) \sim 7.5$), minding the fact that now the profiles extend only to about 500 $\mathtt{km}$, corresponding to $\log r(\mathtt{km}) \simeq 2.7$ in Fig 2.4.1. The radiative luminosity ratio profiles, $\Gamma = L_R/L_{Edd}$, also exhibit a similar behavior to the ones reported in the previous chapter. They all show a sharp rise close to the envelope base, quickly stabilizing outwards around a value of $\Gamma \sim 1$, with tiny variations of about 10^{-3}. This is also a sign of a quick change from gas pressure-driven to radiation-driven wind.

A characteristic time plot is also shown. This time we employed a different prescription for calculating it. In Section 2.4.1 we showed a characteristic time plot (Figure 2.1 bottom

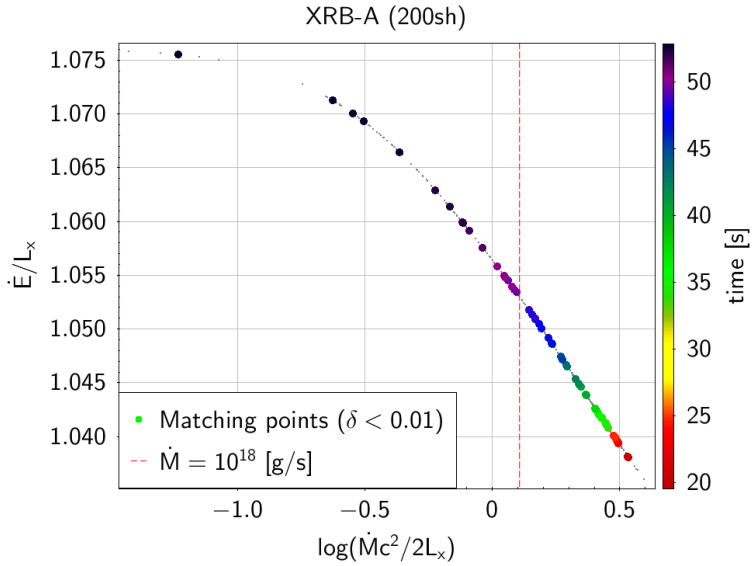

Figure 3.4: Evolution of Wind-Burst matching points in parameter space (for model XRB-A). Colored dots represent matching points with relative error $\delta < 0.01$. Color scale corresponds to time since burst peak expansion. Both energy outflow, $\dot{E}$, and mass outflow, $\dot{M}$, are normalized in terms of Eddington luminosity in the electron scattering case, L_X (see text). A reference value for $\dot{M} = 10^{18}$ `g/s` is indicated by a vertical dashed red line.

left panel), following the prescription used by Quinn & Paczyński (1985) and expressed in Equation 2.21. However, according to Guichandut *et al.* (2021), this flow time is not a good measure of the feasibility of the quasi-stationary approach. They stated the problem is that it is highly dominated by the very slow wind velocity at the wind base. Instead, they proposed a combined characteristic time using the much higher sound speed for the subsonic part, and the regular wind speed for the supersonic part, giving a much smaller characteristic time than the typical wind duration. That is:

$$\Delta t_d = \int_{r_{\rm wb}}^{r_{\rm cr}} \frac{\mathrm{d}r}{c_s} + \int_{r_{\rm cr}}^{r_{\rm ph}} \frac{\mathrm{d}r}{v} \tag{3.4}$$

where Δt_d is this new *dynamic* time, c_s is the sound speed, and the other symbols have the usual meaning. The reasoning behind this choice can be understood as follows. A small change in physical conditions at the base can be thought of as a perturbation from the stationary regime solution. This perturbation will travel at the speed of sound as long as the flow is subsonic, readjusting the profile in its way up, and will travel with the flow velocity when it is supersonic. This effectively means that Δt_d is associated to the propagation speed of information through the wind envelope. As long as this information travel time is small enough compared to the duration of the wind, we can consider the quasi-stationary regime as a good approximation. Given the fact that $\Delta t_d < 0.5$ `s` in all profiles, and that the duration is above 30 `s`, we can safely conclude that the quasi-stationary hypothesis holds.

A detailed view of the match between temperature profiles from wind and XRB hydrodynamic models is displayed in Fig. 3.6. There, one can graphically appreciate not only the precise match in temperature at different times, but also the fact that the temperature

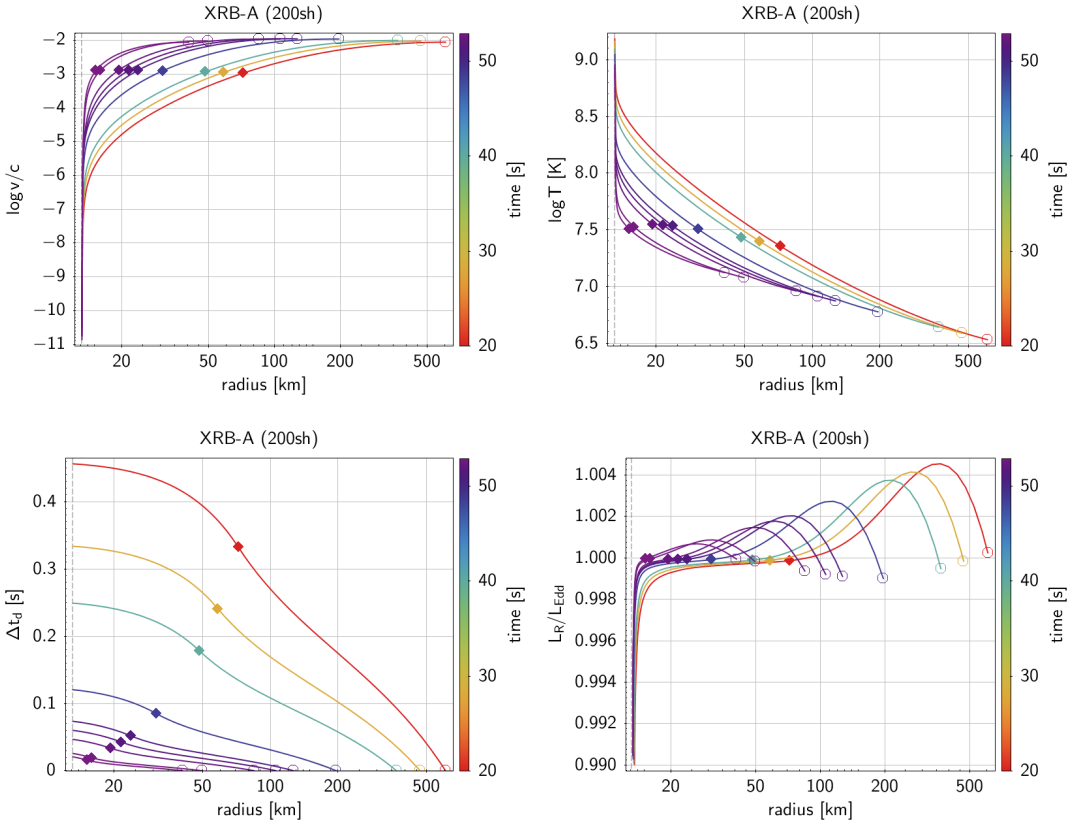

Figure 3.5: Wind profiles obtained (for model XRB-A). Time evolution is indicated by line color. Locations of the critical sonic point (⧫) and photosphere (○) are indicated in each curve. Panels in reading order are: velocity, temperature, characteristic time, and luminosity ratio Γ, all plotted as a function of radius. Neutron star radius is 13.1 `km` (vertical dashed line).

gradient in both models has a similarly continuous value. This feature is expected if convection is negligible, making diffusion the only relevant term in the energy transport equation. However, the same can not be said for the density match. Despite the match in density being more accurate in most cases, the density gradient is not continuous. A density gradient appears in the mass conservation equation, and this discontinuity may originate in a significant contribution to integrated mass outflow from the time-dependent term. Alternatively, it may derive from the different choice of photospheric boundary conditions in XRB hydrodynamic models, $P = P_{\rm Rad}$, $T = T_{\rm eff}$, usual for non-expanded static envelopes, and the fact they do not admit mass-loss. These conditions can shape radial profiles differently, especially in upper shells close to the boundary, where the jump in density gradient seems to be more prominent.

3.3.2 Mass-loss and contribution to galactic abundances

Now that a sequence of matching points has been found, we can take a look at the chemical composition present at those points. This will be, under our working hypothesis,

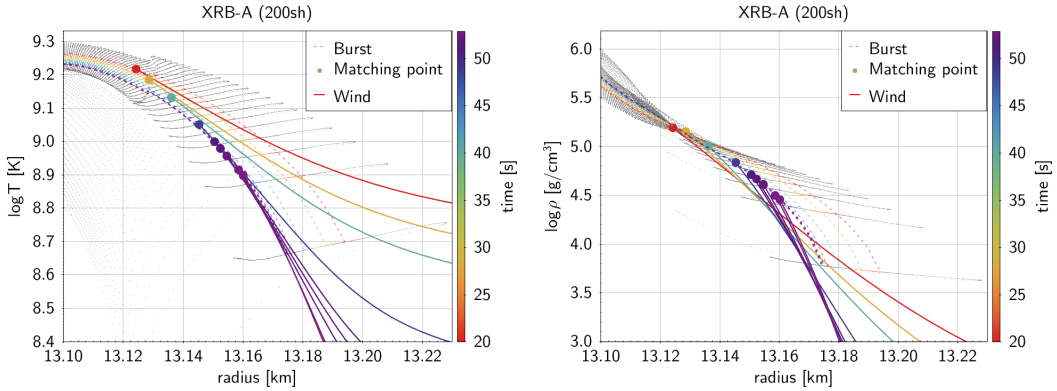

Figure 3.6: Detailed match of temperature (left) and density (right) radial profiles between wind and hydrodynamic model XRB-A. Each wind profile is indicated with a continuous colored line, while dashed colored lines indicate their matching counterparts in the XRB model. Burst-Wind profiles matching points are indicated with big circles. Color scale indicates the time since burst peak expansion. Gray dots indicate the rest of unmatched XRB points.

the composition of the wind envelope. Every isotope present in it would ride this wind and escape the neutron star gravitational potential into the interstellar medium.

Our especial interest is on some p-nuclei mentioned before (^{92,94}Mo, ^{96,98}Ru). However, there are other unstable isotopes also produced during the XRB that eventually decay into the ones we are interested in. In this regard, the unstable isotopes with the most significant production are ^{92}Pd, ^{94}Ag, and, ^{98}In.

In order to calculate the total mass-loss for each species, Δm_i, we need to integrate the mass outflow rate of every isotope, $\dot{m}_i(t)$, with respect to time, and over the duration of the wind. That is, for every isotope denoted with subindex i, we would like to obtain a numerical approximation of the following integral:

$$\Delta m_i = \int_{t_o}^{t_f} \dot{m}_i(t)\, dt = \int_{t_o}^{t_f} \dot{M}(t) X_i(t)\, dt \tag{3.5}$$

where $\dot{M}(t)$ is the total mass outflow as a function of time, which corresponds to each wind solution obtained matching parameter, and t_o and t_f are the initial and final times of the wind.

Although the accuracy of the match was relatively high in model XRB-A, with a significantly low matching error of $\delta < 0.01$, the matching points still show some degree of fluctuation in most physical variables and irregularity in time distribution (see Fig 3.7, for instance). In some of the time-steps, more than one matching point from neighboring shells was found within the allowed matching error. For other times none was found, even in-between others with a match, where a continuous evolution is expected. This represents an inconvenience when trying to numerically integrate eq. 3.5. Such irregularities may happen when the matching point moves between shells that involve an abrupt enough change of physical conditions, to which the match is very sensitive. Points around where this occurs give larger matching error and the candidate shells are left out, while points with a smoother change give multiple nearby shells as acceptable matching solutions. Decreasing the accuracy requirement of the matching method populates both empty time-steps and the ones

with multiple matching shells at the same time. The study on the lower resolution models (App. C), showed that this issue is worsened. An even higher grid resolution, which could better resolve the changes in physical conditions to which the match is very sensitive and allow using a smaller δ threshold, may help to improve on this issue in the future.

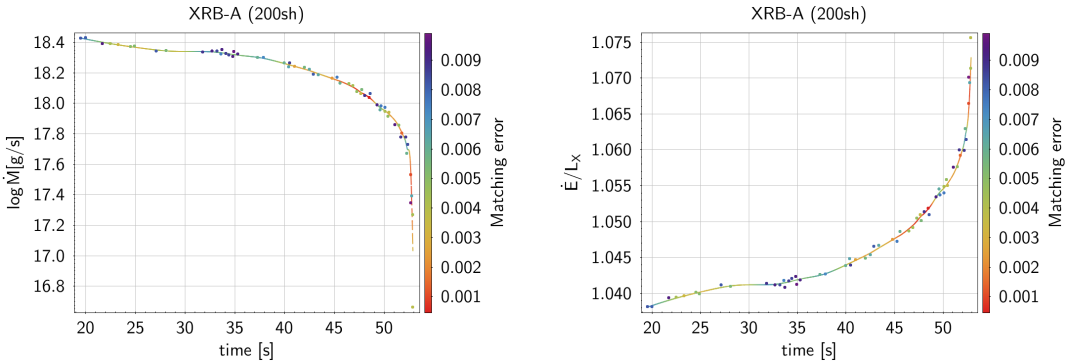

Figure 3.7: Time evolution of mass outflow, $\dot{M}$ (left), and energy outflow, $\dot{E}$ (right), in model XRB-A, and predictive curves using smoothing-interpolating technique (see text). Wind-burst matching data points are indicated with dots, and predicted values with a line. Color scale indicates the matching error obtained (dots) or expected (lines), respectively.

In order to overcome this inconvenience with the data available in the present work, we performed the following results post-processing. A smoothing technique using local regression (see App. A.6) is applied, similarly to the one employed to treat the noisy variables from the original XRB hydrodynamic simulations in Section 3.1. This time, though, we can use the matching error as a weight factor in the form $\omega = \delta^{-2}$, so that the smoothing favors points with smaller error. This fixes the fluctuation in densely populated time intervals. Then, a smooth interpolation was used to reconstruct a curve. This serves two purposes: first, it fills up time gaps where sequences of potential matching points would lie in-between shells; and secondly, to get a large enough amount of equally distributed points to better approximate the integral in equation 3.5. Figure 3.7 shows both the matching point data and this smooth-interpolating predictive curve, for the mass outflow, $\dot{M}$, and total energy outflow, $\dot{E}$. The matching error for the interpolated points was also predicted using the same method and is color-coded in the predictive curves.

The same technique was applied to every physical variable and all isotopic abundances. Here we will focus on the latter and leave the analysis of the rest of physical variables for the following Section 3.3.3. Figure 3.8 shows both the predicted time-evolution curves and matching data points of mass outflow rates for the species of interest, and their time-integrated ejected mass. It is worth mentioning here that, although the matching technique could still be applied to find earlier matching points (this was dismissed due to hypothesis inconsistency between models, see Sect. 3.3.1), the mass outflow rate for each of the isotopes seems to drop a few orders of magnitude in that direction, as shown in the left panel of Fig. 3.8. Consequently, the contribution of earlier matching points may be of little significance for the time-integrated ejected mass of these isotopes. The same cannot be said for the total mass outflow, whose value seems to slightly increase backwards in time. However, it is expected to go back down by the time of the wind actual onset (compare with the lower resolution models analyzed in Appendix Section C.2). The total mass yield obtained is

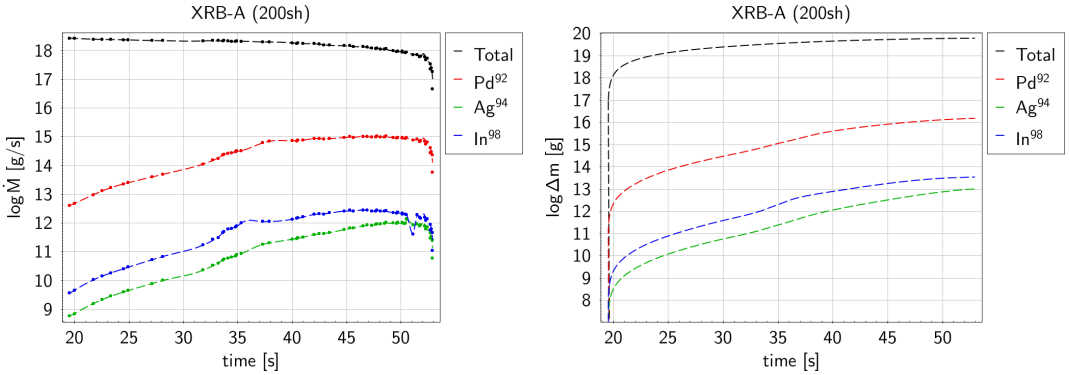

Figure 3.8: Left: Time evolution of mass outflow ($\dot{M}$) for some species of interest (see text) and total mass outflow. Wind-Burst model matching points are indicated with dots, the predictive curve (dashed line) is also shown for each of them. Right: Time-integrated ejected mass (Δm) for the same isotopes. Both panels correspond to model XRB-A.

$\Delta m = 6.16 \times 10^{19}$ g $= 3.1 \times 10^{-14}$ $M_\odot$, for the time interval analyzed.[3] Considering that model XRB-A has a recurrence time of 5.9 hr, and assuming no period of inactivity (i.e., an upper limit to its real contribution), this implies a yearly output of $4.6 \times 10^{-11}\,M_\odot/\mathrm{yr}$, that is 2.6% of the mass-accretion rate.

Figure 3.9 shows the total mass yield of every isotope produced in the XRB and ejected by the stellar wind. Mass yield is color-coded only for species with a mass output $\Delta m_i > 10^{10}$ g. Values for the top ten mass-yielding isotopes are shown in Table 3.2 (left panel). Most of the isotopes produced in the XRB are unstable and will eventually decay (mainly through β process) into stable ones. The final resulting stable isotopes were also computed, by simply adding the mass of each progenitor species. Almost 90% of the total expelled mass is constituted by the first four isotopes listed in the table: ^{60}Ni, ^{64}Zn, ^{68}Ge, ^{56}Ni, as seen in the right panel of Table 3.2. All ten species shown in the table account for over 97% of the overall mass ejected.

The mass yields of all the final stable isotopes are shown in Fig 3.10, with the p-nuclei species of our concern highlighted. Their mass yields were: $\Delta m_{92\mathrm{Mo}} = 1.57 \times 10^{16}$ g, $\Delta m_{96\mathrm{Ru}} = 5.75 \times 10^{15}$ g, and $\Delta m_{98\mathrm{Ru}} = 4.72 \times 10^{15}$ g, for the duration of the wind, which corresponds to mass fractions of: $X_{\mathrm{Mo92}} = 2.57 \times 10^{-4}$, $X_{\mathrm{Ru96}} = 9.33 \times 10^{-5}$, and $X_{\mathrm{Ru98}} = 7.67 \times 10^{-5}$, with respect to the total XRB mass-loss. With a burst recurrence time of $\tau_{rec} = 5.9$ hr, this gives annual yields of: $1.18 \times 10^{-14}\,M_\odot/\mathrm{yr}$, $4.29 \times 10^{-15}\,M_\odot/\mathrm{yr}$, and $3.53 \times 10^{-15}\,M_\odot/\mathrm{yr}$, respectively.

The remaining question is how significant is the XRB wind contribution we found for the observed Galactic abundance of these light p-nuclei species. Current measurements in primitive meteorites (see Lodders *et al.* 2009, and references therein) report the following abundances: $X^{\mathrm{Sol}}_{\mathrm{Mo92}} = 9.27 \times 10^{-10}$, $X^{\mathrm{Sol}}_{\mathrm{Ru96}} = 2.59 \times 10^{-10}$, and $X^{\mathrm{Sol}}_{\mathrm{Ru98}} = 8.80 \times 10^{-11}$. For an estimation of the XRB wind contribution to the Galactic abundances, the total net mass of each element ejected by the XRB winds must be compared to the total mass of that

[3] Without considering any contribution from possible earlier matching point. In that case, bearing in mind the analogous results found in Appendix Section C.2, a quick extrapolation for the estimated mass yield could be twice as much.

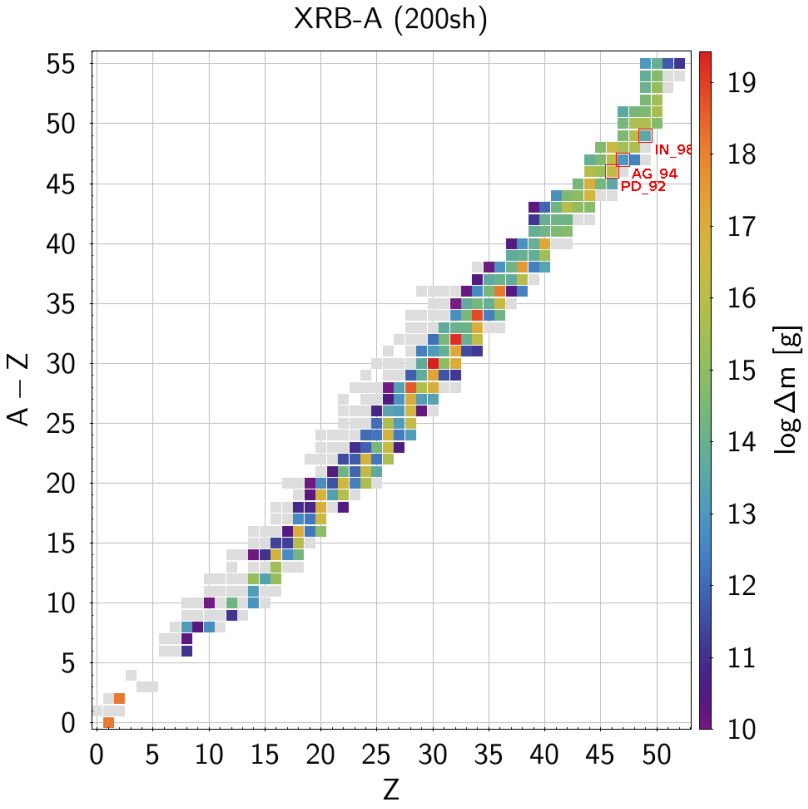

Figure 3.9: Mass ejected per isotope for the overall duration of the wind, from model XRB-A. The atomic number, Z, is indicated in the horizontal axis, while the neutron number, $N = A - Z$, is indicated in the vertical axis. Color scale indicates the mass ejected only for isotopes for which $\log \Delta m > 10$, the rest is gray. Some species of interest are also marked.

Produced isotopes

Sym	Z	A	Mass (g)	Fraction
Zn	30	60	2.71×10^{19}	4.39×10^{-1}
Ge	32	64	1.70×10^{19}	2.76×10^{-1}
Se	34	68	6.99×10^{18}	1.13×10^{-1}
Ni	28	56	4.20×10^{18}	6.82×10^{-2}
He	2	4	1.47×10^{18}	2.38×10^{-2}
Kr	36	72	1.42×10^{18}	2.31×10^{-2}
H	1	1	1.29×10^{18}	2.09×10^{-2}
Sr	38	76	4.04×10^{17}	6.56×10^{-3}
Zn	30	59	2.11×10^{17}	3.43×10^{-3}
Ge	32	63	1.48×10^{17}	2.40×10^{-3}

Final stable isotopes

Sym	Z	A	Mass (g)	Fraction
Ni	28	60	2.71×10^{19}	4.39×10^{-1}
Zn	30	64	1.70×10^{19}	2.76×10^{-1}
Ge	32	68	6.99×10^{18}	1.13×10^{-1}
Ni	28	56	4.20×10^{18}	6.82×10^{-2}
He	2	4	1.47×10^{18}	2.38×10^{-2}
Se	34	72	1.42×10^{18}	2.31×10^{-2}
H	1	1	1.29×10^{18}	2.09×10^{-2}
Kr	36	76	4.04×10^{17}	6.56×10^{-3}
Ni	28	59	2.11×10^{17}	3.43×10^{-3}
Cu	29	63	1.48×10^{17}	2.41×10^{-3}

Table 3.2: Top ten isotopes by mass yield, from stellar wind in model XRB-A. Left panel: isotopes directly produced in XRB nuclear reactions. Right panel: final stable isotopes after radioactive decay. All 10 isotopes shown account for $\sim 97.6\%$ of the total mass-loss, of which the top 5 constitute $\sim 92\%$.

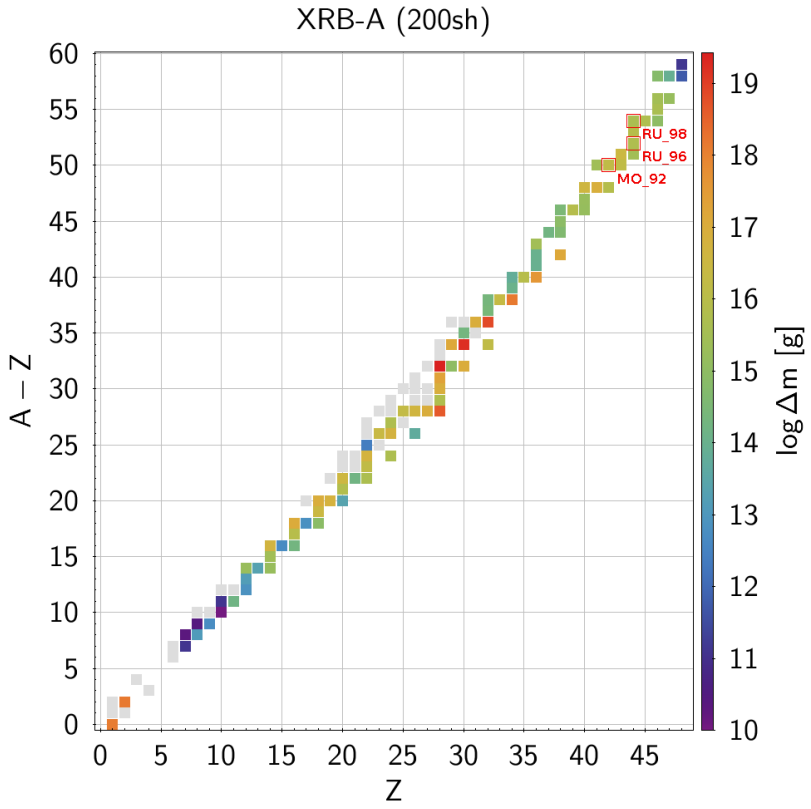

Figure 3.10: Stable isotopes mass yield from stellar wind in model XRB-A. This corresponds to the final products from radioactive decay of the unstable isotopes shown in Fig 3.9.

Isotope	^{92}Mo	^{96}Ru	^{98}Ru
XRB-A wind mass yield per burst (g)	$1.57 \cdot 10^{16}$	$5.75 \cdot 10^{15}$	$4.73 \cdot 10^{15}$
XRB-A annual yield ($M_\odot$/yr)	$1.18 \cdot 10^{-14}$	$4.29 \cdot 10^{-15}$	$3.53 \cdot 10^{-15}$
XRB-A wind mass fraction X_i	$2.57 \cdot 10^{-04}$	$9.33 \cdot 10^{-05}$	$7.67 \cdot 10^{-05}$
XRB-A life-time contribution ($M_\odot$)	$5.88 \cdot 10^{-05}$	$2.15 \cdot 10^{-05}$	$1.76 \cdot 10^{-05}$
Solar system X_i	$9.27 \cdot 10^{-10}$	$2.59 \cdot 10^{-10}$	$8.80 \cdot 10^{-11}$
Isotope mass presence in MW ($M_\odot$)	$1.85 \cdot 10^{02}$	$5.17 \cdot 10^{01}$	$1.76 \cdot 10^{01}$
Sources like XRB-A required to match	$3.15 \cdot 10^{06}$	$2.41 \cdot 10^{06}$	$9.98 \cdot 10^{05}$

Table 3.3: Estimates of light p-nuclei isotopes contribution from XRB-A wind to the galactic abundances. XRB-A is considered to be active through all the galactic age (13.5×10^9 `yr`). Total galactic mass used for calculations is 2×10^{11} $M_\odot$ (see text).

element present in the Galaxy. A raw estimate can be obtained in the following way (results are summarized in Table 3.3). The total observable mass of the Milky Way is believed to lie in the range of $[100 - 400] \times 10^9\,\mathrm{M}_\odot$.[4] Assuming a value of 200×10^9 $\mathrm{M}_\odot$, and the mass fractions inferred from meteoritic samples in our solar system, we get the following estimates for the amount of those p-nuclei present in our Galaxy: $\Delta m^{\mathtt{MW}}_{92\mathrm{Mo}} = 185$ $\mathrm{M}_\odot$, $\Delta m^{\mathtt{MW}}_{96\mathrm{Ru}} = 51.7$ $\mathrm{M}_\odot$, and $\Delta m^{\mathtt{MW}}_{98\mathrm{Ru}} = 17.6$ $\mathrm{M}_\odot$, where the "MW" supraindex stands for Milky Way. Now, assuming that all XRB sources contribute with a similar chemical abundance pattern than Model XRB-A, and assuming no periods of inactivity (i.e., all sources experience one burst after 5.9 hr, continuously throughout their entire lifetime), we can get an estimate of the overall mass contribution for each species to the galactic abundance, by simply multiplying the annual yields by the estimated lifetime of X-ray binaries (5 `Gyr`).[5] This results in: $\Delta m^{\mathtt{XRB}}_{92\mathrm{Mo}} = 1.59 \times 10^{-4}$ $\mathrm{M}_\odot$, $\Delta m^{\mathtt{XRB}}_{96\mathrm{Ru}} = 5.8 \times 10^{-5}$ $\mathrm{M}_\odot$, and $\Delta m^{\mathtt{XRB}}_{98\mathrm{Ru}} = 4.76 \times 10^{-5}$ $\mathrm{M}_\odot$. The ratio between the amount of each species in the Galaxy and the amount ejected by all XRB sources in the overall duration of the Galaxy (i.e. $\Delta m_i^{\mathtt{MW}} / \Delta m_i^{\mathtt{XRB}}$) yields an estimate of the number of XRB sources similar to XRB-A needed to account for the origin of these p-nuclei. This ratio gives different results for each isotope. Between a few hundred thousand to over a million sources like XRB-A are needed to match. In contrast, the total number of identified XRB sources so far is around one hundred.[6] That is, assuming that XRBs are the only source for these species and that our XRB-A is a representative case, then $10^3 - 10^4$ times more sources than the ones already discovered would be needed to explain the observed mass abundances of these light p-nuclei. This suggests that the origin of these light p-nuclei in XRBs (as their major contributors) is unlikely.

3.3.3 Observables, correlations and other physical magnitudes

Another important aspect we would like to analyze from the XRB-wind matching results is the evolution of observable features and how they relate to other predicted physical variables. Since the study of model XRB-A does not show the complete wind evolution (due to some mismatch between the XRB hydrodynamic and wind models hypothesis explained in Sect. 3.3.1), the analysis of lower resolution models, XRB-1 to 4, in Appendix C can supplement it and help build a more complete picture. In this regard, the results post-processing employed for calculating the mass-loss in Section 3.3.2 was extremely useful in order to extract a likely prediction from the less accurate matches in the lower resolution models. All plots displayed in this section will show dots for the actual values corresponding to matching wind profiles, and lines for the predicted curves using this previously mentioned smoothing-interpolating technique.

Time-evolution of photospheric magnitudes is shown in Fig. 3.11. Photospheric radial expansion is receding from over 600 `km`, steadily for most of the time interval displayed, and drops rapidly in the last few seconds, seemingly towards the final XRB-wind matching radius (~ 13.17 `km`), close to the NS core surface. Effective temperature appears to evolve in an exactly inverse manner, rising from around 4×10^6 `K` in the earlier moments where

[4] Here, we consider only baryonic matter, no dark matter estimate is included.

[5] This is a traditionally assumed value for X-ray binaries lifetime, but it is currently not very well constrained. More recent works suggest much shorter lifetimes, by even 3 orders of magnitude (see Iben *et al.* 1995; Podsiadłowski *et al.* 2002; Pfahl *et al.* 2003). In such case, our final conclusion (see further ahead) is strengthened, since even more XRB sources would be needed to explain the observed mass abundances.

[6] See `http://www.sron.nl/~jeanz/bursterlist.html` for an updated list of known galactic type I XRB systems.

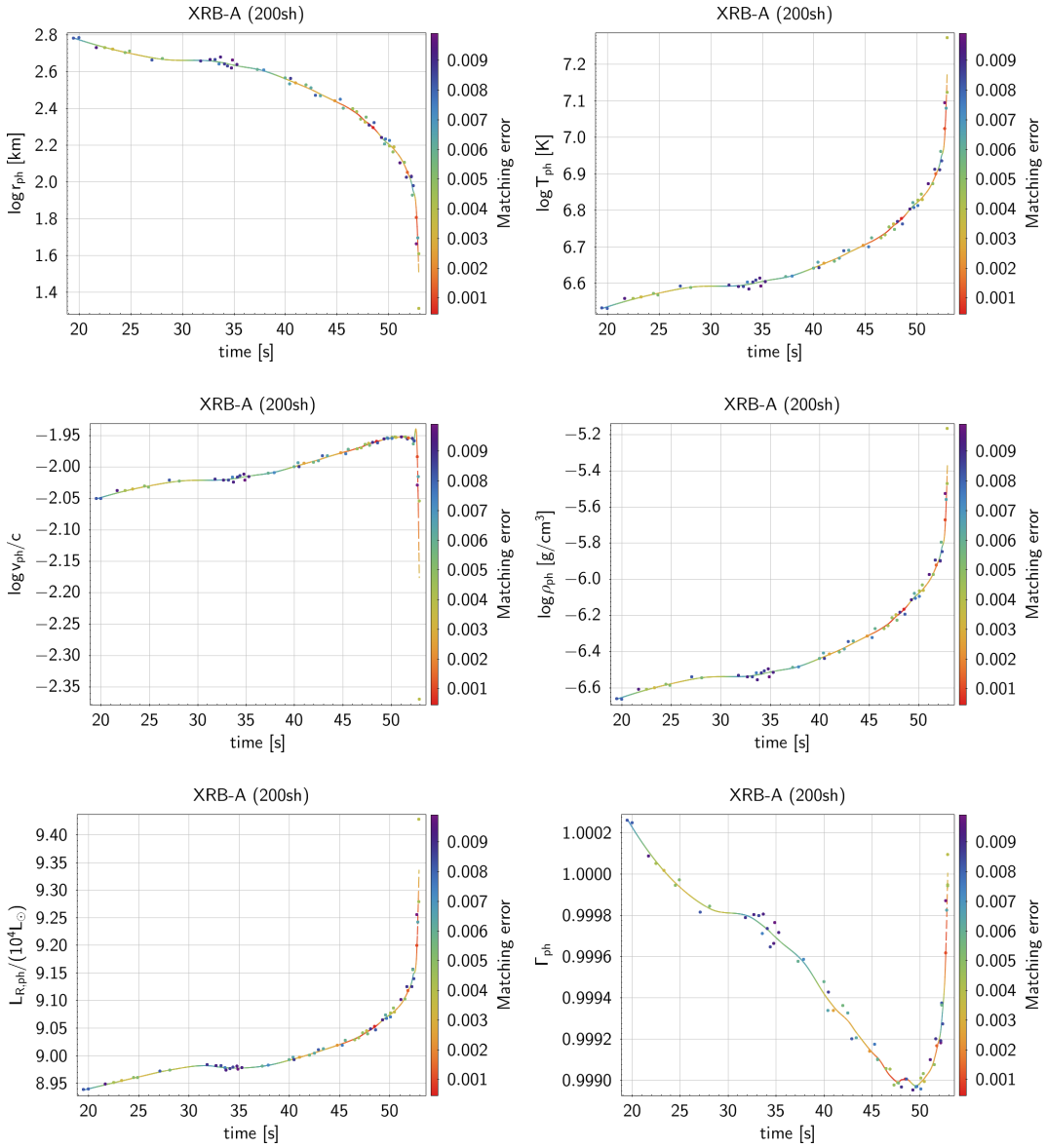

Figure 3.11: Time evolution of photospheric magnitudes, in model XRB-A. In reading order, radius, temperature, wind velocity, density, radiative luminosity and its ratio to local Eddington luminosity. Values corresponding to matching wind profiles are indicated with dots, and predicted values (using smoothing-interpolating technique) with a line. Color scale indicates the matching error obtained (dots) or expected (lines), respectively.

the wind atmosphere is most expanded, and ending in a quick spike ($> 1.6 \times 10^7$ K) that seems to sharply rise up towards the much higher photospheric temperature ($\sim 5 \times 10^8$ K) of the envelope after the wind phase (See Fig. 3.1 panel 3). Wind velocity at the photosphere varies little around $\sim 0.01\,c$ for the most part, and drops abruptly by the end. Density shows an almost identical behavior to temperature.

Photospheric luminosity rises slowly through most of the wind and spikes towards the end, in a similar way to temperature. Furthermore, analysis of the full wind evolution from the lower resolution models shown in App. C.3, shows that this rise may in fact be the recovery part of an overall dip in luminosity around the burst peak expansion. At a first glance, this behavior seems to be at odds with the expected overall sharp rise and slow decline observed in a typical XRB light curve. However, upon a closer look, this change in photospheric luminosity represents quite a small fraction ($\sim 5{-}6\%$) of the average luminosity value while the wind is active ($\sim L_o = 3.52 \times 10^{38}$ erg/s $\sim 9 \times 10^4$ $L_\odot$), and it is a few orders of magnitude smaller when compared to the overall typical burst luminosity rise ($10 - 100$ times the persistent luminosity). Nevertheless, this average photospheric luminosity in the wind profiles is often lower than the peak luminosity reported in the XRB models, remaining very close to the local Eddington value.[7] This drop of luminosity around the peak radial expansion could, in principle, be observed as a flattening of the luminosity peak for the duration of the wind or, if the dip is significant in magnitude with respect to the windless envelope luminosity, as a double peak. The onset of the stellar wind is expanding the envelope further, cooling it down towards the photosphere. This in turn rises opacity and allows for the absorption of more radiative energy into the gas that is transformed into kinetic energy, making the photosphere dimmer. From the observational point of view, such a feature, could be a clear signal of the presence of a stellar wind.

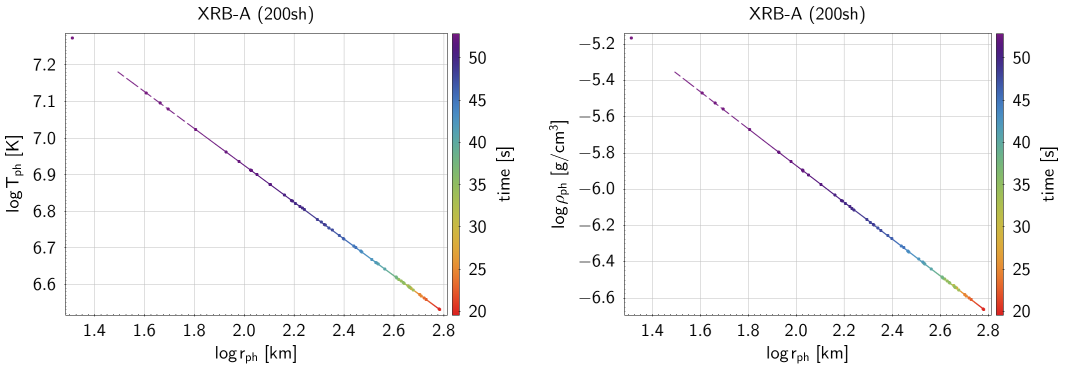

Figure 3.12: Correlated photospheric magnitudes in XRB-A wind profiles. Left panel indicates an approximate $T_{\rm ph}^2 \sim r_{\rm ph}^{-1}$ relation. Right panel similarly implies $\rho_{\rm ph} \sim r_{\rm ph}^{-1}$.

We noted the similarity between photospheric temperature and density time evolution curves, and their apparent inverse relation to photospheric radius. The actual linear correlation can be appreciated in Fig. 3.12. In the characterization study shown in previous chapter (Sect. 2.4.3) we found similar correlations (Eq. 2.23 and 2.24), due to the fact that

[7] Especially in models XRB-1 to 4. Compare peak values in Table 3.1 with photospheric luminosity curves here and in Appendix Section C.3.

Regression Model	a	c	Correlation
$\log T_{\rm ph} = {\rm c} + {\rm a} \log r_{\rm ph}$	-0.503	10.45	0.9999
$\log \rho_{\rm ph} = {\rm c} + {\rm a} \log r_{\rm ph}$	-1.013	1.22	0.9999
$\frac{8}{3}\frac{v_{\rm ph}}{c} = {\rm c} + {\rm a}\frac{\dot{M}}{L_{R,{\rm ph}}}\frac{GM}{r_{\rm ph}}$	0.997	5.5×10^{-5}	0.9999
$\frac{\dot{E}}{L_{R,{\rm ph}}} - 1 = {\rm c} + {\rm a}\frac{\dot{M}}{L_{R,{\rm ph}}}\frac{GM}{r_{\rm ph}}$	0.992	3.6×10^{-4}	0.9994

Table 3.4: Regression results from correlations among observable variables and wind parameters in model XRB-A.

photospheric luminosity was close to Eddington luminosity. Now we are able to confirm that these correlations hold for the more realistic scenario studied here. Equation 2.25 also stated the correlation between observable features, such as photospheric luminosity and wind velocity, and wind parameters determined by physical conditions of the inner parts of the envelope. These correlations were also found in all XRB hydrodynamic models studied. The regression results are shown in Table 3.4. The derivation of these correlations was treated in Section 2.4.3, and their importance was already discussed in Section 2.5.

Finally, and for the sake of completeness, Figures 3.13 and 3.14 show the time evolution of physical magnitudes at the critical point and wind base (XRB model matching point), respectively. The critical point remains much closer to the base, extending only a few times the NS radius, and receding at a somewhat uniform rate. Temperature, velocity and density at the critical point evolve in the opposite direction, slowly growing, with an overall smaller change of velocity around $v_{\rm cr} \sim 10^{-3}c$, but with an abrupt drop right before the end of the wind. Luminosity stays very close below the local Eddington luminosity. The effective optical depth of the critical point stays always higher than the required threshold of 10, needed to consider the wind optically thick, but it seems to drop very quickly by the end of the wind. This may hint that there could be a continuation of the wind with an optically thin regime, which our wind simulation code does not contemplate. However, the XRB-to-wind matching point moves quickly towards the outermost shells of the XRB hydrodynamic model where the boundary condition $P_g = 0$ was set, making the appearance of a thin wind unlikely and, in practice, impossible to search further matches, even if the wind code was capable of dealing with an optically-thin wind.

Physical magnitudes at the wind base (XRB-wind matching points) were discussed in previous Section 3.3.1, but there are a few things we can add. Most notably, the ratio of gas pressure gradient to radiation pressure gradient at the wind base (last panel of Figure 3.14) shows values very close to unity. This result rests in good agreement with the very "generic" boundary condition assumed in Section 2.2.3 and used for the characterization study from Section 2.4. It does not come as a surprise, since the previously assumed boundary condition was inspired by (and is a necessary condition for) a situation in which wind velocity can be neglected and radiation pressure is not dominant, both of which correspond to a transition region between stellar wind and static envelope. These turned to be good approximations to physical conditions in all XRB hydrodynamic models studied, as can be seen for current model XRB-A (Figure 3.14, last three panels): wind velocity is smaller than 1 `cm/s` ($\sim 0.33 \times 10^{-10}c$), and radiative luminosity is about one half of the local Eddington limit needed to accelerate the wind; the remainder half of the driving force is provided by gas pressure

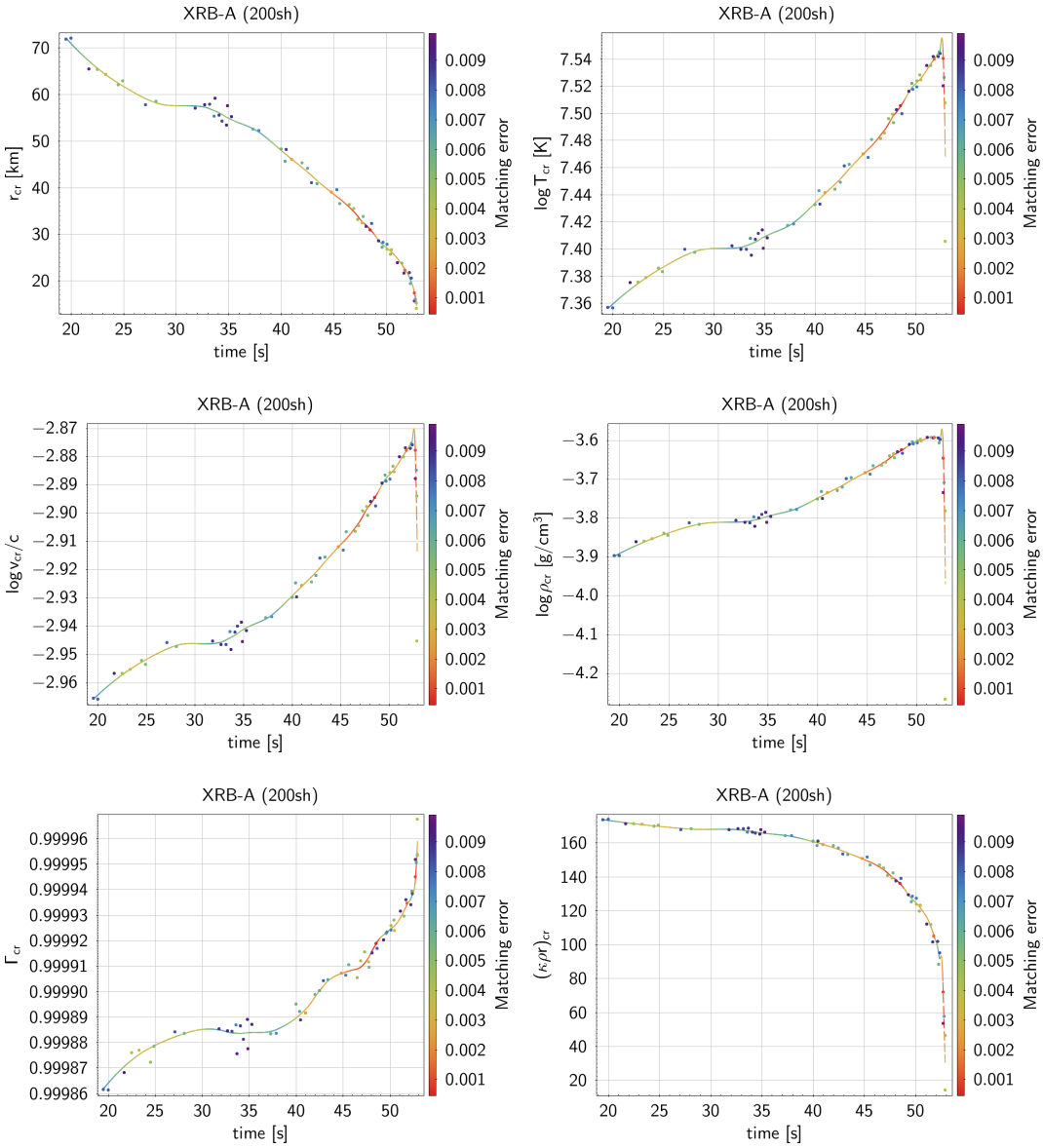

Figure 3.13: Time evolution of physical magnitudes at the critical point, in model XRB-A. In reading order, radius, temperature, density, radiative-to-Eddington luminosity ratio, and effective optical depth. Wind-burst matching points are indicated with dots, and predicted values (using smoothing-interpolating technique) with a line. Color scale indicates the matching error obtained (dots) or expected (lines), respectively.

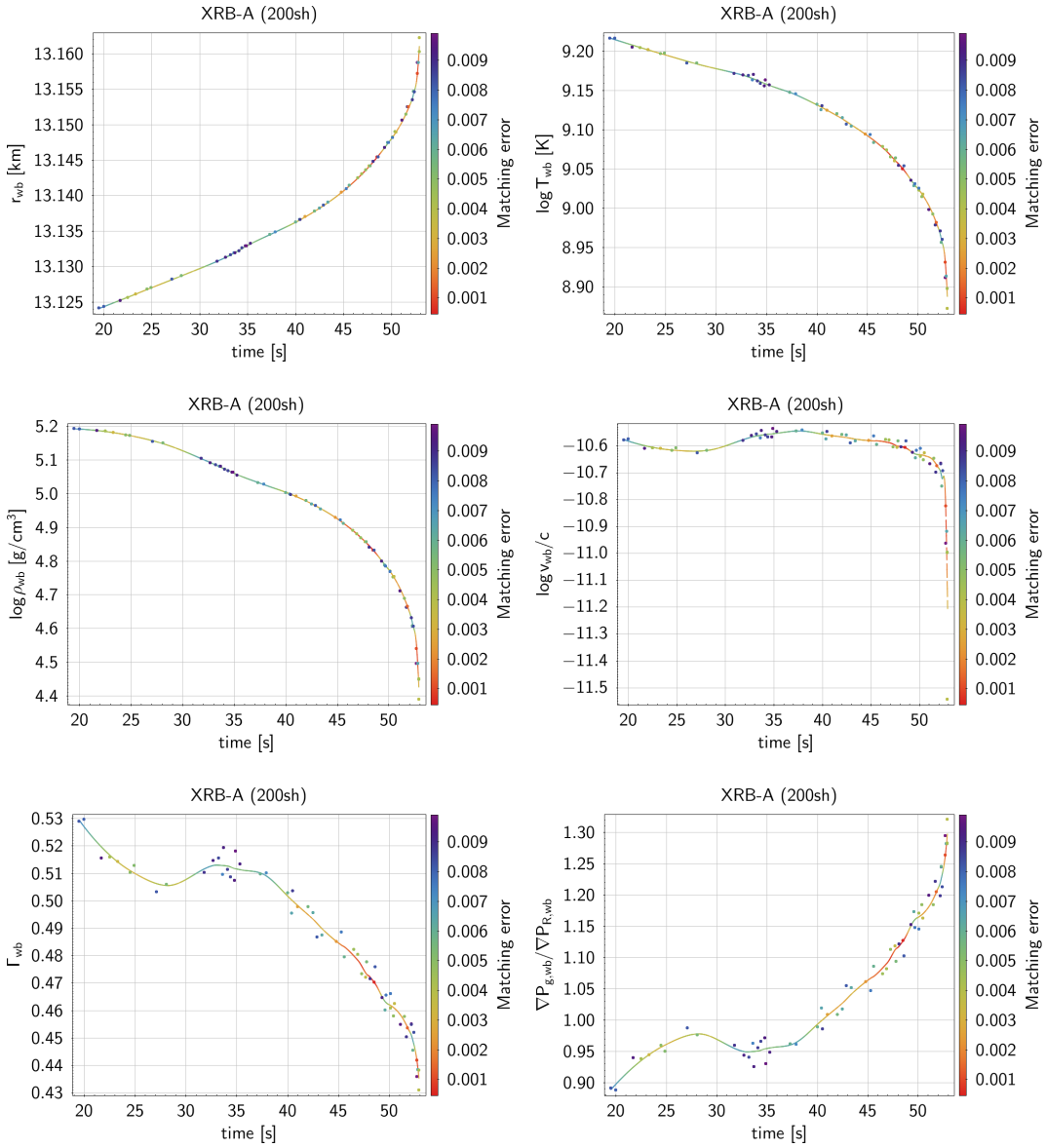

Figure 3.14: Time evolution of physical magnitudes at the wind base, in model XRB-A. In reading order, radius, temperature, density, velocity luminosity ratio Γ, and gas-to-radiation pressure gradient ratio. Wind-burst matching points are indicated with dots, and predicted values (using smoothing-interpolating technique) with a line. Color scale indicates the matching error obtained (dots) or expected (lines), respectively.

gradient, due to the abrupt temperature and density changes.

3.4 Summary

In this chapter, the possibility of stellar winds appearing from a more realistic burst scenario, as described by XRB hydrodynamic models, was studied. In order to do so, a data smoothing technique had to be applied to some of the XRB models results. A series of novel methods and algorithms were then developed for matching the stellar wind model solutions to the physical conditions given by the XRB hydrodynamic simulations.

After finding the matching solution candidates and analyzing their consistency, we concluded that a stellar wind appears for each burst studied here. A quantification of the consequent mass-loss was pursued for every isotope species produced in the XRB model, with particular interest in the light p-nuclei: ^{92,94}Mo and ^{96,98}Ru. For this objective, further post-processing was required to compensate for some irregularity in the distribution of matching points and, in the case of lower resolution XRB models, to extract some useful information from matches with higher error. A crude estimate of the possible contribution of XRBs to the synthesis of light p-nuclei resulted only in a small fraction ($10^{-5} - 10^{-6}$) of their galactic abundances. An unrealistically large number of XRB sources would be required to account for their origin.

Finally, an analysis of the time evolution and correlation of observables and other physical magnitudes was performed. All of the correlations found in the preliminary study in Section 2.4.3, were found to hold. Their significance regarding observational applications was already discussed in Section 2.5.

Chapter 4

Summary and conclusions

The study of stellar winds in the context of XRBs performed in this thesis had two main motivating issues. These are open questions from branches of physics as seemingly unrelated as nucleosynthesis and the study of degenerate matter. The first question is whether or not the heavy elements produced from nucleosynthesis in XRBs can escape NS gravity through the stellar wind and contribute *significantly* to Galactic abundances. The special interest is set on some light p-nuclei that are underproduced in every other astrophysical scenario, with respect to inferred abundances. The second question relates to the determination of the equation of state (EoS) of neutron-degenerate matter. Independent measurements of NS radii and masses are required to constrain available EoS theoretical models. Therefore, predictions of observable features in NS expanded envelopes during stellar winds are important in this regard.

A non-relativistic stellar wind model was successfully implemented in Chapter 2. The model introduced some improvements with respect to previous works in literature, like the inclusion of modern opacity tables from OPAL and The Opacity Project (see Appendix B.2), and treatment of the critical point (Appendix A.2). Its implementation also required the development of novel numerical methods and other useful algorithms (Appendices A.4 and A.5). In Section 2.4, the stellar wind model was applied to a generic NS scenario, as a way to test its implementation, characterize possible solutions and explore the parameter space. In order to simulate this generic scenario, a rather flexible but sensible choice of inner boundary condition at the wind base was imposed (see Section 2.2.3). This restricts the region of compatible solutions in the parameter space $(\dot{M}, \dot{E})$. Even with such a generic choice of inner boundary conditions, the simulations showed some remarkable features and common patterns. The results from these simulations are compatible with other similar studies (Kato 1983; Joss & Melia 1987; Quinn & Paczyński 1985).

The resulting wind profiles were all observed to transition from a gas pressure-driven regime at the inner parts, where opacity is low, into a full radiatively-driven wind in the outer parts. Most notably, some photospheric magnitudes showed a high correlation (see Section 2.4.3), namely $r_{\rm ph} \sim T_{\rm ph}^{-2} \sim \rho_{\rm ph}^{-1}$, independently of the NS radii at which the aforementioned wind base condition was imposed. These correlations are apparently independent from model parameters $(\dot{M}, \dot{E})$ too, so they are expected to appear in every scenario. They seem to derive from the choice of boundary conditions at the photosphere (see Section 2.2.1), and the fact that photospheric luminosity takes on values very close to Eddington luminosity

$L_o = \frac{4\pi cGM}{\kappa_o}$, for every choice of parameters $(\dot{M}, \dot{E})$.

Another set of correlations found involves parameters $(\dot{M}, \dot{E})$ as well as photospheric magnitudes (see Equation 2.25). Since wind parameters are determined upon imposing conditions for all physical variables at the wind base, these correlations effectively link observable magnitudes to the physics of the innermost parts of the envelope, close to its interface with the NS core. This could lead to a technique that allows to indirectly determine the radius of the NS, independently from its mass, from photospheric magnitudes, as outlined in Section 2.5. However, a study in a more realistic XRB scenario was required first, before jumping to this conclusion.

In Chapter 3, we linked the stellar wind model to a series of XRB hydrodynamic models by José *et al.* (2010). There, we developed a technique that successfully matched different wind profiles to the boundary conditions given at different points during the evolution of each burst, with a quasi-stationary approach. This allowed us to construct a time evolution of wind profiles and to quantify the mass-loss of each isotope produced by nucleosynthesis in the XRB. The overall ejected mass varied between the XRBs analyzed, ranging from $\sim 6 \times 10^{19}$ g in the high resolution model XRB-A, studied in Section 3.3, to smaller values in the range of $\sim 2 \times 10^{17} - 7 \times 10^{18}$ g in the lower resolution models shown in Appendix C. The ejected material contained a small fraction of our light p-nuclei of interest. The species with the highest amount across all models was ^{92}Mo, with $\sim 1.5 \times 10^{16}$ g in XRB-A, and within $10^{12} - 10^{13}$ g in the other models. However, an estimation of their significance regarding Galactic abundances showed that an unreasonable number of XRB sources like the one analyzed (corresponding to a typical X-Ray Burst episode) was required to account for the observed abundances of each isotope. Therefore, we concluded that XRB sources are unlikely to constitute the sole explanation of their origin. Nevertheless, given that the models analyzed showed a large difference in the ejected mass of these p-nuclei (three orders of magnitude), we cannot assure that a future study on XRB hydrodynamic models with overall larger metallicity, will not show a more significant contribution.

Upon analyzing the photospheric magnitudes during the wind phase, the correlations previously discussed in Section 2.4.3, were found to hold. This is a promising result regarding the issue of NS radii determination. Nevertheless, further study is required to determine whether these results are affected by the inclusion of more complex input physics, like relativistic wind models, or a more detailed treatment of radiative transfer.

Appendix A

Computational and mathematical techniques

In this Appendix we include descriptions of the most relevant algorithms and techniques employed throughout this work. In some occasions, we could apply commonly used tools in numerical analysis, adapted to the particular problems we encountered. But for some others, novel techniques had to be developed from scratch.

Stellar wind equations described in Section 2.1 require numerical calculations to be solved. The set of differential equations was integrated using an adaptive step Runge-Kutta method described in Section A.1. Two-point boundary-value problems, like the one we have, require techniques like the shooting method (Section A.3). Since the stellar wind equations present a singularity (see Section 2.2.2), a variable substitution was introduced to overcome the problems of numerical calculations related to it, explained in Section A.2. Data smoothing using a local regression technique was required for Chapter 3, and it is described in Section A.6. Novel techniques we developed include robust root-finding algorithms (Section A.4) and a grid search optimization algorithm (Section A.5), that were used in a variety of situations.

A.1 Adaptive step Runge-Kutta method

In general, a set of ordinary differential equations (ODE) of any order can be expressed as a set of N first-order ODEs as:

$$\frac{dy_i(x)}{dx} = f_i(x, y_1, ..., y_N), \qquad \text{with } i = 1, ..., N \tag{A.1}$$

where $y_i(x)$ are unknown functions of the independent variable x, and f_i are known functions expressed in terms of them. In addition a set of boundary conditions have to be provided to uniquely determine all integration constants. These can be given all at one point, x_o, in which case we have an *initial value problem*, or at more than one point, which is called *two-point boundary-value problem*. Several iterative methods exist for solving initial value problems numerically. They usually consist in advancing the solution from x_o, where function values $y_i(x_o)$ satisfy the boundary conditions, taking discrete small steps of size h towards the desired stopping point. Each step accumulates error, which in the simplest case (Euler's method) is of order h^2.

The Runge-Kutta methods reduce the error in each step by taking one or several intermediate steps. Each extra intermediate step can reduce the error of the full step by one order, when combined with the right weight coefficients. For instance, when advancing the integration of one equation ($N = 1$) from step n to $n+1$, a fifth-order Runge-Kutta method (RK5) formula takes the form:

$$\begin{aligned} k_1 &= hf(x_n, y_n) \\ k_2 &= hf(x_n + a_2 h, y_n + b_{21} k_1) \\ &\vdots \\ k_6 &= hf(x_n + a_6 h, y_n + b_{61} k_1 \cdots + b_{65} k_5) \\ y_{n+1} &= y_n + c_1 k_1 \cdots + c_6 k_6 + O(h^6) \end{aligned} \tag{A.2}$$

where $\{k_i\}$ are approximated increments of $y(x)$ at each intermediate step, and the coefficients $\{a_i, b_{ij}, c_i\}$ are different weights that vary across members of the Runge-Kutta family (see Press *et al.* 1992) and references therein.

Additionally, the step size h can be adjusted dynamically at each step: reducing it to meet an accuracy requirement where error is large, or increasing it where error is small to save computing time. The method developed by Cash & Karp (1990), based on the original idea by Fehlberg (1970), combines a Runge-Kutta method of order 5 (Equation A.2) with a different choice of the same amount of intermediate steps that results in a formula of order 4:

$$y^*_{n+1} = y_n + c^*_1 k_1 \cdots + c^*_6 k_6 + O(h^5). \tag{A.3}$$

This mixed fourth and fifth orders Runge-Kutta method (RK45) allows us to obtain the following estimate of the fourth order truncation error:

$$\Delta = y_{n+1} - y^*_{n+1} = \sum_{i=1}^{6} (c_i - c^*_i)\ k_i(h) \sim O(h^5) \tag{A.4}$$

This way, the step size h can be adjusted to meet a certain value of Δ. When trying a step with size h_1, if the error obtained Δ_1 is larger than the desired Δ_o, the step can be retried with a smaller step estimate:

$$h_o = h_1 \left| \frac{\Delta_o}{\Delta_1} \right|^{1/5}. \tag{A.5}$$

The same can be applied in reverse if the error obtained is much smaller than the required one, to allow a larger next step try.

The adaptive size Runge-Kutta method outlined here (RK45) was adopted to integrate the wind model equations (2.9 and 2.10). A suite of FORTRAN procedures, provided in Press *et al.* (1996), was implemented for this task. Some necessary modifications were in order, though, to accommodate for some of the special features of our problem.

A.2 Critical point substitution

In order to avoid the numerical difficulties involved in calculating the velocity gradient at the critical point we used a substitution. The velocity gradient in the wind equations is

expressed in the form of a ratio:

$$\frac{r}{v}\frac{dv}{dr} = \frac{N(r,T,v)}{D(T,v)} \tag{A.6}$$

with N, D being the numerator and denominator which should both become zero at the critical point in order to have a regular solution. Explicitly, the singularity condition is given by $D(T,v) = v^2 - \frac{kT}{\mu m_A} = 0$. Hereafter, the local isothermal sound speed will be denoted by s, where $s^2 = \frac{kT}{\mu m_A}$.

Consider the following function and its derivative:

$$y_{(x)} = \frac{1}{2}\left(x + \frac{1}{x}\right) = \frac{x^2+1}{2x} \tag{A.7}$$

$$y'_{(x)} = \frac{1}{2}\left(1 - \frac{1}{x^2}\right) = \frac{x^2-1}{2x^2} \tag{A.8}$$

In differential form we get:

$$\frac{dy}{y} = \frac{y'}{y}dx = \frac{x^2-1}{x^2+1}\frac{dx}{x}$$

If we now set $x^2 = \frac{v^2}{s^2}$, then $\frac{dx}{x} = \frac{dv}{v} - \frac{1}{2}\frac{dT}{T}$ and it can be easily found that:

$$\frac{dy}{y} = \frac{\frac{v^2}{s^2}-1}{\frac{v^2}{s^2}+1}\frac{dx}{x} = \frac{D_{(T,v)}}{v^2+s^2}\left(\frac{dv}{v} - \frac{1}{2}\frac{dT}{T}\right)$$

The radial gradient of this new variable y then satisfies:

$$\frac{r}{y}\frac{dy}{dr} = \frac{D_{(T,v)}}{v^2+s^2}\left(\frac{r}{v}\frac{dv}{dr} - \frac{1}{2}\frac{r}{T}\frac{dT}{dr}\right) \tag{A.9}$$

and replacing expression A.6 for the velocity gradient, the denominator D is canceled, giving:

$$\frac{r}{y}\frac{dy}{dr} = \frac{1}{v^2+s^2}\left(N_{(r,T,v)} - \frac{D_{(T,v)}}{2}\frac{r}{T}\frac{dT}{dr}\right)$$

This derivative does not present a singularity anymore and can be integrated instead of the momentum equation for the new variable y.

There is one inconvenient, though, when transforming back to v. The function $y(x)$ has one global minimum at $x = 1$ with $y_{min} = 1$, which corresponds to the critical point (where $v = s$). From there, y increases monotonically towards both $x = 0$ and $x \longrightarrow \infty$ (see Fig. A.1). Its inverse function therefore has two branches:

$$x_\pm = y \pm \sqrt{y^2 - 1} \tag{A.10}$$

with the following properties for all y:

$$x_+ \geq 1 \qquad x_- \leq 1 \qquad x_- x_+ = 1 \qquad x_+ + x_- = 2y$$

Care must be taken about which of the branches is followed. It is not known a priori if at a certain point the wind should be supersonic (x_+) or subsonic (x_-), unless integration is started from the critical sonic point in a particular direction. When integrating away from it, the value of y must increase, so it must be ensured that the radial gradient takes a positive value for $r \gtrsim r_{cr}$ and negative value for $r \lesssim r_{cr}$ and prevent any numerical error near the critical point that may give a different result.

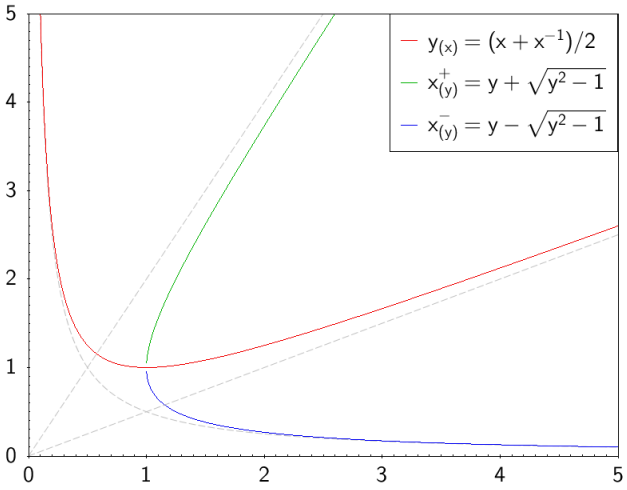

Figure A.1: Variable substitution for critical point. Change of variables $y(x)$, in red, used to integrate close to the critical point $(x, y) = (1, 1)$, and the two branches of its inverse function (green and blue).

A.3 Shooting method

In a two-point boundary problem, the boundary conditions are given at more than one point.[1] When starting numerical integration with iterative algorithms like RK-45 from one of these points, we will have insufficient boundary conditions to uniquely determine every variable starting value. This gives multiple possible solutions, most of which will not satisfy the rest of boundary conditions at the end point (see Figure A.2). The *shooting method* is usually employed to find a solution that does. The basic idea behind it resembles any game of projectile shooting, like bow and arrow, perfecting our aim to hit a target. It consists in trying several solution candidates (the shots), temporarily guessing a set of values that complies with boundary conditions at the starting point. The deficit in starting boundary conditions gives us a number of free variables to choose (aiming parameters), equal to the number of remaining boundary conditions at the end point. When integration arrives at the end point, the values obtained for all variables are tested against the rest of boundary conditions (the target). These end point values we obtain depend on the starting aiming parameters and will often fail to satisfy the boundary conditions at the end point (miss the target) in the first few guesses. The objective (hit the target, of course) is to find the starting aiming parameters that give solutions satisfying the boundary conditions at the end point. We can construct a function that measures how far off from target our shot landed (target function), which will depend on our aiming parameters, and then employ a suitable root finding method to find zeros of that target function (see next Section A.4).

In the stellar wind model we have a system of two ODEs (momentum conservation equation 2.9 and radiative diffusion equation 2.10), for which we need two integration constants. A total of four boundary conditions are given at the critical point and the photosphere; but their

[1] In our case we have two boundaries, critical point and photosphere. But, in general, conditions can be given at more than two points (see Press *et al.* 1992).

location is not given explicitly, adding two extra undetermined parameters.[2] This results in four total parameters, $\{T_{\rm cr}, r_{\rm cr}, T_{\rm ph}, r_{\rm ph}\}$, with two boundary conditions at each point (see sections 2.2.1 and 2.2.2). At first sight, this looks like a two-dimensional root-finding problem for which we would need to find roots of a vector target function $\vec{f} = (f_1(T_{\rm cr}, r_{\rm cr}); f_2(T_{\rm cr}, r_{\rm cr}))$, with f_1 and f_2 being scalar target functions associated to each of the photospheric boundary conditions. Multidimensional root-finding algorithms suggested in literature involve calculation of derivatives, like Newton-Raphson. They are inadequate in this case for reasons exposed in Appendix Section A.4, and we would like to avoid them. For one-dimensional problems, the alternatives are bracketing methods, but no generalization to more dimensions exists, that we know of.

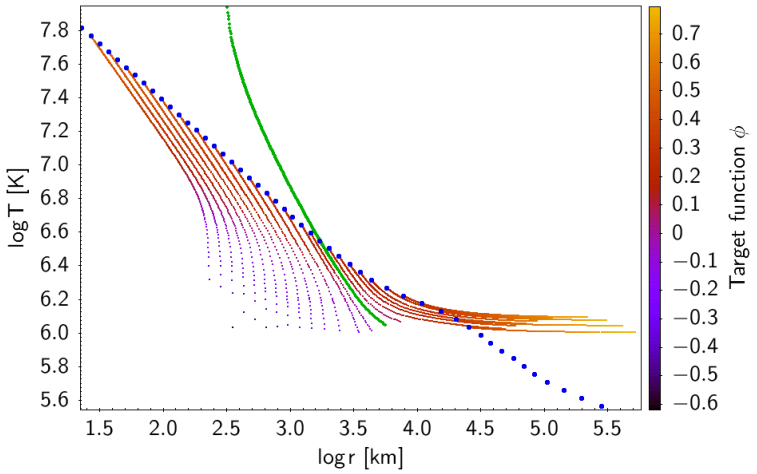

Figure A.2: Two-point boundary problem with the stellar wind model. Different solution candidates (dotted lines in color scale) are obtained when integrating outwards from critical points (blue circles) with varying $T_{\rm cr}$, while disregarding photospheric boundary conditions (resulting in *missed shots*). Color scale represents the value of the target function employed with the shooting method. The actual solution found with the shooting method (plotted in green), satisfying all boundary conditions, is also integrated inwards into its subsonic region.

However, with deeper analysis, the problem can be turned into a one-dimensional shooting. Since two of the four parameters are related to the positions of the boundaries, $\{r_{\rm cr}, r_{\rm ph}\}$, they are only necessary to determine the integration starting and stopping points. Starting at the critical point, we have two equations (singularity condition 2.17 and regularity condition 2.18) to determine the three initial values needed to start integration $\{r_{\rm cr}, T_{\rm cr}, v_{\rm cr}\}$. That leaves us with only one free choice, for instance $T_{\rm cr}$, to work as aiming parameter. As the integration advances, we can decide to stop it whenever either one of the photospheric conditions is met (we chose the optical condition 2.14), which decides $r_{\rm ph}$.[3] We are left with the one remaining photospheric condition (temperature condition 2.13) to construct our now

[2] This is like shooting arrows to a moving target while riding a horse, which is extremely difficult. Unless, of course, you are... the Mongols.

[3] In some cases, this condition was never met and the integrations were set to stop at a certain high radius or maximum allowed steps. In Figure A.2, this was the case of profiles extending towards high radii, settling at approximately constant T values, which gave high target function values.

scalar target function, and proceed with the one-dimensional shooting as it was outlined in Section 2.3. The application of a bracketing method is now possible, with some safeguards (see Section A.4).

A.4 Root finding algorithms

In various occasions throughout this work, a root-finding algorithm with special requirements was needed. The shooting method described in Section A.3, and the XRB-wind matching method in Section 3.2 are the most relevant of such occasions. The two main special features in these cases are: first, the functions that need to be zeroed are somewhat expensive to evaluate in terms of computational time (one or several integrations of an ODE problem in each evaluation); and second, but more important, the function domain depends on several varying parameters in a way we do not know a priori.[4]

Conventional and fast-converging methods like Newton-Raphson, which depend on the derivative of the function, present some issues that render their application inviable for the cases at hand. The first of these issues is the very need for calculating the derivative of the function. Since we lack analytical expressions of our functions, a numerical approximation of the derivative must be calculated instead. This requires additional evaluations of the function at nearby points, which multiply the already considerable computation time of each step. In some cases, this extra time may be compensated by the faster convergence of these methods, which require fewer steps. However, computational speed is not the only concern with methods that involve derivatives.[5] A more important matter is their possibility of failing to converge in certain cases. Stationary points, cyclic iteration points, *overshooting*, and discontinuous derivatives are some of the common pathological cases. Other related methods deal with some of these issues with different techniques, but they are hardly foolproof, and our functions sometimes may present several of the aforementioned pathologies.

Bracketing methods, on the other hand, suffer from fewer issues. Among them, the bisection method, while being among the slowest, is the simplest and most robust. The only requisite is that we need to provide a starting interval where our function is continuous and changes sign. This still presents the problem of the unknown valid domain where to choose the starting interval. However, this issue is less problematic now since, once inside the valid domain, bracketing methods will not overshoot outside of it like derivative-based ones may (see the case of x_5 in Figure A.3). In order to overcome this problem the following technique was developed.

A.4.1 Increasing Resolution Interval Search

For a given function $y(x)$, we usually want to find a value x_o, such that $y(x_o) = y_o$, for a given target value y_o. That is, we need to find roots for the function:

$$f(x) = y(x) - y_o \tag{A.11}$$

[4] In the shooting method used for solving the stellar wind equations (see Section 2.3, and Appendix Section A.3), the range of candidate $T_{\rm cr}$, for which physically valid ODE solutions are found, changes with model parameters $(\dot{M}, \dot{E})$. Similarly, in the XRB-wind matching method (Section 3.2), the first matching variable $\dot{M}$, has a range of acceptable solutions that depends on $\dot{E}$ and abundances X_i.

[5] Quasi-Newton methods and other modifications can be used when derivatives are unavailable or expensive to calculate. However they still give some approximation of derivative, suffering from the same ailments.

We search for an interval $[x_a, x_b]$ where our target function $f(x)$ is: well defined, continuous, and changes sign (i.e., $f(x_a)f(x_b) < 0$), so that we can safely apply bisection (or other bracketing method of choice). Suggested methods in literature (see Press *et al.* 1992) involve partitioning a given big interval $[x_0, x_N]$ into an arbitrary amount of smaller intervals, N, by evaluating the target function at a sequence of intermediate points, $\{x_i;\ i = 1, ..., N-1\}$, and then checking which consecutive pair of points $[x_i, x_{i+1}]$ gives the desired sign change in $f(x)$. There are three problems with this scheme. We will describe them and explain the solution we implemented, with an illustrative example in Figure A.3.

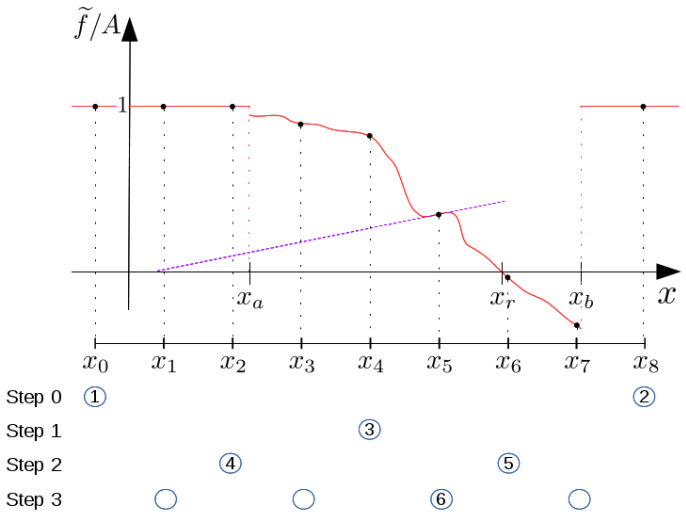

Figure A.3: IRIS method illustration. Modified target function $\widetilde{f}$, normalized to magic number A, is plotted in red. Interval $[x_a, x_b]$ marks the valid domain of the original target function f, with the desired root x_r inside. Purple line is the tangent to $\widetilde{f}$ at x_5, illustrating a point where derivative-based methods would overshoot outside the valid domain and fail to converge (so would they at x_3 and x_4). IRIS candidate points for function evaluation $\{x_i\}_{i=0,...,8}$ are also shown, with their evaluation order (numbered circles) at each step of the algorithm displayed below. Empty circles mark evaluations skipped due to additional time-saving criteria (see text).

Problem 1: valid domain. We may be surely evaluating the target function several times outside its valid domain. For this, it is customary to redefine the target function by assigning a *magic number* whenever this happens. In order to avoid choosing a magic number that could naturally occur in the target function, we use an alternative target function in the form:

$$\widetilde{f}(x) = \begin{cases} A \tanh\left[k\ f(x)\right] & x \in \texttt{Dom}(f) \\ \pm A & x \notin \texttt{Dom}(f) \end{cases} \tag{A.12}$$

with arbitrary constants A, k. This new function $\widetilde{f}$ shares the same roots as the original f and behaves similarly in their vicinity, preserving sign change. Additionally, $|\widetilde{f}(x)| < A$

inside $\texttt{Dom}(f)$ and approaches $\pm A$ asymptotically for large $|f(x)|$. This allows us to chose any value of A (for instance $A = 1$) as a magic number. The value of k, determines the slope of $\widetilde{f}$ close to the root, and can be adjusted freely to regulate the sensitivity of the method (since $\Delta\widetilde{f} \sim Ak\Delta f$ close to the roots). For instance, if we set $k = 1/2$, with $f(x) = y(x) - y_o$; $y(x) = \ln T(x)$; and $y_o = \ln T_{\text{eff}}$; it can be easily found that:[6]

$$\widetilde{f} = \frac{T(x) - T_{\text{eff}}}{T(x) + T_{\text{eff}}} \tag{A.13}$$

inside the valid domain, which corresponds to the target function ϕ employed with the shooting method (see Section 2.3), where T depends on the shooting parameter $x = T_{\text{cr}}$. In Equation A.12, the "$\pm$" sign outside $\texttt{Dom}(f)$ can be manually chosen to match the sign of f at the nearest valid point, if we know it. If we do not, we can choose "+" both above and below $\texttt{Dom}(f)$ and an artificial discontinuity will appear at the border of $\texttt{Dom}(f)$ where $f(x) < 0$ (the case of x_b in Figure A.3). Which leads us to Problem 2.

Problem 2: continuity. This is a requisite that cannot be guaranteed a priori. Whether the discontinuity arises artificially (for instance, from the solution to the previous problem) or it is naturally occurring in our target function, and we are unlucky enough for the discontinuous jump to change sign in $f(x)$, the bisection method will then be fooled into converging on it. We are left with few options, none of them certain, except checking a posteriori if the bisection resulted in a *root false positive*. But, in the case of the artificial false root, there is a workaround related to the solution of Problem 3.

Problem 3: computing time. We do not know how many intermediate points will suffice to find the desired interval, and we would prefer not to evaluate the already expensive target function unnecessarily, to avoid the extra computing time. In this regard, the technique developed here presents a substantial improvement. Instead of dividing the original interval into many small pieces and evaluating the target function in all and every intermediate point upfront, we proceed progressively (see evaluation order in Figure A.3). Starting with the original interval ($[x_0, x_8]$ in the example), we evaluate at both extremes (step 0) and in the middle-point (x_4) (step 1). If either of the two resulting sub-intervals is suitable for bisection, we proceed with it. If none is, we iterate recursively, halving each new sub-interval and evaluating at the new middle-points, while book-keeping the values of $\widetilde{f}(x_i)$ at each previously evaluated point for subsequent iteration steps, until any of them results in a successful bisection. Each iteration step doubles the resolution, and we can stop the process at a desired maximum allowed resolution (= 8 in the example). That is, taking n steps, would imply 2^n target function evaluations (plus the 2 at the extremes of the initial interval). At first sight, reaching this maximum resolution may involve evaluating the target function at as many intermediate points as the originally suggested method. But more often than not, a bisection-suitable interval is found much earlier. In Figure A.3 this happens in step 2, with the fifth evaluation at x_6. We will rarely be that lucky, so a fourth step is shown to illustrate the following additional time-saving criteria that we added in each interval assessment to avoid further unnecessary evaluations in subsequent iteration steps:

[6] Here we used the identity $\tanh(z) = \dfrac{e^{2z} - 1}{e^{2z} + 1}$.

- After a minimum *safe* resolution is achieved, intervals with *magic numbers* at both extremes are likely to be outside $\texttt{Dom}(f)$ and can be skipped. This is the case of $[x_0, x_2]$, which prevented evaluation at x_1. We introduce this minimum resolution to avoid falling for $[x_0, x_8]$, for instance, and other cases where the valid domain $[x_a, x_b]$ could be much smaller than the starting interval.
- This is also useful to avoid an interval containing the artificial discontinuity (x_b), which is characterized by having only one extreme with magic number A, and a different value with opposite sign on the other, at the risk of missing out on additional true roots that lie very close to this border of $\texttt{Dom}(f)$. In the example, such an interval is $[x_6, x_8]$, thus avoiding x_7.
- The same can be applied for intervals, that may lie entirely or partially inside $\texttt{Dom}(f)$, for which we sensibly suspect they are far away from the root, giving similar high values at both extremes (e.g. $\widetilde{f}(x_i) \simeq \widetilde{f}(x_{i+1}) \gtrsim 0.8A$ or $\lesssim -0.8A$). This happens with $[x_2, x_4]$ allowing us to skip x_3.

This method, dubbed *IRIS* (an acronym of this subsection's title), was successfully applied in our simulations, both for finding wind profiles with the shooting method, and for later matching them with XRB models. The illustrative example in Figure A.3, though hand-drawn, synthesizes the essence of the situations encountered while applying the method in Section A.3 and Section 3.2. In most cases, a root was quickly found after few iterations, reaching low resolutions of 4 or 8 intervals (2 or 3 iteration steps, 8 or fewer function evaluations), and saving a lot of computing time. In a few cases, more were needed, requiring resolutions of 256 or 512 to find a root (8 or 9 steps, and up to 512 evaluations). If we had chosen a fixed amount of subintervals, as the originally suggested method requires, for instance 100 intervals, it would have taken much longer to find a root due to the extra unnecessary upfront evaluations when compared to our quick findings at low resolution ($100/2^{2-3}$ times longer). On the other hand, we also would have missed the roots for the cases that required a higher resolution. The only case in which *IRIS* would not introduce an improvement in speed, is when there is no actual root in the interval; and even then it may still save us from reaching maximum resolution through one of the interval skipping criteria, once the minimum resolution is achieved. Developing such a robust algorithm that could overcome the aforementioned problems and adapt to this variety of situations, while at the same time optimizing computing efforts, was a key element in the present work.

A.4.2 *Simplisection*: a multidimensional bisection?

In Section 3.2, we found yet another situation in which we needed a special root-finding method, but this time for an apparently unavoidably two-dimensional problem. Multidimensional root finding methods commonly found in literature are all derivative-based, or rely on calculating some numerical approximation of derivatives. This makes them suffer from the same inadequacies, previously explained throughout this section, when trying to apply them to our particular problem at hand (especially *overshooting*). To our knowledge, no practical generalization of bracketing methods exist for multidimensional root-finding problems. In an ambitious move, we attempted to develop such a method, ending in a bitter-sweet outcome.

Inspired by our slow but trusty work-horse, *bisection*, we tried to formulate an algorithm that catches its spirit and expands it to higher dimensions. At each step, bisection takes a segment $[a_n, b_n]$, divides it in two, evaluating our function at the middle-point $\frac{a_n+b_n}{2}$, and

checks which half contains the root by looking for opposing signs in function values at each end of a particular interval. So, we need a generalization of segments to more dimensions, a way to divide them into smaller similar elements, and a way to decide if and where the root lies within one of these partition sub-elements, hopefully with only a few function evaluations per step.

The generalization of a segment to more dimensions is the *simplex*, the simplest polytope in an n-dimensional space.[7] Therefore, we name our method *Simplisection* (dubbed *SiSec*, for short). In two dimensions, a simplex is a triangle; in three, a tetrahedron, and so on. In N dimensions, a simplex is the region inside the convex hull determined by $N + 1$ affinely independent vertices.[8] We will postpone the generalization to larger dimensions for a future study and consider first the two-dimensional case we need, that means: triangles.

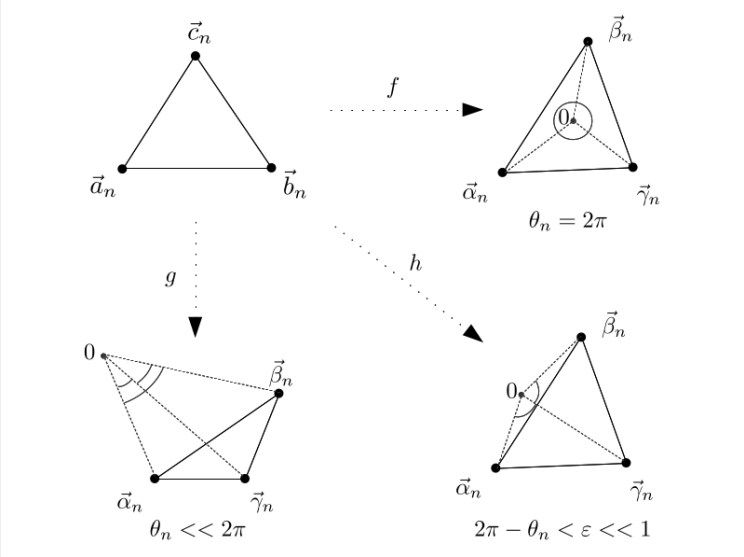

Figure A.4: Simplisection illustration of root location cases.

Let n be any step in our iterative algorithm. In general, unless we are quite unlucky, applying a function $f : \mathbb{R}^2 \to \mathbb{R}^2$ to the three vertices of a triangle, denoted by vectors $\{\vec{a}_n, \vec{b}_n, \vec{c}_n\}$, will also result in three points, $\{\vec{\alpha}_n, \vec{\beta}_n, \vec{\gamma}_n\}$ respectively, that determine a different triangle in the arrival space. Here we need to remark that this new triangle in the arrival space *is not* the image through f of the original triangle. Vertices aside, a non-linear function[9] will deform the straight sides of the original triangle into curve segments. The extent to which the new triangle and the actual image differ will depend on how far from linear our function is. That is, the smaller the second and higher order terms in its series expansion are, the better this triangle approximates the actual image. Unless the root coincides with any extremum,[10] terms higher than linear order usually become smaller the closer we are to the root.

[7] A polytope is the generalization to any number of dimensions of the three-dimensional polyhedron.
[8] Meaning that no lower dimension sub-space can contain all vertices at once.
[9] Like the one we are dealing with surely is. Otherwise roots are easily found by diagonalizing a matrix.
[10] Here the relevant terms are second order. Bisection would also a fail in this situation.

We would like to determine if the zero in the arrival space lies within this triangle, rising our chances that the root lies inside the original triangle as well. If so, we would further subdivide it in following steps, and iterate. One way to do this is by calculating the sum of all angles between vector pairs among $\{\vec{\alpha}_n, \vec{\beta}_n, \vec{\gamma}_n\}$ (see Figure A.4). That is, we want:

$$\theta_n = \arccos(\hat{\alpha}_n \cdot \hat{\beta}_n) + \arccos(\hat{\beta}_n \cdot \hat{\gamma}_n) + \arccos(\hat{\gamma}_n \cdot \hat{\alpha}_n) \tag{A.14}$$

where the *hat* denotes normalized vectors (e.g. $\hat{\alpha}_n = ||\alpha_n||^{-1}\vec{\alpha}_n$). We will distinguish three possible cases, illustrated in Figure A.4 by evaluating three different functions, $\{f, g, h\}$. If $\theta_n = 2\pi$, then the zero lies within the arrival triangle (f case), and the chances are high that the root also belongs inside the original one. We will keep this original triangle. If $\theta_n \ll 2\pi$, then it lies far outside (g case), and our chances are slim. We would surely discard this triangle. But we should not rush to discard it in a case like h, where it lies in the vicinity, giving a $\theta_n \lesssim 2\pi$. In this case the zero may still lie inside the actual image of the original triangle. We can specify a small threshold difference ε for cases like these such that, if $2\pi - \theta_n < \varepsilon$, we allow it to survive for further analysis in following steps. It is clear now that the question of a given triangle containing a root is not one with a binary answer, but a fuzzy matter that depends on θ_n. The decision to further divide and analyze one of them, discard it completely, or maybe save it for a later low priority search, can be made accordingly, by adapting the ε parameter to each case.

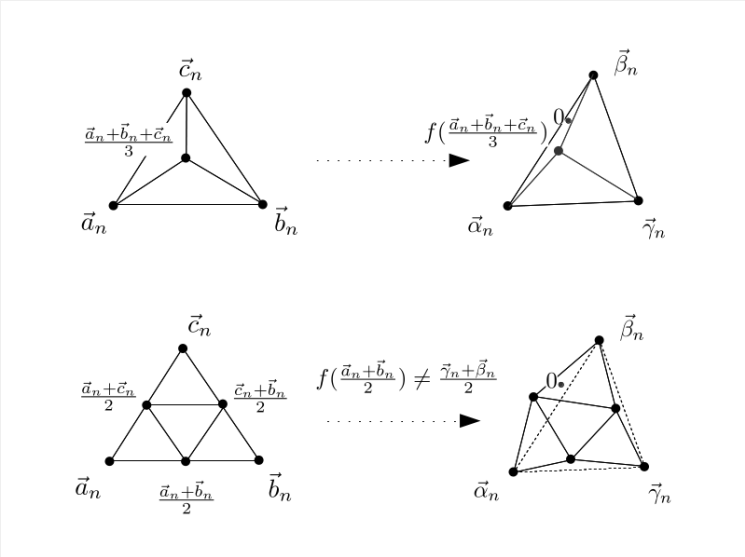

Figure A.5: Simplisection partition and function evaluation possibilities for advancing steps.

We now need to specify a way to partition a *good* triangle into new smaller triangles to be assessed in step $n+1$. We would like to make as few evaluations as possible too. The cheapest option is to evaluate one new point at each step. Following bisection spirit, we could choose the geometric middle point $\frac{\vec{a}_n+\vec{b}_n+\vec{c}_n}{3}$. This divides the original triangle into three new triangles (a *tri-section*), a third of the area each. With f being non-linear, the image of this geometric middle-point will surely not correspond to its counterpart in the arrival space

triangle, i.e. $f\left(\frac{\vec{a}_n+\vec{b}_n+\vec{c}_n}{3}\right) \neq \frac{\vec{\alpha}_n+\vec{\beta}_n+\vec{\gamma}_n}{3}$, but it will have good chances of being somewhere inside of it (see Figure A.5 top case). The problem with this choice is that, if the root lies close to one of the edges, in subsequent partitions like this, this edge's vertices could remain unchanged, resulting in increasingly thiner triangles. Fearing this could present convergence problems, this option was not explored further.

The second partition possibility explored is to bisect each triangle edge, requiring three new function evaluations at each step. Now the original triangle is divided in four smaller triangles (a *tetra-section*), all equivalent in shape to the original one (bottom case of Figure A.5). Again, the images of these three new points will not correspond to the edge mid-points in the arrival triangle, e.g. $f(\frac{\vec{a}_n+\vec{b}_n}{2}) \neq \frac{\vec{\gamma}_n+\vec{\beta}_n}{2}$, and so on. However, since they may lie outside, they can catch an outlying zero close to the edge. The algorithm would then proceed at each step as follows:

1. Evaluate the function at vertices $\{\vec{a}_n, \vec{b}_n, \vec{c}_n\}$, obtaining the image values, $\{\vec{\alpha}_n, \vec{\beta}_n, \vec{\gamma}_n\}$
2. Check if any of the vertices corresponds to a root, e.g. $||\vec{\alpha}_n|| < \delta$, for a given tolerance δ. If so, we can stop now, or continue to search for more roots.
3. Check the resulting points angle sum θ_n (Equation A.14) and decide: If $2\pi - \theta_n < \varepsilon$, then divide into sub-triangles (tetra-section or other choice) and add them to a waiting list for analysis in subsequent steps. Otherwise, discard it. We can also discard triangles for which a maximum precision has been achieved (vertices too close), without finding a root (this safety measure would certainly fail for long thin triangles resulting from *tri-section*).
4. Load the next triangle in the list, and iterate until either no triangles remain in the list, or a maximum number of steps has been reached.

This algorithm was tested with several trial functions giving promising results, converging on multiple roots, even for classic examples of functions and starting positions for which derivative-based method would clearly fail. However, when applied to the original problem it was intended for, the XRB-wind profile match (Section 3.2), time costs made it impractical for a full scale exploration of an entire XRB model data set. This is the main reason it was set aside in favor of the method explained in Section 3.2, combining *IRIS* with *Battleship*.

Aside of the intrinsic cost of calculating a single wind profile, the overall large time cost may have had another contributing factor: the extra cost of evaluating the functions three times in each step (for *tetra-section*). A step is reducing the area to 1/4 of the original, at best. Since area scales as the square of the distance between vertices, that means distances are only halved, so we get to only double the precision at each step. The precision gain per function evaluation is only a factor 2/3. By comparison, bisection has a precision gain per function evaluation of 2. If *tri-section* could be worked out, with 1/3 area and one point per step, it would mean a gain per evaluation of $\sqrt{3} \simeq 1.73$. Better, but not certain it is feasible. A hybrid option could be tried, evaluating at only one of the *tetra-section* edge mid-points per step, dividing the original triangle in two, halving the area, and obtaining a $\sqrt{2} \simeq 1.41$ gain ratio.

Although the *Simplisection* implementation explained here was impractical for the rather complicated case at hand, it still proved useful for test cases where other methods would certainly fail. An interesting possibility is its potential generalization to n-dimensions. Further study is needed to achieve this, and explore possible improvements.

A.5 Grid search optimization: a game of *Battleship*

Many times across the present work, we needed to explore a parameter space (or a given data set), usually in the form of a two-dimensional grid, in search for a region in that space (or a subset of data points) for which a certain set of desired conditions is met. The extent and shape of that desired region was a priori unknown and changed in relation to other varying parameters (or between datasets). Each point in the grid required time-consuming calculations to determine its compliance with the desired conditions. Quite often, the most expensive points to evaluate were the ones that did not meet the required conditions, lying outside the desired region, and making their calculation a fool's errand.

In order to avoid exploring the entire grid blindly, wasting computing efforts, we implemented an algorithm inspired by the board game *Battleship*. In the game, each player tries to sink a fleet of warships, laid by the opponent in an unknown distribution over a grid. The player guesses grid points to shoot at, to which the opponent must truthfully answer "*hit*" or "*miss*". Since most of the ships span across several contiguous grid points, once a player hits one of such points, a sensible strategy is to subsequently shoot at the adjacent points, trying to quickly sink one entire ship, rather than to keep shooting randomly. This is the key point of the algorithm we implemented: once we found a favorable grid point (a hit), we continue the search analyzing (shooting at) points around it.

Illustrated in Figure A.6, the algorithm proceeds as follows. For the first step, we provide a rather small subset of points as first guesses to shoot at. In practice, if we can apply some physics insight, we may have an approximate idea of the desired region shape and location, or at least where we will surely not find it.[11] If this is not the case, we can always choose a few equidistant points to start with, which is equivalent to performing a much cheaper low resolution sweep of the grid. After this relatively inexpensive first salvo round is depleted, we account for the *hits* and target their first neighbors for the next barrage. In other words, every point in the grid that has at least one adjacent hit, and has not been targeted in a previous step, is marked for analysis in the following step. Iteration of this process progressively expands the area of favorable points found in each step, growing in an organic-looking manner from a first few *seed hits*. The iteration stops when no further target candidates are found for a subsequent step. Although the idea is very simple, the improvement in speed due to computational effort saving in our problems cannot be overstated, as it will become clear soon.[12]

The first situation in which this algorithm was applied in our work was the exploration of wind model parameter space $(\dot{M}, \dot{E})$ in Section 2.4.2. There, we wanted to find a region of solutions that were compatible with a R_{NS} in a typical range (fully colored area in Figures 2.2 to 2.4).[13] This region needed to be explored in high resolution in order to find a decent amount of solutions with $R_{\mathrm{NS}} = 13$ km. Indeed, the colored area is, in reality, composed by a few thousand *hits* from this search, with an original grid of 128×128 points (that would mean trying over 16 thousand wind model solutions). In this case, we knew exactly where to shoot first, not by physical insight, but because we already had a 32×32 grid exploration to guide us (the bigger points also shown outside this desired area). This lower resolution sweep was previously done to find the region of acceptable (hypothesis consistent) solutions,

[11] The same way we will not find ships on dry land or very shallow waters.

[12] In addition, its beneficial side effect is to minimize chances of suffering the impatience, and possible pain and frustration, from long-running simulations crashing or being useless due to bad set-up.

[13] That is, solutions that met wind base boundary condition, explained in Section 2.2.3, at the given radii.

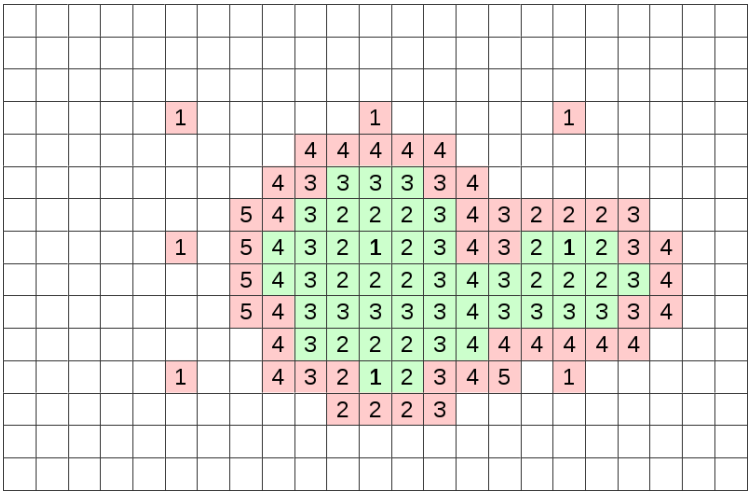

Figure A.6: Battleship algorithm illustration. Numbers represent the iteration step in which grid locations are evaluated. Step 1 targets equally spaced points, manually indicated as first guesses. Subsequent steps expand the search by targeting points that are adjacent to a previous *hit* (green), while points with only *misses* (red) around are not considered as targets for following steps. Empty locations are never targeted by the algorithm.

prior to the development of the *Battleship* algorithm. This is why Figures 2.2 to 2.4 present many *misses* where no solution was found.[14]

The other important application of *Battleship* was sweeping the XRB models (time-step,shell) grid in order to find XRB-wind matching points in Section 3.2. Here, the requisite for a hit was the success in finding a wind profile with a density $\rho_{\rm WB}$ matching the XRB model density $\rho_{\rm BS}$ at that grid point, with given radius and energy outflow. For this, several wind model solutions were tried at each grid point, employing IRIS root finding method, with varying $\dot{M}$. This potentially squares the computing time of each point with respect to the previous example, which required computing only one wind profile per point.[15] Additionally, the grid resolution was fixed by the XRB model data. In most XRB models analyzed, this grid contained around 4×10^5 points, while the high resolution model XRB-A contained over 4×10^6 points. A titanic task, at first sight. Nevertheless, we do not have to explore the whole grid, since we can apply the physical insight obtained from the previous study in Section 2.4. For instance, from the parameter space exploration, we can expect points with normalized energy outflows further than a few percent above or below $\dot{E}/L_o = 1.05$ to likely admit no compatible wind solution at all. In addition, points with physical conditions outside the region of validity of the wind model hypothesis would have to be skipped. This reduced the candidate grid points to a few hundred in low resolution models, and a few thousand in the 200-shell model. With computational cost per point

[14] Later on, we repeated the study with other parameters and scenarios (including different envelope compositions, NS radii and masses, and even white dwarves) using *Battleship* with an equidistant point subset as first guess. Sadly, since time was short, their analysis will be postponed for future work.

[15] Yes, this implies using two nested IRIS root-finding at each XRB grid point: one in the shooting method for calculating each candidate wind profile with different $\dot{M}$, and a second one to find that particular $\dot{M}$ that makes the wind base density match with that of the XRB.

being squared with respect to the previous application, this is still quite a feat, equivalent to sweeping a wind parameter space grid of a few $10^4 - 10^6$ points.

Enter *parallelization*, divide and conquer. We can always partition the original data set and feed each resulting subset to independent instances of our algorithm. Each instance can run on a different processor core of a multi-core machine, or in several machines at once. One way to implement this is to directly divide the grid into different quadrants. However, there is a better way in our case. Since we also want to evaluate a second match in temperature afterwards, not every *hit* in density we find will ultimately be useful.[16] Instead we performed a low resolution first run, with one in every eight points of the grid and skipping the rest. This gave us an insight on where the actual *useful hits* were. With this information we could reduce the target area of first guesses to a few tens or hundred points (tenfold reduction), avoiding points that were far from temperature match, for subsequent runs. We then ran seven more times at 1/8 resolution, in this reduced target area, in parallel, and shifting the positions by one point in each of them to complete the full set.

The computational time saved, when sweeping a grid with *Battleship*, is not always in direct proportion to the ratio of *hits* to unexplored points (e.g., avoiding half the points, does not mean halving the computing time). As stated before, the speed improvement can be much better. For instance, in parameter space exploration, the points with no wind solution usually take the longest to resolve, due to the exhaustive maximum resolution search performed by the *IRIS* root-finding within the shooting method (see Section A.4.1). For each of such points, the average calculation can take up to 2^{m-k} times longer than the average *hit* points, where m is the maximum steps allowed (which *IRIS* depletes before giving up), and k is the average steps needed by *IRIS* to resolve a *hit*. In our study, we used up to $m = 9$ in some cases, while *hits* took a varying number of steps, normally in the range of $k = 3 - 5$, giving $2^{m-k} = 2^4 - 2^6$; i.e., *misses* cost $16 - 64$ times more than *hits*. If *Battleship* only explored a fraction of points β of the entire grid, leaving $1-\beta$ unexplored, then by weighting each grid point evaluation with its corresponding cost, we get that the computing time can be reduced down to a fraction:[17]

$$\theta = \frac{\texttt{Battleship time}}{\texttt{full grid time}} \gtrsim \frac{\beta 2^k}{\beta 2^k + (1-\beta)2^m} = \left(1 + \left(\frac{1-\beta}{\beta}\right)\ 2^{m-k}\right)^{-1} \tag{A.15}$$

of the original cost of exploring the full grid. If, for instance, *Battleship* hits a third of the grid points, $\beta = 1/3$, then with our values of m and k, we get lower bounds for θ between $\frac{1}{33}$ and $\frac{1}{129}$. That is, in the worst of cases, sweeping the entire original grid blindly could have taken between approximately 30 to over 100 times longer. With such a simple idea inspired on children entertainment, playing a game of *Battleship* is not a waste of time, but quite the opposite.

[16] The reason why we do not require this extra condition upfront for a *hit* is because the final matching points did not always lie adjacent to each other, making *Battleship* miss on many.

[17] In reality, we should weight *misses* at the perimeter of the *hit* area with the corresponding maximum *IRIS* steps factor, 2^m. But this is a second order correction most of the time since, in high resolution, the number of perimeter points usually scales with the square root of the number of points in the hit area (at least for single convex area shapes), and can be neglected. An exception is the *hit* area being small compared to the grid ($\beta << 1$), in which case its perimeter would be comparable in size, but also small when compared to the full grid, still saving a lot of computing time. If the resolution is not high, then the grid size itself is not that big, in which case there is practically not much motivation to apply the algorithm in the first place.

A.6 Data smoothing with local regression

During our study in Chapter 3, we had to extract useful information from noisy or otherwise inaccurate data sets. Data smoothing techniques help us create an approximate representation of the general behavior in the original data, while leaving out noise and other rapidly fluctuating details. Among them, local regression (Cleveland 1979) is especially useful for situations where we do not want to impose any global modeling function to fit the data to.[18] Instead, it only fits simple models, usually a polynomial with degree ≤ 2, to subsets of the data localized around each fitting point. The main drawback of the method, thought, is its high demand in terms of computational time compared to other methods, especially when applied in higher dimensions or to large data sets.

Its most common implementation is the *Locally Weighted Scatter-plot Smoothing*, or *LOWESS* (see Cleveland & Loader 1996) which, as the name suggests, preforms a weighted regression that gives more importance to data points the closer they are to the fitting point. At each fitting point, its nearest neighbor data points are selected to perform the weighted polynomial regression. This local polynomial is then evaluated at the fitting point to obtained the new *smoothed* value. The process is repeated for every point of the data set.

The amount of data points selected for the local fit is controlled through a smoothing parameter α, either provided as a fraction of the data points or as a maximum distance to the fitting point. Large values of α produce smoother curves, but may miss some important rapidly-varying detail. Smaller values, on the other hand, conform better to the original data, but may catch some of the undesired noise. The weighting function can also be chosen manually. The default choice is the tri-cube weight function:

$$\omega(x) = (1 - d^3)^3, \tag{A.16}$$

where $d = |x - x_o|$ is the distance from data point x to the fitting point x_o, but others can be picked. Alternatively, if our data points have associated errors $\delta(x)$, we can use them to favor points with smaller error, by choosing $\omega(x) = \delta(x)^{-2}$.

In our work, we employed the `lowess` function provided in basic statistics packages within R scripting language, in two occasions. The first one was to perform a two-dimensional smoothing of some variables in the XRB models data (Section 3.1). For these, the default tri-cube weight function was used, since we had no error data. The large amount of data points, allowed us to choose relatively small smoothing parameter values, $\alpha = 0.05 - 0.2$ (default choice is 0.2), which were manually explored to balance noise reduction against the loss of significant physical features.[19] The second application was on the sequence of matching points between XRB and wind profiles (see Section 3.3.2).[20] In this case, we had fewer points per data set, making it necessary to pick higher smoothing parameters $\alpha = 0.3 - 0.7$. However, this time we had the matching error δ to use as weights, making the smoothed curve follow the more accurate matches.

[18] Although, much earlier, Savitzky & Golay (1964) developed a method of similar characteristics.
[19] For instance, choosing an excessively large α could flatten the XRB luminosity spike.
[20] We also performed an interpolation with the `predict.loess` function.

Appendix B

Input micro-physics

In the stellar wind model we implemented (Section 2.1), the set of dynamic equations (2.1 to 2.4) must be supplemented with constitutive relations that express the total pressure P, specific enthalpy h, and opacity κ, as functions of density ρ, temperature T, and mass abundances X_i, where subindex i denotes the different elements present in the envelope. Pressure and specific enthalpy are determined by the equation of state for the given gas mixture and radiation, as described in Section B.1. Opacity is obtained from interpolation or extrapolation of two different set of tables, and is discussed in Section B.2.

B.1 Equation of state

Specific enthalpy can be expressed in terms of pressure and internal energy density u as:

$$h = \frac{P + u}{\rho}, \tag{B.1}$$

where the contributions from both gas and radiation have to be considered. As in most stars, the contribution from radiation follows a black-body law, then:

$$P_{\text{rad}} = \frac{u_{\text{rad}}}{3} = \frac{aT^4}{3}. \tag{B.2}$$

where $a = \frac{4\sigma}{c} = 7.565 \times 10^{-15} \texttt{erg cm}^{-3}\ \texttt{K}^{-4}$ is the radiation constant. For the range of high pressures and temperatures present in NS expanded envelopes, the gas can be considered to be a non-degenerate, non-relativistic, fully ionized ideal gas:[1]

$$P_{\text{gas}} = \frac{2}{3} u_{\text{gas}} = \frac{\rho k T}{\mu m_A} \tag{B.3}$$

where $k = 1.380649 \times 10^{-16}\ \texttt{erg K}^{-1}$ is the Boltzmann constant, and $m_A = 1.6605391 \times 10^{-24}\ \texttt{g}$ is the atomic mass unit. The mean mass per particle μ, in units of m_A, depends on

[1] However, for temperatures above $10^9\texttt{K}$, effects from electron degeneracy starts to become noticeable (see Blinnikov *et al.* 1996).

the gas composition given by mass abundances X_i or number fractions Y_i, and counts ions and electrons as separate particles. The resulting constitutive relations are:

$$P(\rho, T, X_i) = P_{\rm gas} + P_{\rm rad} = \frac{\rho k T}{\mu(X_i) m_A} + \frac{aT^4}{3} \tag{B.4}$$

$$h(\rho, T, X_i) = h_{\rm gas} + h_{\rm rad} = \frac{5}{2}\frac{kT}{\mu(X_i) m_A} + \frac{4aT^4}{3\rho} \tag{B.5}$$

The aforementioned relationship between μ and the elements mass abundances X_i, or number fractions Y_i, can be derived as follows. For a given species with atomic mass A_i (in m_A units), electric charge Z_i (in electron charge units), if N_i and m_i are the number of particles and the mass of that species in a certain volume, respectively, then the number fraction Y_i, and the mass abundance X_i are, by definition:

$$Y_i = \frac{N_i}{N_T} = \frac{N_i}{\sum_i N_i} \tag{B.6}$$

$$X_i = \frac{m_i}{m_T} = \frac{A_i N_i}{\sum_i A_i N_i} \tag{B.7}$$

where $m_T = \sum_i m_i$ and $N_T = \sum_i N_i$ account for the total aggregated mass and number of particles of all elements, in the same volume, respectively. It is easily seen that they are normalized: $\sum_i Y_i = \sum_i X_i = 1$. In general the mean mass per particle μ, is defined as:

$$\mu = \frac{m_T}{N_T} = \frac{\sum_i A_i N_i}{\sum_i N_i} \tag{B.8}$$

but, for a fully ionized gas, the electrons and ions count separately for particle number, and the mass of the former can be neglected, that is $m_T \simeq m_{\rm ions}$, so:

$$\mu = \frac{m_T}{N_{e^-} + N_{\rm ions}} = \frac{\sum_i A_i N_i}{\sum_i N_i (Z_i + 1)} \tag{B.9}$$

since each species contributes with Z_i electrons plus 1 ion per atom. If we replace definitions B.6 and B.7 into Equation B.9, we get the desired functions:

$$\mu(Y_i) = \frac{\sum_i A_i Y_i}{\sum_i Y_i (Z_i + 1)} \tag{B.10}$$

$$\mu^{-1}(X_i) = \sum_i \frac{X_i}{A_i}(Z_i + 1) \tag{B.11}$$

where we divided both denominator and numerator in Equation B.9 by N_T to obtain B.10. If we also define the mean charge per ion (or average number of electrons per atom) as:

$$\zeta = \frac{N_{e^-}}{N_{\rm ions}} = \frac{\sum_i Z_i N_i}{\sum_i N_i} = \sum_i Z_i Y_i \tag{B.12}$$

we can write the following useful relations:

$$\mu(Y_i) = \frac{\sum_i A_i Y_i}{\zeta + 1} \tag{B.13}$$

$$\mu^{-1}(X_i) = (\zeta + 1) \sum_i \frac{X_i}{A_i} \tag{B.14}$$

where Equation B.13 comes from distributing the parenthesis in the denominator of Equation B.10, and then using B.12 and normalization relation $\sum_i Y_i = 1$. Meanwhile, Equation B.14 is obtained similarly from B.9, but previously dividing its denominator and numerator by N_T. Alternatively, from Equation B.9, multiplying both denominator and numerator by $A_i N_i$ and $\sum_i N_i$, and regrouping factors:

$$\begin{aligned}\mu &= \frac{\sum_i A_i N_i}{A_i N_i} \frac{A_i N_i}{\sum_i N_i} \frac{\sum_i N_i}{\sum_i N_i (Z_i + 1)} \\ &= X_i^{-1} A_i Y_i \ (\zeta + 1)^{-1}\end{aligned}$$

That is:

$$X_i = \frac{A_i Y_i}{\mu(1 + \zeta)} \tag{B.15}$$

which allows us to quickly switch from number fractions to mass abundances of each element separately.

B.2 Opacity

Two different sets of opacity tables have been used in this thesis: the ones by OPAL (Iglesias & Rogers 1996), and The Opacity Project (or TOP) (Seaton *et al.* 1994). Both projects provide a set of tabulated logarithms of Rosseland mean opacities, $\log \kappa$, as a function of $(\log T, \log R)$, where $R = \rho \ (T/10^6)^{-3}$, for different values of hydrogen mass fraction X and metallicity Z. They also provide a set of FORTRAN subroutines to process the tables and interpolate for values in between the tabulated ones for all variables.

In the case of OPAL tables, the relative abundances of the 22 allowed chemical elements is fixed for most elements heavier than helium, allowing the variation of only two of them at a time beyond the value included in the metallicity. This makes it necessary to request the OPAL website to generate a new table set for other desired compositions. In comparison, TOP gives you the option to download a package with all necessary monochromatic opacity tables and subroutines to build your own set of Rosseland mean opacity tables locally, for any arbitrary composition, but only 17 elements are allowed in the mixture. The generation of such sets of opacity tables, for a given custom mix, demands a short extra computing time. So does the pre-loading of the up to 2 gigabytes of monochromatic opacity data, which is required to remain in the main memory for generating new mixture tables. This preparation takes a few extra minutes at the beginning of every wind simulation.

The opacity tables provided by OPAL cover a wider domain in temperature and density, but the metallicity is limited to $Z = 0.1$ in most cases. For the first group of simulations described in Section 2.4, the opacity tables from OPAL have been used. For the simulations that required higher metallicity, such as the ones performed for Chapter 3, The Opacity Project packages were used. It is worth mentioning, though, that since these tables allow fewer elements than the ones contemplated in XRB hydrodynamic models studied in Chapter 3, the composition used for calculating the opacities through TOP had to be approximated. The abundances of elements heavier than Ni were added to it, which is the heaviest one that TOP allows. This is a limitation that cannot be resolved at present time, until opacity tables with heavier elements become available.

In order to obtain opacities outside the available temperature and density domain from OPAL or TOP, different methods were employed depending on which set of tables was being used and which region of the $(\log T, \log R)$ space was considered. Given the typical temperature and density values expected for the wind models in the XRB scenario, the regions for $\log R > 0$, and $\log T < 5$ are not of concern, and there's no need to extrapolate in these directions. However, the high temperatures reached by XRBs are outside the available domains, and so is the small density (and R) at a typical wind photosphere.

At low density the opacity is expected to be dominated by Thompson electron scattering, $\kappa_{es} = 0.2\ \mathtt{cm^2 g^{-1}}$. As temperature escalates, opacity drops due to electron-positron pair creations. Buchler & Yueh (1976) have calculated opacity values in this regime, and the formula proposed by Paczyński (1983):

$$\kappa_P = \kappa_{\rm es}\ (1+X)\left[1+(\alpha T)^{\xi}\right]^{-1}, \tag{B.16}$$

with $\xi = 0.86$ and $\alpha^{-1} = 4.5\times10^8\mathtt{K}$, approximates these values very well for a non-degenerate gas, and also approaches Thompson scattering value as T drops.

Formula B.16 was used for temperatures above the respective maximum, and R values below the respective minimum, of each table sets (OPAL or TOP). However, this formula does not match continuously with TOP values at its reduced domain borders. This represents a potential problem since it translates into a discontinuity of the derivatives in the wind model equations, making the numerical integration algorithms behave erratically. The following blend scheme was employed to overcome this issue. For any two functions $f(x), g(x)$ overlapping in $0 \le x \le 1$, consider the blend function:

$$F(x) = b(x)f(x) + (1-b(x))\ g(x) \tag{B.17}$$

with
$$b(x) = \frac{1}{2} - \frac{1}{2}cos(\pi x) \tag{B.18}$$

where x is a parameter that measures the distance to a given border of TOP domains. By setting f to be the interpolated TOP opacities and g the extrapolation Equation B.16, for instance, we obtain a smooth transition with continuous derivatives.

Appendix C

Additional XRB wind solutions

In Chapter 3 we have obtained stellar wind solutions matching the conditions of XRB-A, that is, the 200-shell XRB hydrodynamic model by José *et al.* (2010). Here we will present the analogous results for the remaining 55-shell bursts we were able to analyze, XRB-1 to XRB-4, all corresponding to Model #1 from Table 3.1. We will comment on some of the figures shown and their features, only when remarkable differences are found with respect to the higher resolution model, especially if they are significant for the main results description in Section 3.3.

C.1 Wind-Burst matching solutions

Since bursts XRB-1 to XRB-4 present a lower shell resolution, the jump of physical values between shells is considerably larger. This makes it more difficult for the algorithm described in Section 3.2 to find a match within such a low matching error tolerance, $\delta < 0.01$, as was used for the higher resolution model XRB-A. Although matching points were actually found, with a slightly higher but still low $\delta < 0.05$, in some models they were not enough to reconstruct a decent time evolution. For these models, even larger δ thresholds were chosen, keeping in mind their low accuracy. This is later partially compensated when performing the matching points smoothing and interpolation (described in Section 3.3.2), by the fact we are using the same matching errors as inverse weights, in the form $\omega = \delta^{-2}$, to get a curve that sticks closer to the most accurate matches where possible, while still being able to connect the missing dots with the help of the less accurate ones. This way a more complete, but less detailed picture can be obtained.

Figure C.1 shows the matching points obtained in each of the burst evolutions, along with the δ threshold employed. The first difference with XRB-A arises here. In some of these bursts an almost complete evolution is observed. A characteristic U-shaped path of matching points is observed around the peak radial expansion in models XRB-1 and XRB-3. The match is located at relatively shallow shells by the onset of the wind, then it travels to deeper shells, and finally rises again towards the end. This does not seem to be the case with XRB-2, which shows matching points starting at deeper layers, rising slowly in the beginning, and more rapidly towards outer shells by the end, in a way that qualitatively resembles that of XRB-A. Even though we observe the full evolution of the wind phase, the overall duration is shorter than that of XRB-A. All of them lasting less than 10 s, while

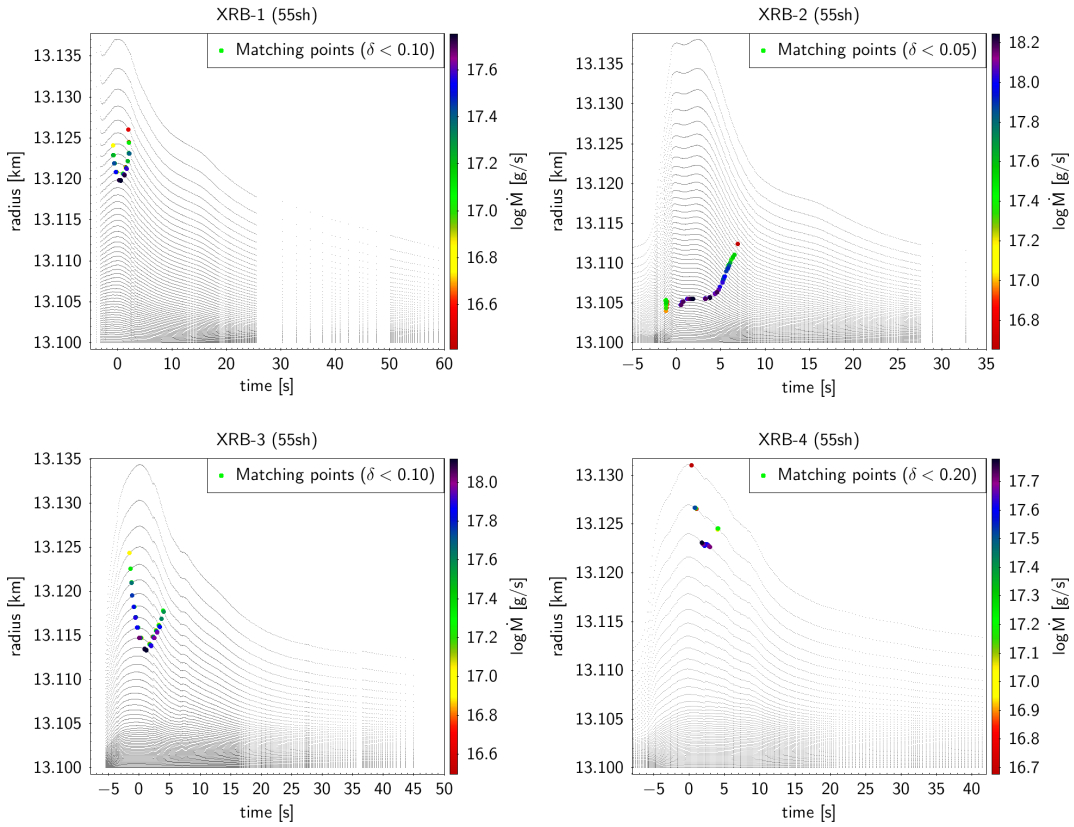

Figure C.1: Wind matching points during XRB evolution. Analog to Fig 3.3 but for models XRB-1 to XRB-4, in reading order.

XRB-A wind duration was approximately 30 s.

The evolution of matching points in the wind parameter space is shown in Figure C.2. In all of the bursts analyzed, they appear along the same curve. The initial matching points show higher energy outflows, $\dot{E}/L_X \simeq 1.075$, and lower mass outflows, $\dot{M} < 10^{17}$g/s, that is the top left corner of the plot. They evolve towards lower $\dot{E}/L_X \sim 1.05$ and higher $\dot{M} \sim 10^{18}$g/s, by the middle of their evolution (bottom right corner), and go back along the same curve to the starting position in later times. By contrast XRB-A showed only the last half of this behavior, starting from the bottom right corner.

C.2 Mass-loss

Figure C.3 shows the application of the smoothing-interpolation technique, described in Section 3.3.2, to the mass outflow of matching points in bursts XRB-1 to XRB-4. Again, this allows us to reconstruct the time evolution necessary to calculate the mass-loss. Although the matching points show significantly larger error with respect to XRB-A (as shown with the color scale), the curve reconstructed with this technique follows those points with smaller error. The curve color also gives an estimate of the matching error expected for it at each

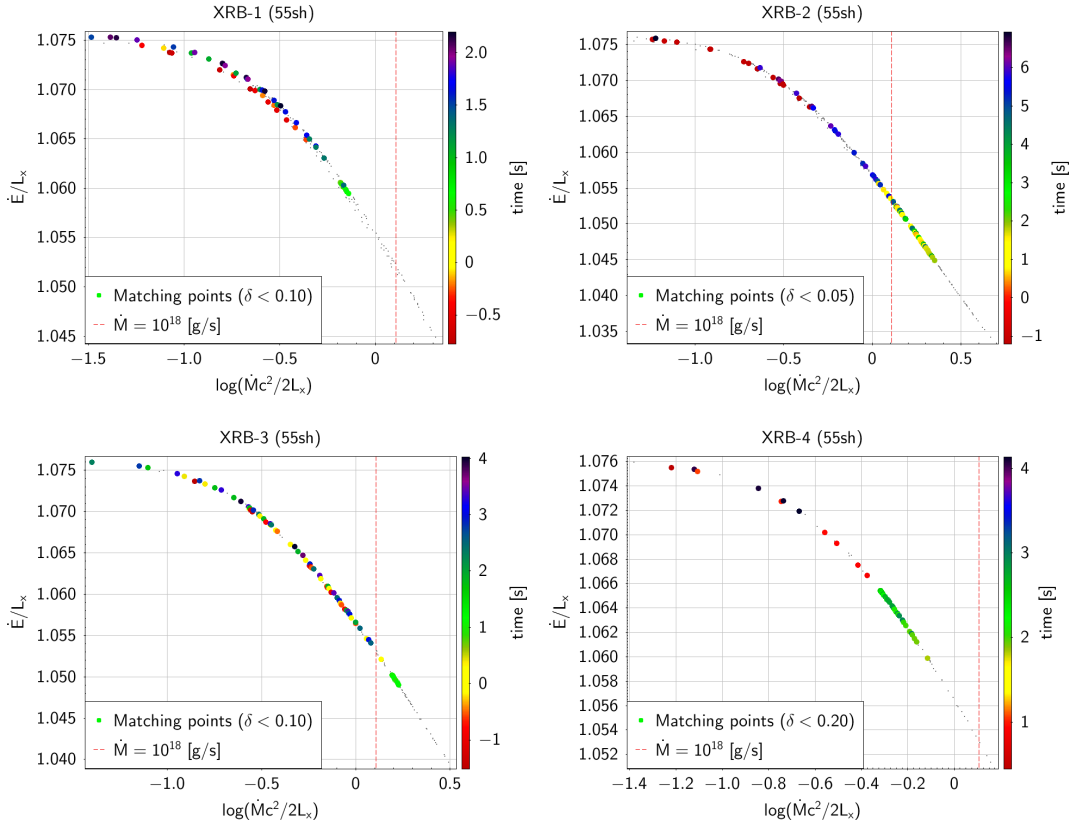

Figure C.2: Evolution of Wind-Burst matching points in parameter space. Analog to Fig 3.4, but for models XRB-1 to XRB-4, in reading order.

time. In most cases, this expected error is still quite small, in the range of $\delta \sim 0.01-0.03$. The exception is XRB-4, which shows considerably larger errors, $\delta > 0.15$. Very few matching points were found below such large error threshold, making it difficult to reconstruct an accurate evolution. This may imply that XRB-4 is not a good candidate for a wind to appear.

The time-integrated expelled masses for each burst are: $\Delta m = 2.21 \times 10^{17}$ g from XRB-1, $\Delta m = 7.58 \times 10^{18}$ g from XRB-2, $\Delta m = 2.18 \times 10^{18}$ g from XRB-3, and $\Delta m = 1.04 \times 10^{18}$ g from XRB-4. These values are all at least an order of magnitude smaller than in XRB-A, where $\Delta m = 6.16 \times 10^{19}$g.

By applying the same smoothing technique to the mass abundances of every isotope, we are able to reconstruct their time evolution and integrate the total masses expelled (Equation 3.5) for each of them. The results are shown in Figure C.4, for the unstable isotopes directly produced and expelled during XRB winds, and in Figure C.5 for their final stable counterparts. XRB-1 shows significantly lower expelled quantities of the heaviest elements allowed in the XRB models. This heavy elements expulsion becomes more important in the subsequent bursts. This may have two contributing factors. The first is the fact that the wind matching points occur at deeper shells, where the presence of heavy elements is more

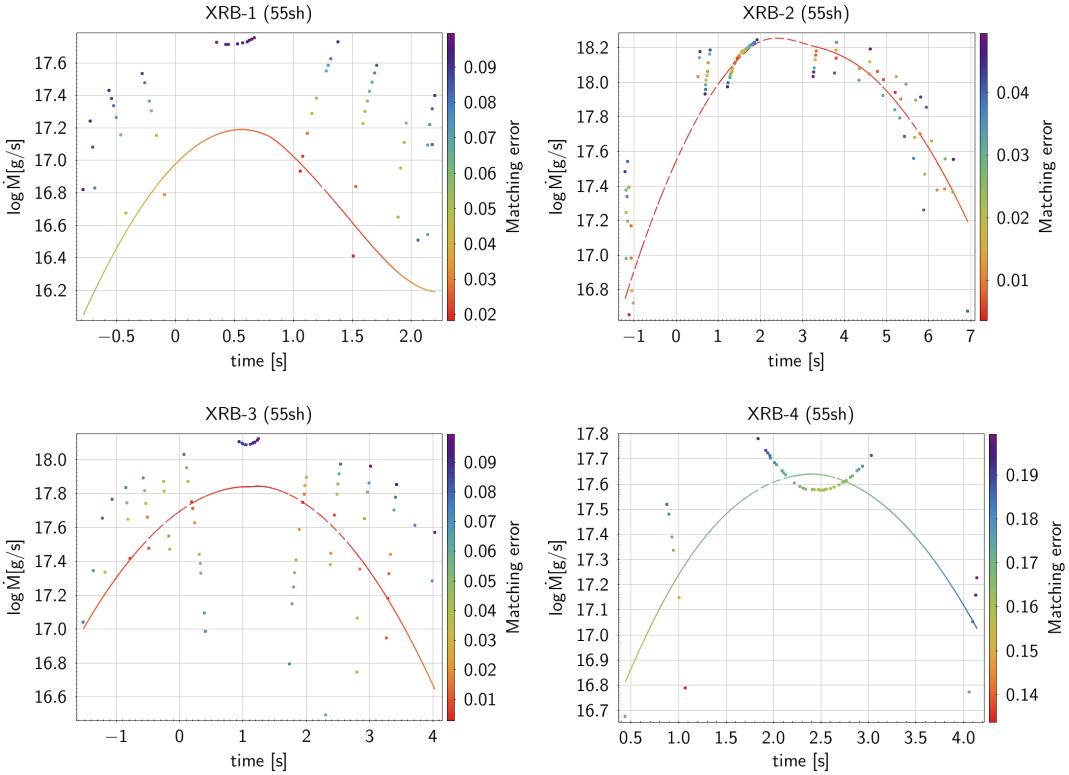

Figure C.3: Time evolution of mass outflow, $\dot{M}$, reconstructed with smoothing technique from matching points with higher error. Analog to Fig 3.7, but for bursts XRB-1 to XRB-4, in reading order.

prominent. This is the case of XRB-2 (see Figure C.1). The second factor is related to the overall availability of heavy elements in the envelope. With every bursting episode, new ashes of nuclear burning accumulate in every shell. This may well be the case of and XRB-3 and XRB-4, showing high quantities of heavy elements expelled even when the matching points occur within in the top $\sim 5 - 15$ shells, as in XRB-1.

Only very small quantities of light p-nuclei are expelled in these cases. The most significant is ^{92}Mo with: 4.41×10^{12} g in XRB-2, 8.95×10^{12} g in XRB-3, and 3.6×10^{13} g in XRB-4. These are thousands of times smaller than in XRB-A. Their contribution to Galactic abundances is therefore even more insignificant.

C.3 Observable magnitudes

Lastly, we would like to compare the evolution of photospheric magnitudes in the lower resolution bursts to the similar results obtained for XRB-A. Figures C.6 to C.9, show the evolution of photospheric radius, temperature, density, and radiative luminosity, for each burst.

In all four bursts, the photospheric radius plots (top left panel in each figure) show almost

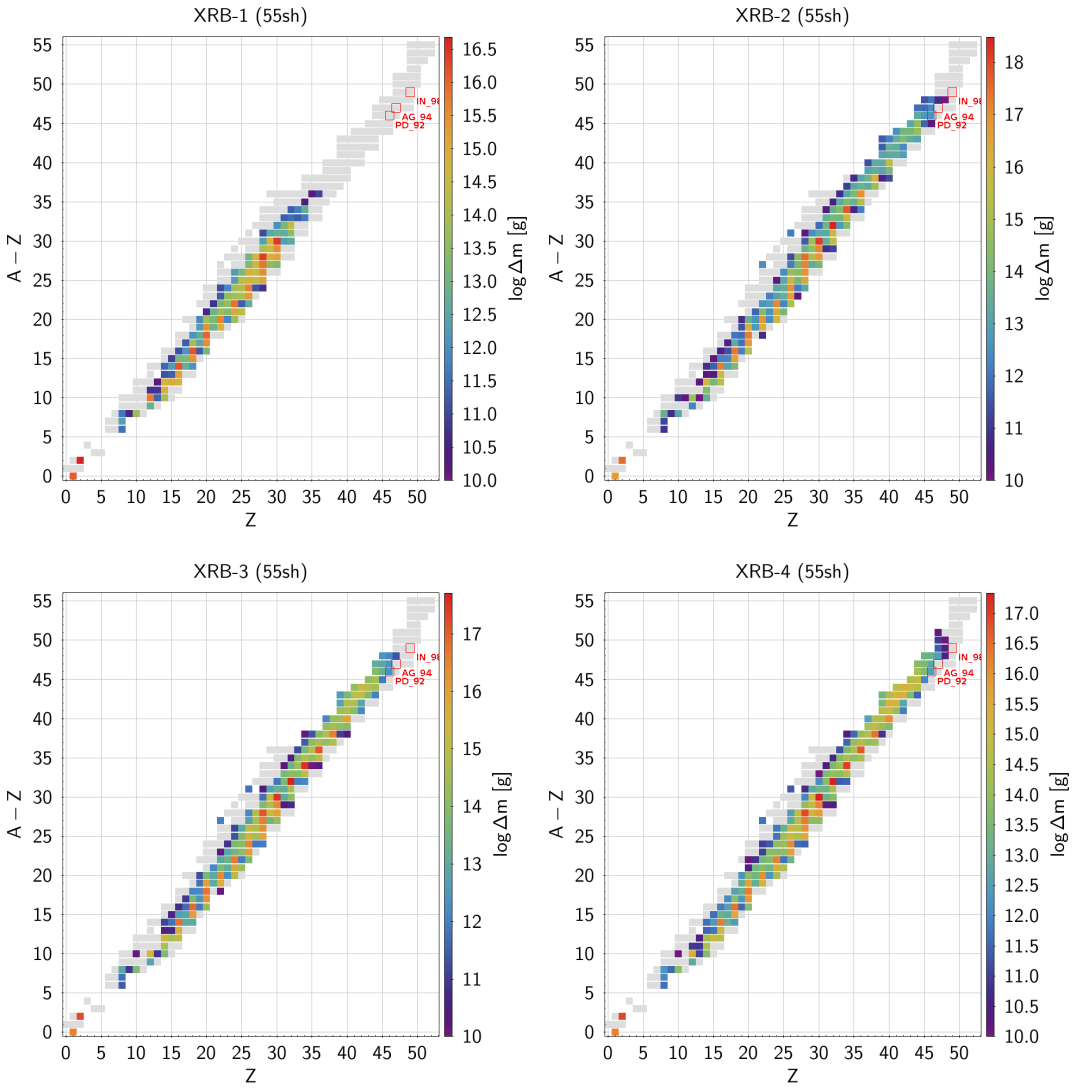

Figure C.4: Mass yield per isotope for the duration of the wind. Same as Fig 3.9, but for bursts XRB-1 to XRB-4, in reading order.

the full cycle of expansion and recession of the envelope due to the wind. In most of them, it starts very close to the NS surface (marked by a gray dashed line), it expands to a maximum radius, and recedes back to the original radius. The maximum photospheric expansion varies in each case. XRB-1 reaches a maximum of only ~ 35 km. The most expanded one is XRB-2, with ~ 300 km, followed by XRB-3, at ~ 120 km, and finally XRB-4, expanding to ~ 80 km.

Photospheric temperature and density show the opposite behavior, starting at higher values, going down and then rising again. This behavior is in complete agreement with the $r_{\rm ph} \sim T_{\rm ph}^{-2} \sim \rho_{\rm ph}^{-1}$ correlations found in Section 2.4.3 and Section 3.3.3. Luminosity plots show the small dip mentioned in Section 3.3.3. Their minima are only a few percent below

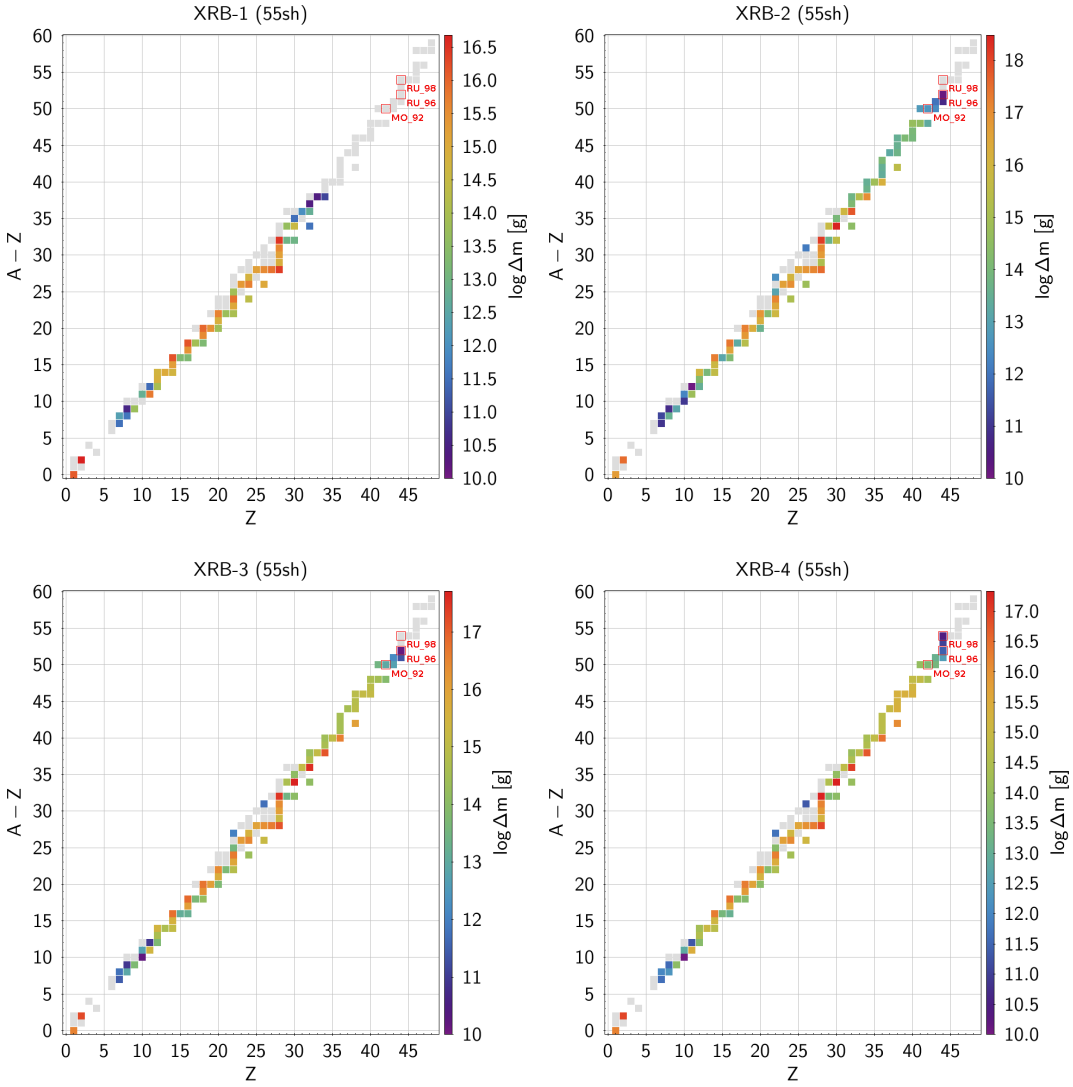

Figure C.5: Stable isotopes yield (for models XRB-1 to XRB-4). Final products from radioactive decay of the unstable isotopes shown in Fig C.4.

the starting and ending values ($5 - 6\%$). Nevertheless, the overall photopheric luminosity is much lower than the peak luminosities reported in the XRB models without wind (see Table 3.1). The reasons behind this difference and its implications were already discussed in the aforementioned subsection in Chapter 3.

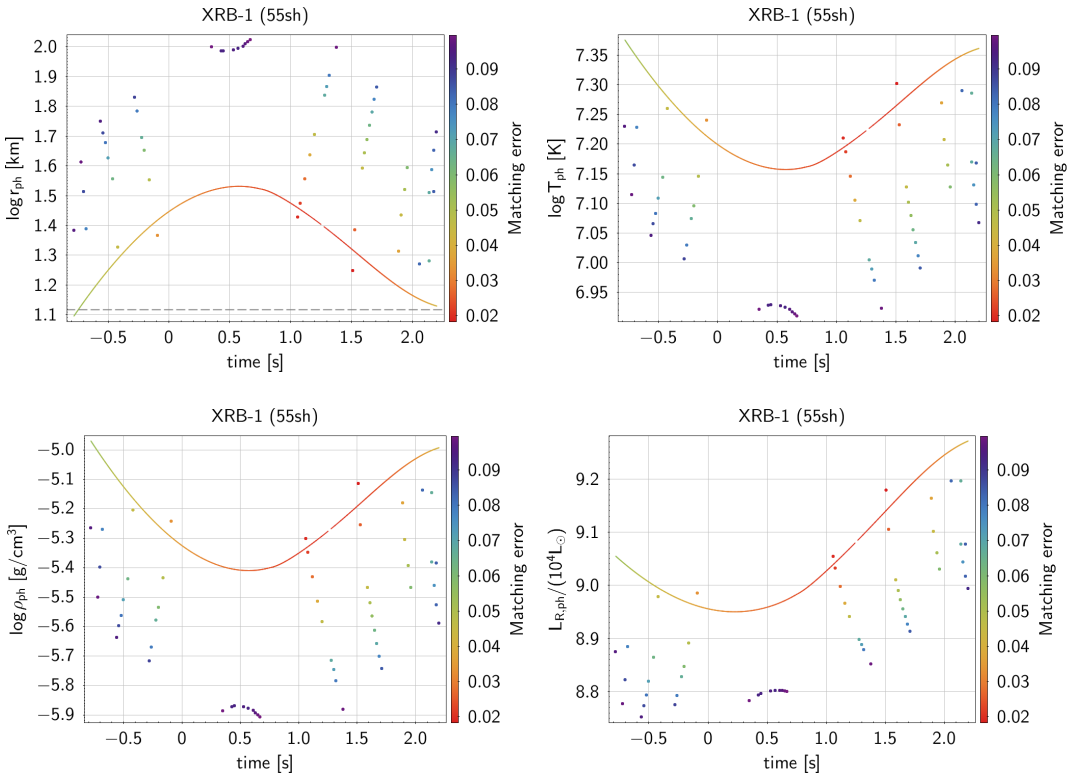

Figure C.6: Time evolution of observable (photospheric) magnitudes, in model XRB-1. In reading order, radius, temperature, wind velocity, and radiative luminosity. Analog to Fig 3.11, but for model XRB-1.

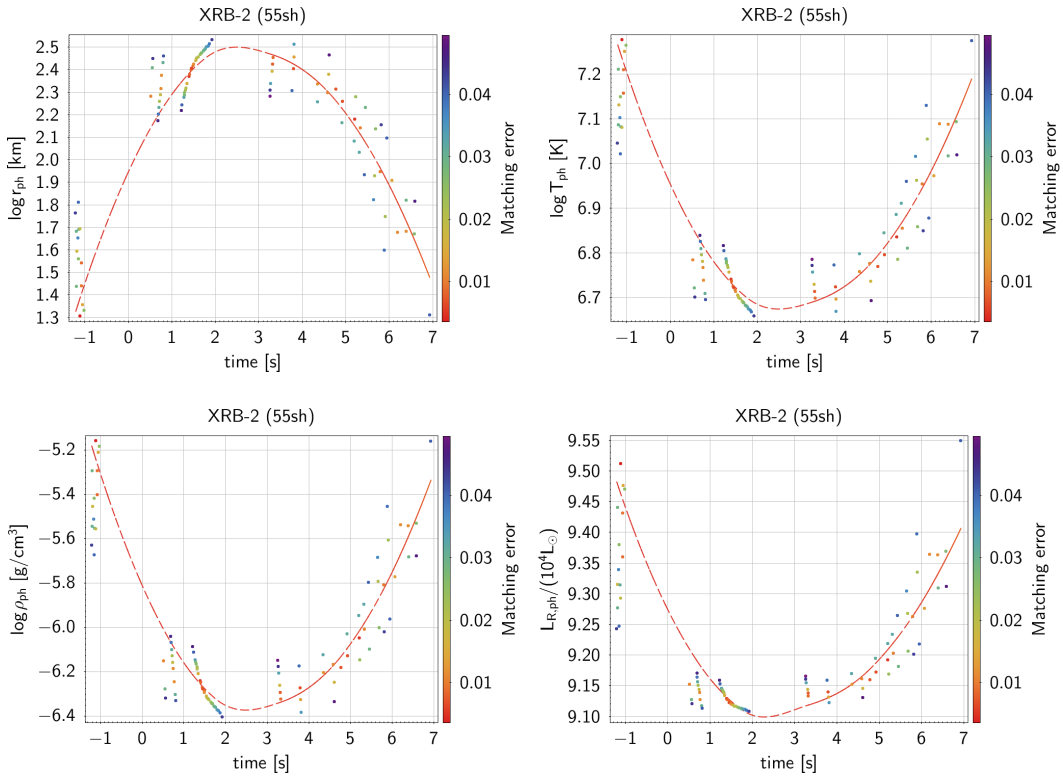

Figure C.7: Same as Fig C.6, but for model XRB-2.

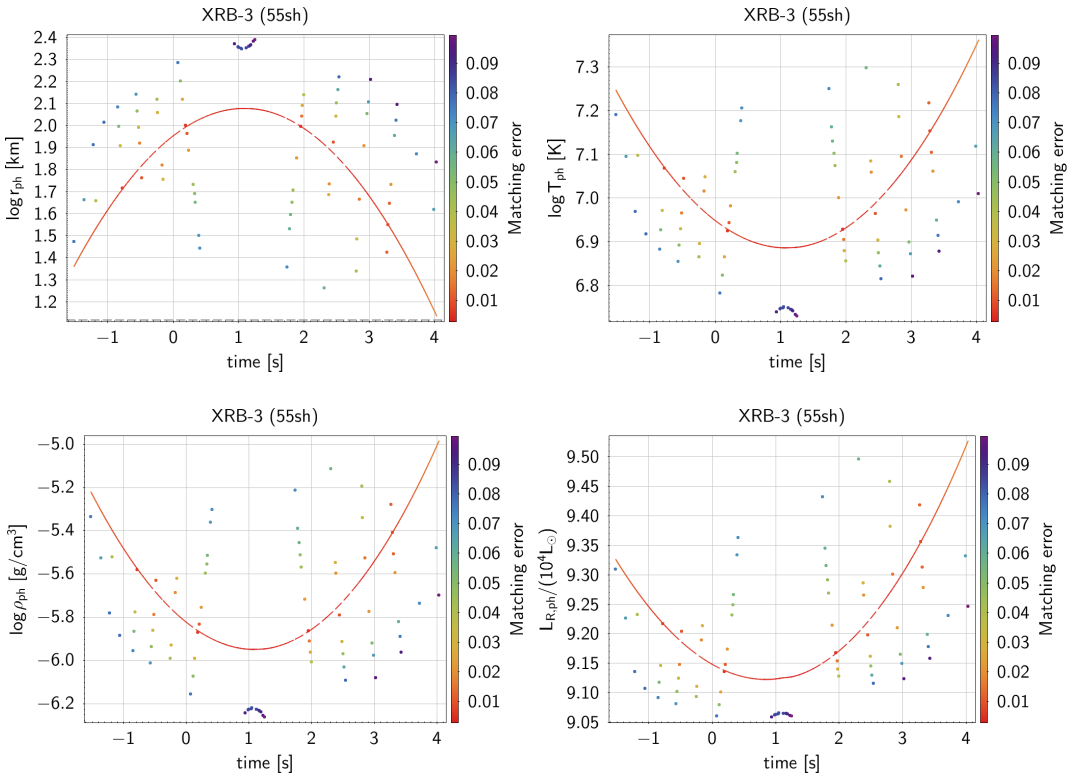

Figure C.8: Same as Fig C.6, but for model XRB-3.

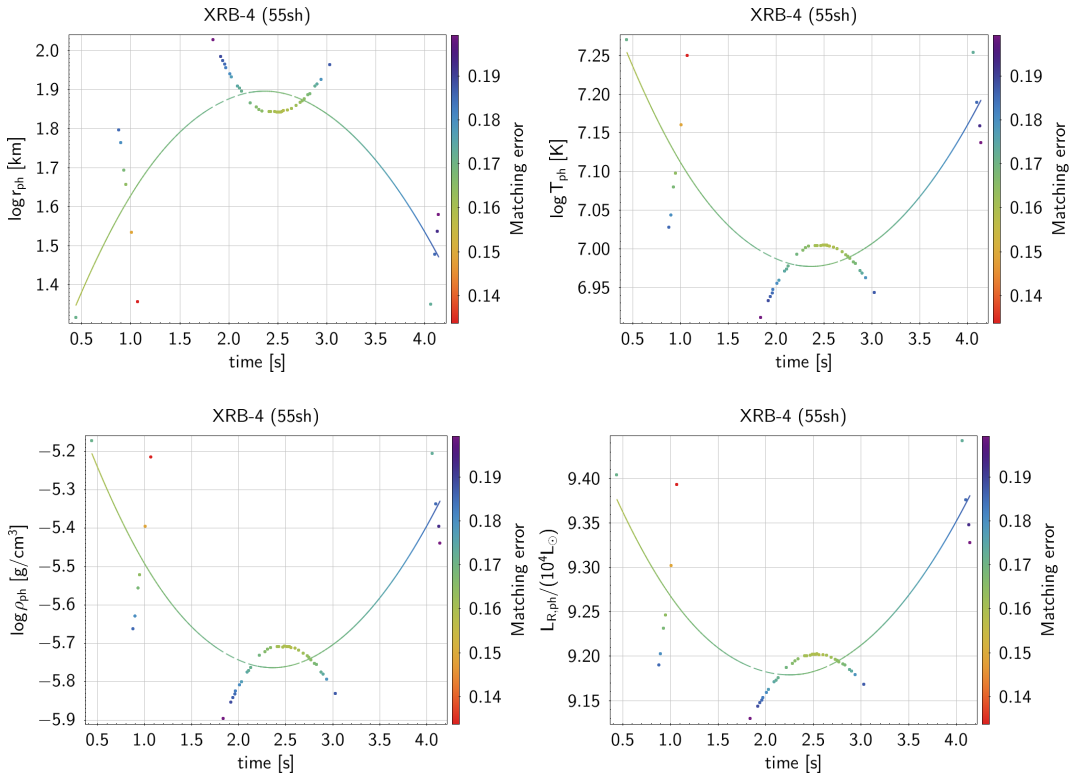

Figure C.9: Same as Fig C.6, but for model XRB-4.

Bibliography

Ayasli, S., & Joss, P. C. 1982. Thermonuclear processes on accreting neutron stars - A systematic study. *ApJ*, **256**(May), 637–665.

Babushkina, O. P., Kudriavtsev, M. I., Melioranskii, A. S., Savenko, I. A., Iushkov, B. I., & Bratoliubova-Tsulukidze, L. S. 1975. Hard X-ray bursts in June 1971. *Soviet astronomy letters*, **1**(Feb.), 32–34.

Belian, R. D., Conner, J. P., & Evans, W. D. 1976. The discovery of X-ray bursts from a region in the constellation Norma. *ApJ*, **206**(June), L135–L138.

Bildsten, L., Chang, P., & Paerels, F. 2003. Atomic Spectral Features during Thermonuclear Flashes on Neutron Stars. *ApJ*, **591**(1), L29–L32.

Blinnikov, S. I., Dunina-Barkovskaya, N. V., & Nadyozhin, D. K. 1996. Equation of State of a Fermi Gas: Approximations for Various Degrees of Relativism and Degeneracy. *ApJS*, **106**(Sept.), 171.

Buchler, J. R., & Yueh, W. R. 1976. Compton scattering opacities in a partially degenerate electron plasma at high temperatures. *ApJ*, **210**(Dec.), 440–446.

Bult, P., Jaisawal, G. K., GÃ$\frac{1}{4}$ver, T., Strohmayer, T. E., Altamirano, D., Arzoumanian, Z., Ballantyne, D. R., Chakrabarty, D., Chenevez, J., Gendreau, K. C., Guillot, S., & Ludlam, R. M. 2019. A NICER thermonuclear burst from the millisecond x-ray pulsar SAX j1808.4–3658. *The astrophysical journal*, **885**(1), L1.

Cash, J. R., & Karp, A. H. 1990. A variable order Runge-Kutta method for initial value problems with rapidly varying right-hand sides. *Acm trans. math. softw.*, **16**(3), 201–222.

Castor, J. I., Abbott, D. C., & Klein, R. I. 1975. Radiation-driven winds in Of stars. *ApJ*, **195**(Jan), 157–174.

Chang, P., Bildsten, L., & Wasserman, I. 2005. Formation of Resonant Atomic Lines during Thermonuclear Flashes on Neutron Stars. *ApJ*, **629**(2), 998–1007.

Chang, P., Morsink, S., Bildsten, L., & Wasserman, I. 2006. Rotational Broadening of Atomic Spectral Features from Neutron Stars. *ApJ*, **636**(2), L117–L120.

Cleveland, W. S. 1979. Robust locally weighted regression and smoothing scatterplots. *J. Am. Stat. Assoc.*, **74**(368), 829–836.

Cleveland, W. S., & Loader, C. 1996. Smoothing by local regression: Principles and methods. *Pages 10–49 of:* Härdle, W., & Schimek, M. G. (eds), *Statistical theory and computational aspects of smoothing*. Heidelberg: Physica-Verlag HD.

Damen, E., Magnier, E., Lewin, W. H. G., Tan, J., Penninx, W., & van Paradijs, J. 1990. X-ray bursts with photospheric radius expansion and the gravitational redshift of neutron stars. *A&A*, **237**(Oct.), 103.

Ebisuzaki, T., Hanawa, T., & Sugimoto, D. 1983. Mass loss from the neutron stars associated with X-ray bursts. *PASJ*, **35**(1), 17–32.

Fehlberg, E. 1970. Klassische runge-kutta-formeln vierter und niedrigerer ordnung mit schrittweiten-kontrolle und ihre anwendung auf wärmeleitungsprobleme. *Computing*, **6**(1), 61–71.

Finger, M. H., Wilson, R. B., Harmon, B. A., Hagedon, K., & Prince, T. A. 1996. GRO J1744-28. *IAU Circ.*, **6285**(Jan.), 1.

Fisker, J. L., Schatz, H., & Thielemann, F.-K. 2008. Explosive Hydrogen Burning during Type I X-Ray Bursts. *ApJS*, **174**(1), 261–276.

Galloway, D. K., Muno, M. P., Hartman, J. M., Psaltis, D., & Chakrabarty, D. 2008. Thermonuclear (Type I) X-Ray Bursts Observed by the Rossi X-Ray Timing Explorer. *ApJS*, **179**(2), 360–422.

Goodwin, A. J., Heger, A., Chambers, F. R. N., Watts, A. L., & Cavecchi, Y. 2021. X-ray burst ignition location on the surface of accreting X-ray pulsars: can bursts preferentially ignite at the hotspot? *MNRAS*, **505**(4), 5530–5542.

Grindlay, J., Gursky, H., Schnopper, H., Parsignault, D. R., Heise, J., Brinkman, A. C., & Schrijver, J. 1976. Discovery of intense X-ray bursts from the globular cluster NGC 6624. *ApJ*, **205**(May), L127–L130.

Guichandut, S., Cumming, A., Falanga, M., Li, Z., & Zamfir, M. 2021. Expanded Atmospheres and Winds in Type I X-Ray Bursts from Accreting Neutron Stars. *ApJ*, **914**(1), 49.

Güver, T., Psaltis, D., & Özel, F. 2012. Systematic Uncertainties in the Spectroscopic Measurements of Neutron-star Masses and Radii from Thermonuclear X-Ray Bursts. I. Apparent Radii. *ApJ*, **747**(1), 76.

Hansen, C. J., & van Horn, H. M. 1975. Steady-state nuclear fusion in accreting neutron-star envelopes. *ApJ*, **195**(Feb.), 735–741.

Herrera, Y., Sala, G., & José, J. 2020. Simulations of stellar winds from X-ray bursts: Characterization of solutions and observable variables. *A&a*, **638**, A107.

Hoffman, J. A., Marshall, H. L., & Lewin, W. H. G. 1978. Dual character of the rapid burster and a classification of X-ray bursts. *Nature*, **271**(5646), 630–633.

Iben, Icko, J., Tutukov, A. V., & Yungelson, L. R. 1995. A Model of the Galactic X-Ray Binary Population. II. Low-Mass X-Ray Binaries in the Galactic Disk. *ApJS*, **100**(Sept.), 233.

Iglesias, C. A., & Rogers, F. J. 1996. Updated Opal Opacities. *ApJ*, **464**(Jun), 943.

José, J., & Hernanz, M. 1998. Nucleosynthesis in Classical Novae: CO versus ONe White Dwarfs. *ApJ*, **494**(Feb.), 680–690.

José, J. 2016. *Stellar Explosions: Hydrodynamics and Nucleosynthesis*. Boca Raton, FL: CRC/Taylor and Francis.

José, J., Moreno, F., Parikh, A., & Iliadis, C. 2010. Hydrodynamic Models of Type I X-ray Bursts: Metallicity Effects. *ApJS*, **189**(1), 204–239.

Joss, P. C. 1977. X-ray bursts and neutron-star thermonuclear flashes. *Nature*, **270**(5635), 310–314.

Joss, P. C. 1978. Helium-burning flashes on an accreting neutron star: a model for X-ray burst sources. *ApJ*, **225**(Nov.), L123–L127.

Joss, P. C., & Li, F. K. 1980. Helium-burning flashes on accreting neutron stars - Effects of stellar mass, radius, and magnetic field. *ApJ*, **238**(May), 287–295.

Joss, P. C., & Melia, F. 1987. Quasi-static Winds from Neutron Stars. *ApJ*, **312**(Jan.), 700.

Kato, M. 1983. Neutron star wind. *PASJ*, **35**(1), 33–46.

Kato, M., & Hachisu, I. 1994. Optically Thick Winds in Nova Outbursts. *ApJ*, **437**(Dec), 802.

Keek, L., & in't Zand, J. J. M. 2008 (Jan). On burning regimes and long duration X-ray bursts. *Page 32 of: Proceedings of the 7th integral workshop*.

Kouveliotou, C., Kommers, J., Lewin, W. H. G., van Paradijs, J., Fishman, G. J., Briggs, M. S., Hurley, K., Harmon, A., Finger, M. H., & Wilson, R. B. 1996. GRO J1744-28. *IAU Circ.*, **6286**(Jan.), 1.

Kovetz, A. 1998. The Simulation of Nova Evolution with Optically Thick Winds. *ApJ*, **495**(1), 401–406.

Lamb, D. Q., & Lamb, F. K. 1978. Nuclear burning in accreting neutron stars and X-ray bursts. *ApJ*, **220**(Feb.), 291–302.

Lattimer, J. M., & Prakash, M. 2006. Equation of state, neutron stars and exotic phases. *Nuclear Physics A*, **777**(Oct.), 479–496.

Lewin, W. H. G., Doty, J., Clark, G. W., Rappaport, S. A., Bradt, H. V. D., Doxsey, R., Hearn, D. R., Hoffman, J. A., Jernigan, J. G., Li, F. K., Mayer, W., McClintock, J., Primini, F., & Richardson, J. 1976. The discovery of rapidly repetitive X-ray bursts from a new source in Scorpius. *ApJ*, **207**(July), L95–L99.

Lewin, W. H. G., van Paradijs, J., & Taam, R. E. 1993. X-Ray Bursts. *Space Sci. Rev.*, **62**(3-4), 223–389.

Lodders, K., Palme, H., & Gail, H. P. 2009. Abundances of the Elements in the Solar System. *Landolt börnstein*, **4B**(Jan.), 712.

Maraschi, L., & Cavaliere, A. 1977 (Jan.). X-ray bursts of nuclear origin? *Pages 127–128 of: X-ray binaries and compact objects.*

Özel, F., Baym, G., & Güver, T. 2010. Astrophysical measurement of the equation of state of neutron star matter. *Phys. Rev. D*, **82**(Nov), 101301.

Paczyński, B. 1983. Models of X-ray bursters with radius expansion. *ApJ*, **267**(Apr.), 315–321.

Paczyński, B., & Prószyński, M. 1986. Models of Radiation-driven Winds from General Relativistic Neutron Stars. *ApJ*, **302**(Mar), 519.

Parker, E. N. 1965. Dynamical Theory of the Solar Wind. *Space Sci. Rev.*, **4**(5-6), 666–708.

Paxton, B., Bildsten, L., Dotter, A., Herwig, F., Lesaffre, P., & Timmes, F. 2011. Modules for Experiments in Stellar Astrophysics (MESA). *ApJS*, **192**(Jan.), 3.

Pfahl, E., Rappaport, S., & Podsiadłowski, P. 2003. The Galactic Population of Low- and Intermediate-Mass X-Ray Binaries. *ApJ*, **597**(2), 1036–1048.

Pietsch, W., & Haberl, F. 2005. XMM-Newton detection of type I X-ray bursts in M 31. *A&A*, **430**(Jan.), L45–L48.

Podsiadłowski, P., Rappaport, S., & Pfahl, E. D. 2002. Evolutionary Sequences for Low- and Intermediate-Mass X-Ray Binaries. *ApJ*, **565**(2), 1107–1133.

Press, W. H., Teukolsky, S. A., Vetterling, W. T., & Flannery, B. P. 1992. *Numerical recipes in fortran (2nd ed.): The art of scientific computing.* USA: Cambridge University Press.

Press, W. H., Teukolsky, S. A., Vetterling, W. T., Flannery, B. P., & Metcalf, M. 1996. *Numerical recipes in fortran 90: Volume 2, volume 2 of fortran numerical recipes: The art of parallel scientific computing.* Cambridge University Press.

Quinn, T., & Paczyński, B. 1985. Stellar winds driven by super-Eddington luminosities. *ApJ*, **289**(Feb), 634–643.

Sala, G., Haberl, F., José, J., Parikh, A., Longland, R., Pardo, L. C., & Andersen, M. 2012. Constraints on the Mass and Radius of the Accreting Neutron Star in the Rapid Burster. *ApJ*, **752**(2), 158.

Savitzky, A., & Golay, M. J. E. 1964. Smoothing and differentiation of data by simplified least squares procedures. *Analytical chemistry*, **36**(Jan.), 1627–1639.

Schatz, H., Aprahamian, A., Görres, J., Wiescher, M., Rauscher, T., Rembges, J., Thielemann, F.-K., Pfeiffer, B., Möller, P., Kratz, K.-L., Herndl, H., Brown, B., & Rebel, H. 1998. rp-process nucleosynthesis at extreme temperature and density conditions. *Physics reports*, **294**(4), 167 – 263.

Schatz, H., Aprahamian, A., Barnard, V., Bildsten, L., Cumming, A., Ouellette, M., Rauscher, T., Thielemann, F.-K., & Wiescher, M. 2001. End Point of the *rp* Process on Accreting Neutron Stars. *Phys. Rev. Lett.*, **86**(Apr), 3471–3474.

Seaton, M. J., Yan, Y., Mihalas, D., & Pradhan, A. K. 1994. Opacities for stellar envelopes. *MNRAS*, **266**(Feb.), 805.

Shore, S. N. 1992. Chapter 8 - Outflows and accretion. *Pages 257–317 of:* Shore, S. N. (ed), *An introduction to astrophysical hydrodynamics*. San Diego: Academic Press.

Steiner, A. W., Lattimer, J. M., & Brown, E. F. 2010. The Equation of State from Observed Masses and Radii of Neutron Stars. *ApJ*, **722**(1), 33–54.

Strohmayer, T., & Bildsten, L. 2006. *New views of thermonuclear bursts*. Vol. 39. Cambridge Univ. Press. Pages 113–156.

Tan, W. P., Fisker, J. L., Görres, J., Couder, M., & Wiescher, M. 2007. O15(α,γ)Ne19 Breakout Reaction and Impact on X-Ray Bursts. *Phys. Rev. Lett.*, **98**(24), 242503.

Turolla, R., Nobili, L., & Calvani, M. 1986. On Hydrodynamics of Radiatively Driven Winds. *ApJ*, **303**(Apr), 573.

Weinberg, N. N., Bildsten, L., & Schatz, H. 2006. Exposing the Nuclear Burning Ashes of Radius Expansion Type I X-Ray Bursts. *ApJ*, **639**(2), 1018–1032.

Woosley, S. E., & Taam, R. E. 1976. γ-ray bursts from thermonuclear explosions on neutron stars. *Nature*, **263**(5573), 101–103.

Woosley, S. E., Heger, A., Cumming, A., Hoffman, R. D., Pruet, J., Rauscher, T., Fisker, J. L., Schatz, H., Brown, B. A., & Wiescher, M. 2004. Models for Type I X-Ray Bursts with Improved Nuclear Physics. *ApJS*, **151**(1), 75–102.

Yu, H., & Weinberg, N. N. 2018. Super-Eddington Winds from Type I X-Ray Bursts. *ApJ*, **863**(1), 53.

Żytkow, A. 1972. On the Stationary Mass Outflow from Stars. I. The Computational Method and the Results for 1 $M_\odot$ Star. *Acta Astron.*, **22**(Jan), 103.